

POLITECNICO
MILANO 1863

SCUOLA DI INGEGNERIA INDUSTRIALE
E DELL'INFORMAZIONE

Analysis of Breakup Events along Earth-Moon L2 Halo Orbits and Cislunar Disposal Trajectories

Tesi di Laurea Magistrale in
Space Engineering - Ingegneria Spaziale

Author: **Andrea Dal Passo**

Student ID: 249712
Advisor: Prof. Camilla Colombo
Co-advisors: Mathilda Bolis, Yeerang Lim
Academic Year: 2025-26

Copyright © 2026, Andrea Dal Passo.
All rights reserved.

This work is original and was written by the author, Andrea Dal Passo. All non-original information taken from previous works is acknowledged and cited in the Bibliography.

When referring to this work, full bibliographic details must be given, i.e.
Andrea Dal Passo (2026). *Analysis of Breakup Events along Earth-Moon L2 Halo Orbits and Cislunar Disposal Trajectories*. Politecnico di Milano, Milan, Italy.
Supervisor: Camilla Colombo, Co-supervisors: Mathilda Bolis and Yeerang Lim.

Printed in Italy

Abstract

The expected increase in the number of cislunar missions raises new challenges for space safety and sustainability. In this context, fragmentation events may pose a relevant hazard since the resulting debris evolution is governed by the nonlinear dynamics of the Earth–Moon system. This thesis investigates breakup events along southern Earth–Moon L_2 Halo orbits and cislunar disposal trajectories associated with the unstable manifold of a reference Near Rectilinear Halo Orbit, with the aim of identifying the dynamical mechanisms governing debris transport. The debris population is generated using the NASA Standard Breakup Model, while the Circular Restricted Three-Body Problem is adopted as the fundamental dynamical model. The methods employed to characterise debris evolution include trajectory analyses, debris outcome maps, post-breakup Jacobi constant distributions, dynamical metrics, and finite-time Lyapunov exponents. For the Halo family, the results show that debris transport is strongly affected by both the breakup phase angle and the stability properties of the parent orbit. In particular, the analysis reveals distinct orbital regions where different dynamical mechanisms govern the evolution of the generated fragments. For breakup events along cislunar disposal trajectories, the debris evolution is instead coherently shaped by the unstable manifold dynamics. In this case, fragments tend to follow the natural transport pathways after the breakup, with later events along the disposal trajectories generally favouring transport outside the Earth–Moon sphere of influence. This study improves the dynamical understanding of cislunar breakup events, supporting the definition of safety and mitigation strategies and the development of future Space Situational Awareness capabilities in the Earth–Moon system. This thesis is part of the work developed under agreement No. 2023-50-HH.0 for the project “Detriti spaziali e sostenibilità delle attività spaziali a lungo-termine”, established between ASI and INAF, contributing to the activities of the IADC.

Keywords: Cislunar space, breakup events, space debris, Halo orbits, unstable manifolds, Space Situational Awareness

Abstract in lingua italiana

L'aumento previsto del numero di missioni cislunari pone nuove sfide per la sicurezza e la sostenibilità spaziale. In questo contesto, gli eventi di frammentazione possono rappresentare un pericolo rilevante, poiché l'evoluzione dei detriti generati è governata dalla dinamica non lineare del sistema Terra–Luna. Questa tesi studia eventi di breakup lungo orbite Halo meridionali attorno a L_2 nel sistema Terra–Luna e lungo traiettorie di disposal cislunari associate alla varietà instabile di una Near Rectilinear Halo Orbit di riferimento, con l'obiettivo di identificare i meccanismi dinamici che governano il trasporto dei detriti. La popolazione di detriti è generata mediante il NASA Standard Breakup Model, mentre il Problema Circolare Ristretto dei Tre Corpi è adottato come modello dinamico fondamentale. I metodi impiegati per caratterizzare l'evoluzione dei detriti includono analisi delle traiettorie, mappe degli esiti dei detriti, distribuzioni della costante di Jacobi a seguito del breakup, metriche dinamiche ed esponenti di Lyapunov a tempo finito. Per la famiglia di orbite Halo, i risultati mostrano che il trasporto dei detriti è fortemente influenzato sia dall'angolo di fase del breakup sia dalle proprietà di stabilità dell'orbita del corpo progenitore. In particolare, l'analisi evidenzia regioni orbitali distinte in cui diversi meccanismi dinamici governano l'evoluzione dei frammenti generati. Per gli eventi di breakup lungo traiettorie di disposal cislunari, l'evoluzione dei detriti risulta invece modellata in modo coerente dalla dinamica della varietà instabile. In questo caso, i frammenti tendono a seguire i percorsi naturali di trasporto dopo il breakup, con eventi più avanzati lungo le traiettorie di disposal che favoriscono generalmente il trasporto al di fuori della sfera di influenza Terra–Luna. Questo studio migliora la comprensione dinamica degli eventi di breakup nello spazio cislunare, supportando la definizione di strategie di sicurezza e mitigazione e lo sviluppo di future capacità di Space Situational Awareness nel sistema Terra–Luna. Questa tesi si inserisce nell'ambito del lavoro sviluppato ai sensi dell'accordo No. 2023-50-HH.0 per il progetto "Detriti spaziali e sostenibilità delle attività spaziali a lungo-termine", istituito tra ASI e INAF e volto a contribuire alle attività dello IADC.

Parole chiave: Spazio cislunare, eventi di frammentazione, detriti spaziali, orbite Halo, varietà instabili, Space Situational Awareness

Contents

Abstract **i**

Abstract in lingua italiana **iii**

Contents **v**

1 Introduction **1**
1.1 Background . . . 1
1.2 Motivation . . . 2
1.3 State of the Art . . . 3
1.3.1 Breakup events in the near-Earth environment . . . 3
1.3.2 Breakup events in Low Lunar Orbit . . . 4
1.3.3 Breakup events in the cislunar environment . . . 5
1.3.4 Breakup events along cislunar periodic orbits . . . 6
1.3.5 Dynamical interpretation of cislunar debris transport . . . 7
1.4 Aims and novelties . . . 8
1.5 Thesis structure . . . 10

2 Fundamental models **11**
2.1 NASA Standard Breakup Model . . . 11
2.1.1 Number of fragments . . . 12
2.1.2 Characteristic length distribution . . . 13
2.1.3 Area-to-mass ratio distribution . . . 14
2.1.4 Ejection velocity distribution . . . 17
2.1.5 Mass conservation . . . 18
2.1.6 Breakup model scheme . . . 18
2.2 Circular Restricted Three-Body Problem . . . 19
2.2.1 Reference frames and coordinate transformations . . . 20
2.2.2 Equations of motion in the inertial frame . . . 22

2.2.3 Equations of motion in the rotating frame . . . 24
2.2.4 Equilibrium solutions . . . 26
2.2.5 Integral of the motion . . . 28
2.2.6 Zero Velocity Surfaces . . . 29
2.3 Fundamental variational relationships . . . 32
2.3.1 Definition of the State Transition Matrix . . . 32
2.3.2 Computation of the STM: finite differences . . . 33
2.3.3 Computation of the STM: variational approach . . . 35
2.4 Numerical computation of periodic orbits . . . 37
2.4.1 Family of Halo orbits . . . 37
2.4.2 Differential correction . . . 38
2.4.3 Numerical continuation . . . 40
2.5 Invariant manifolds . . . 41
2.6 Stability and chaos indicators . . . 46
2.6.1 Linear stability and stability index . . . 46
2.6.2 Cauchy-Green Strain Tensor . . . 47
2.6.3 Finite-Time Lyapunov Exponent . . . 48

3 Simulation setup **49**
3.1 Reference breakup scenario . . . 49
3.2 Breakup framework for Halo orbits . . . 51
3.3 Breakup framework for disposal trajectories . . . 54

4 Analysis of results **57**
4.1 Breakup events on Halo orbits . . . 57
4.1.1 Debris trajectory evolution . . . 57
4.1.2 Debris event counters . . . 60
4.1.3 Post-breakup Jacobi constant distribution . . . 70
4.1.4 Phase angle dependence of debris range . . . 71
4.1.5 TNB velocity projections and debris range . . . 72
4.1.6 FTLE evolution of debris trajectories . . . 74
4.2 Breakup events on cislunar disposal trajectories . . . 77
4.2.1 Debris trajectory evolution . . . 77
4.2.2 Debris event counters . . . 78
4.2.3 Global dependence of debris event counters . . . 81
4.2.4 FTLE evolution of debris trajectories . . . 83

5 Conclusions **87**

5.1 Summary and contributions 87
5.2 Future developments 88

Bibliography **91**

A Appendix A **101**

B Appendix B **105**

List of Figures **107**

List of Tables **109**

Acronyms **111**

Acknowledgements **113**

1 | Introduction

1.1. Background

The Moon is the next frontier of space exploration and the number of missions operating in the cislunar environment is expected to increase in the coming years [1]. Space agencies and private companies have expressed a clear interest in leveraging the cislunar region and its resources for scientific, commercial, economic, military and geopolitical purposes [2]. In recent years, this renewed attention has been accompanied by a paradigm shift in lunar exploration, moving from isolated missions towards more coordinated architectures. Several international programmes are currently aiming to establish a long-term human presence in lunar orbit and on the lunar surface [3]. The Artemis programme is one of the clearest examples of this new direction, in which lunar exploration is part of a broader strategy for sustained activities in the Earth–Moon system [4].

This renewed interest in lunar exploration is driven by different factors. From a scientific perspective, the lunar surface preserves a unique record of the early history of the Solar System and provides access to geological environments that cannot be studied on Earth [5]. From an exploration perspective, the Moon represents a nearby proving ground for technologies and operational capabilities required for future deep-space missions [6]. In addition, the possible use of local resources, such as water ice in permanently shadowed regions and oxygen extracted from lunar regolith, may support future surface activities and space transportation [7].

In parallel with these long-term exploration architectures, a growing number of supporting missions and infrastructures will be required to sustain operations in the Earth–Moon system. These may include satellites and services for navigation, communication, data relay, Space Situational Awareness (SSA), Space Traffic Management (STM) and logistics support [8]. As a consequence, the cislunar region is expected to evolve from a sparsely populated domain into a complex operational ecosystem. This increase in activity also raises questions about the long-term sustainability of the cislunar environment, given the space debris challenges already observed around Earth.

1.2. Motivation

The current space debris problem around Earth shows how the long-term sustainability of an orbital environment can be compromised by the progressive accumulation of inactive objects [9]. This evolution is illustrated in Fig. 1.1, which shows the historical growth of catalogued objects in Earth orbit by object type.

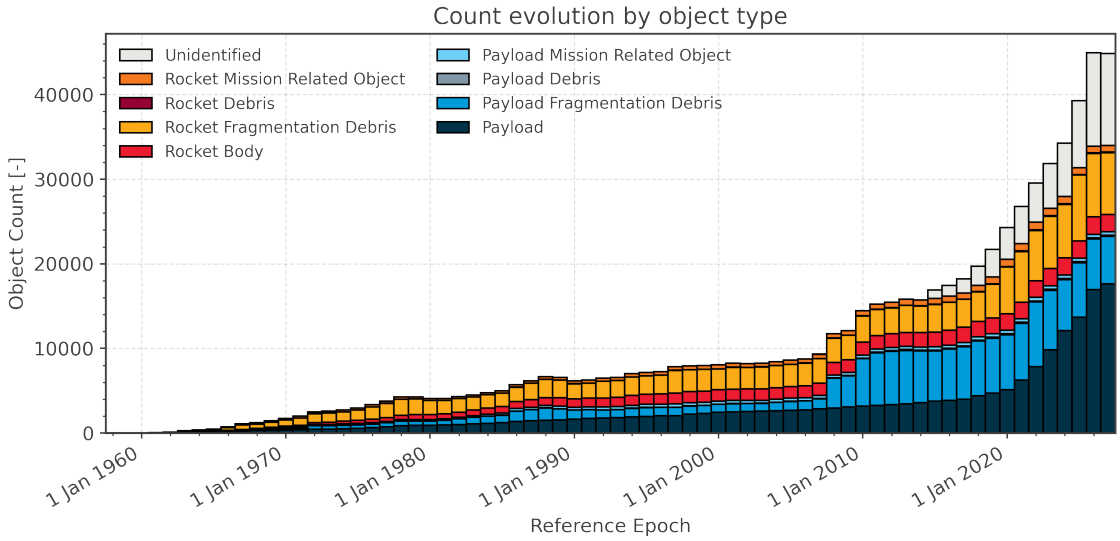


Figure 1.1: Evolution of catalogued objects in Earth orbit by object type [9].

Breakup events are particularly relevant because a single collision or explosion can generate a large population of fragments, many of which may be difficult to track while still posing a threat to operational spacecraft. For this reason, the near-Earth space debris environment has been extensively studied, leading to the development of mitigation strategies that need to be considered from the earliest stages of mission design [10–12].

A similar concern is now emerging in the cislunar environment, where the expected growth of lunar missions is likely to create an increasingly populated operational ecosystem. In this region, the debris problem is particularly complex to study because of the highly nonlinear dynamics of the Earth–Moon system and the current limitations in tracking small fragments at large distances from Earth. As a result, small differences in the breakup location or ejection velocity may lead to very different outcomes.

For these reasons, a dedicated analysis of spacecraft breakup events in the cislunar environment is required. In particular, periodic Halo orbits and Near Rectilinear Halo Orbits (NRHOs), together with their associated transfer and disposal trajectories, are expected to play a central role in future lunar exploration architectures. Understanding how debris

generated along these trajectories evolves is essential to assess possible hazards, support future mitigation strategies and avoid reproducing in the Earth–Moon system the same space debris problem already observed around Earth.

1.3. State of the Art

Recent studies have started to investigate breakup events in the Earth–Moon system, representing a first effort to extend space debris analyses beyond the near-Earth environment. This section reviews the scenarios analysed in the literature, the modelling approaches adopted and the results obtained. First, an overview of the main research areas on breakup events around Earth is provided. Then, the discussion moves to breakup events in cislunar space. The reviewed works are organised according to the regions in which the fragmentation events occur, including Low Lunar Orbit (LLO), the broader cislunar environment and cislunar periodic orbits. A final subsection is dedicated to works that provide a dynamical interpretation of transport mechanisms in cislunar space.

1.3.1. Breakup events in the near-Earth environment

Breakup events around Earth have been extensively studied in recent years since they are one of the main sources of the current space debris population. A relevant aspect of these analyses is the modelling of the initial fragment cloud. The NASA Standard Breakup Model (SBM) has become one of the reference tools for this purpose, as it describes with semi-empirical distributions the number of fragments, their characteristic length, area-to-mass ratio and ejection velocity [13, 14].

Besides the generation of the initial population, several studies have also investigated the evolution of the debris cloud in Earth orbit. This aspect was initially approached by propagating individual fragments through deterministic or Monte Carlo simulations. These methods are flexible and can include complex force models, but they become computationally expensive when small fragments and long propagation times are considered. For this reason, alternative analytical, semi-analytical and probabilistic formulations were developed. In particular, continuum approaches allow the debris cloud to be described as a density distribution rather than as a collection of individual fragments. This makes it possible to assess the global evolution of the cloud and the associated collision risk more efficiently. These methods were applied to different orbital regions, including Low Earth Orbit (LEO), Highly Eccentric Orbits (HEO), Geostationary Transfer Orbits (GTO) and Geostationary Earth Orbit (GEO). The output of these studies includes density maps, effects maps and descriptions of debris cloud evolution in terms of orbital elements [15–21].

An additional area of research focuses on the reconstruction of fragmentation events. The aim is to determine the breakup epoch, the parent object and the associated fragments from observational data, typically using Two-Line Element (TLE) data. Tools such as PUZZLE and FRED were developed to address this problem by propagating the available TLE data backward in time and identifying possible common origins among fragments and parent objects [22–27]. More recently, these approaches have been integrated within OFELIA, a dedicated tool for breakup reconstruction and characterisation that supports SSA and STM activities [28, 29].

The studies of fragmentations around Earth have established the main methodological framework for the analysis of breakup events. These developments provide the natural background for the study of cislunar breakup events. However, their extension to the Earth–Moon system is not straightforward, as debris transport in cislunar space is governed by highly nonlinear dynamics. This motivates the dedicated review of the studies on cislunar breakup events presented in the following sections.

1.3.2. Breakup events in Low Lunar Orbit

Boone and Bettinger were among the first to investigate fragmentation events in LLO. In an initial study, they analysed a catastrophic spacecraft breakup in a polar lunar orbit and evaluated the collision risk posed to a notional spacecraft operating in an equatorial lunar orbit [30]. The debris population was generated using a statistical model derived from the NOAA-16 battery explosion and propagated for 1 month in high-fidelity dynamics. The collision risk was estimated using a probabilistic spacecraft survivability model. Although the hazard probability remained low, the majority of the fragments did not decay to the lunar surface within the simulated time window. This suggests that debris generated in LLO may remain a long-term source of risk.

This preliminary analysis was later extended to a larger number of LLOs using Monte Carlo simulations [31, 32]. In particular, the authors considered breakup events in polar, equatorial and frozen lunar orbits. Their objective was to characterise debris lifetime, lunar impact distributions and collision risk. The debris population was generated using the NASA SBM and propagated for 1 year with a high-fidelity model. The results showed that the longevity of debris in LLO strongly depends on the pre-breakup orbit, with fragments reaching particularly stable conditions when departing from circular polar orbits at 200 km altitude, retrograde equatorial orbits at 100 km altitude or higher and frozen lunar orbits. Although the estimated collision probabilities with other notional spacecraft were small, several close approaches within a few kilometres were observed.

A more general investigation of fragmentation events in LLO was then performed through an extensive Monte Carlo campaign, in which breakups were sampled over a broad set of random initial states within this region [33]. The debris population was again generated using the NASA SBM and propagated in high-fidelity dynamics. The resulting population, including nearly 500,000 fragments, was propagated for 5 years, with a smaller subset extended to 10 years. This study showed that a significant fraction of debris remained in lunar orbit after several years. The decay rate was found to be strongly dependent on the pre-breakup perilune altitude and inclination, and it tended to slow down after the first few years. These results indicate that LLOs are not self-cleaning on short timescales, since some fragments may enter relatively stable dynamical regimes.

1.3.3. Breakup events in the cislunar environment

Boone and Bettinger also addressed breakup events and debris propagation in the broader cislunar environment. First, they investigated fragmentations near the collinear Earth–Moon Lagrange points, considering explosions in the vicinity of L_1 and L_2 [34]. The debris population was again generated using a statistical model derived from the NOAA-16 battery explosion and propagated with a four-body dynamical model. The risk to the Lunar Gateway, to spacecraft located near L_1 and L_2, and to vehicles on low-energy lunar transfers was evaluated using a probabilistic survivability model based on the local debris density. Their results indicated generally low collision risks, but also showed that debris may accumulate near the Moon and along the manifold structures of the Earth–Moon system, especially for breakup events occurring near L_1.

The regions around the stable Lagrange points were then analysed in a study on the natural debris environment near L_4 and L_5 [35]. Although artificial breakup fragments were not considered, particle populations representative of the Kordylewski clouds were propagated using three- and four-body trajectory models. The collision risk posed to a notional spacecraft was assessed using a survivability model. The estimated risk was extremely low for the assumed particle densities, but the simulations showed that solar perturbations can produce periodic variations in particle concentration and relative velocity. This study is also relevant to cislunar breakup analyses, since it applies a similar propagation and risk assessment framework to natural particle populations in the Earth–Moon system.

Boone and Bettinger further extended the analysis of breakup events to representative cislunar trajectories, considering three relevant case studies: an Apollo-like transfer, an L_1 manifold trajectory, and explosions at the stable L_4 and L_5 points [36, 37]. These trajectories were obtained within a four-body dynamical framework, except for the manifold

case, which was modelled using the Circular Restricted Three-Body Problem (CR3BP). The spacecraft vulnerability was evaluated with two different models: a logistic model depending on fragment mass and a ballistic limit model accounting for both fragment mass and relative velocity. The Apollo-like transfer case represented the most critical scenario for near-Earth orbital regions, since fragments could return towards Earth and cross geosynchronous altitudes at high relative speeds. Conversely, the L_1 manifold and L_4/L_5 cases affected mainly spacecraft located in the cislunar environment.

1.3.4. Breakup events along cislunar periodic orbits

Boone et al. provided an initial characterisation of breakup events near the Lunar Gateway reference NRHO [38]. The aim of their study was to characterise debris residence near the parent orbit, lunar surface impact locations and conjunction risk for spacecraft operating in the same region. The debris population was generated using the NASA SBM and propagated in GMAT using an ephemeris model. The results showed that close approaches within 10 km occurred only in a small fraction of the simulated cases, although encounters at larger distances were more frequent and could still be operationally relevant because of the difficulty of tracking small debris at lunar distances. This study was later extended to a large lunar Distant Retrograde Orbit (DRO), similar to the one used during Artemis I [39]. The analyses showed that debris in the NRHO tends to disperse rapidly from the reference orbit, while fragments in the DRO can remain stable over longer timescales, with part of the population still close to the original orbit after 10 years.

Wilmer et al. extended the analysis of breakup events considering five large cislunar orbits that may be used for future SSA and STM missions [40, 41]. These trajectories included four custom periodic orbits designed in the CR3BP and one quasi-periodic trajectory based on the IBEX mission. Eight catastrophic breakup events were simulated along each orbit. The debris population was generated using a statistical model derived from the NOAA-16 battery explosion and propagated in the Bicircular Restricted Four-Body Problem (BCR4BP). The collision risk was evaluated using a spacecraft survivability model, considering both a notional spacecraft operating on the same periodic orbit and other relevant regions of cislunar space. The results showed that the probability of critical damage to these targets is very small, while the most relevant consequences are associated with the orbital regions around Earth and Moon.

Wetterer et al. investigated debris generated by breakup events along a limited set of northern Earth–Moon L_1 and L_2 Halo orbits [42]. Different breakup locations and ejection speeds were considered to study the sensitivity of the debris evolution to the parent

trajectory and initial conditions. The fragments were generated with an idealised breakup model and propagated in GMAT with an ephemeris model. The resulting population was classified into lunar vicinity, sublunar regions, superlunar regions, impacts and escaping trajectories. The results showed that debris dynamics is mainly governed by the parent orbit, breakup location and instability properties. The debris cloud was also found to evolve preferentially along the unstable manifold of the parent orbit.

Guardabasso et al. addressed cislunar debris mitigation from a mission design perspective, developing tools to support disposal and sustainability assessments for future lunar missions. Their first studies characterised the Earth–Moon dynamical environment and investigated possible end-of-life disposal strategies [43, 44]. Periodic orbits in the CR3BP, including NRHOs, Halo orbits and DROs, were used to build dynamical maps linking impulsive manoeuvres to outcomes such as lunar impact, Earth re-entry, Earth–Moon escape or long-term residence within the cislunar region. The methodology was then extended using a Sun–Earth–Moon dynamical model and GPU parallelisation, making it possible to propagate larger sets of perturbed initial conditions over longer time spans [45]. Using the same framework, accidental fragmentation events along a southern Earth–Moon L_2 NRHO, a larger Halo orbit of the same family, and a DRO were also analysed [46]. The results showed that NRHO and Halo breakups tend to produce many lunar impacts and Earth–Moon escapes, whereas the DRO case exhibited a more stable debris population.

1.3.5. Dynamical interpretation of cislunar debris transport

Black and Frueh started to investigate cislunar breakup events from a more dynamical perspective, with the aim of predicting debris behaviour without relying only on large numerical propagations [47, 48]. First, their analyses focused on fragmentation events along planar Earth–Moon L_2 Lyapunov orbits within the CR3BP dynamics. They used Poincaré maps, Jacobi constant (JC) classification and Zero Velocity Curves (ZVCs) to identify the regions of the cislunar space that fragments could access after the breakup event. Initially, constant energy and constant ejection velocity fragmentations were considered. Then, a modified NASA SBM was used to simulate a more realistic explosion scenario. This framework was later extended to Earth–Moon L_2 Halo orbits, where stretching directions and momentum indicators were also used to study the debris dispersion [49].

Bolis et al. investigated the dynamical behaviour of several families of cislunar periodic orbits from a stability and chaoticity perspective [50]. Their study combined Poincaré maps, stability index and maximum local Lyapunov exponent to characterise the Earth–Moon phase space within the CR3BP dynamics. This dynamical framework was later

extended to end-of-life disposal analyses for Lagrangian Point Orbits (LPOs). In this case, the unstable manifold dynamics, energy-based criteria and ZVCs were exploited to design low-cost disposal trajectories using heliocentric no-return and lunar impact solutions [51, 52]. These methodologies can also be extended to the study of cislunar breakup events, since the same dynamical structures that govern orbital stability and chaotic transport may also influence the dispersion of the generated debris fragments.

1.4. Aims and novelties

The existing literature highlights the need to extend the analysis of spacecraft breakup events across a wider range of cislunar periodic orbits, to better understand the complex dynamics governing debris evolution. In particular, fragmentation events along the southern Earth–Moon L_2 Halo family and NRHOs require a deeper investigation, as these orbits represent the primary candidates for future exploration missions. Moreover, given the expected increase in traffic within the Earth–Moon system, breakup events occurring along relevant cislunar transfer and disposal trajectories also need to be addressed. Finally, as most of the reviewed literature relies mainly on numerical simulations, there is a clear need to extend the dynamical analyses by introducing additional tools. For example, stability and chaos indicators may be used to support the interpretation and preliminary prediction of debris evolution at a reduced computational cost.

The objectives of this thesis can be stated as follows:

- The first contribution consists of extending the numerical analysis of breakup events to the entire southern Earth–Moon L_2 Halo family. Instead of focusing only on a limited set of individual reference orbits, the outcomes of fragmentation events are investigated across the family, in order to assess how the location of the breakup and the stability properties of the parent orbit influence the subsequent debris evolution. Particular attention is given to the NRHO region, due to its relevance for future cislunar missions and long-term architectures.
- The second contribution consists of extending the analysis of fragmentation events to relevant disposal trajectories associated with the unstable invariant manifold of a reference NRHO. These trajectories represent natural departure channels from cislunar periodic orbits and are relevant for end-of-life strategies in the Earth–Moon system. Accordingly, it is important to assess whether debris generated along these preferential pathways could congest the manifold tubes and pose a potential hazard to future spacecraft exploiting them for low-energy transfers or disposal operations.

- The third contribution is methodological and consists of introducing a dynamical interpretation of debris evolution based on flow-informed methods, including stability and chaos indicators. These tools are used to relate the observed debris behaviour to the underlying dynamical structure, highlighting the role of local instability and invariant manifolds in shaping the evolution of the debris cloud. The objective is to move from a purely statistical description of breakup outcomes towards a dynamical understanding of the mechanisms that govern debris dispersion in cislunar periodic orbits and disposal trajectories.

The workflow required to accomplish the objectives of this thesis can be formulated as a set of guiding questions, reported below. In this way, the broad research topic is decomposed into specific blocks that support the development of this work. The following questions can be grouped into different thematic areas: questions (1–3) address the breakup modelling and the properties of the generated debris; questions (4–6) focus on the underlying dynamical framework and orbital computation; questions (7–9) concern the analysis of the results through numerical and dynamical characterisation.

1. Which breakup model is the most representative for simulating fragmentation events in the cislunar environment?
2. What are the physical characteristics (e.g., number of fragments, characteristic length, area-to-mass ratio, ejection velocity) of the generated debris population?
3. What are the initial conditions of each debris fragment following a breakup event, in terms of state vectors in the non-dimensional Earth–Moon rotating frame?
4. Which dynamical model is the most representative to describe the debris evolution in the cislunar environment?
5. Which subset of periodic Halo orbits and cislunar disposal trajectories is most suitable for providing a comprehensive analysis of breakup events in cislunar space?
6. How should the breakup location be selected along each periodic Halo orbit and each cislunar disposal trajectory?
7. What is the statistical spatial distribution of the debris generated by a breakup event across the different cislunar regions?
8. What are the dynamical mechanisms and dependencies governing debris evolution from breakup events along periodic Halo orbits and cislunar disposal trajectories?
9. How do stability and chaos indicators make it possible to predict debris behaviour without excessive computational cost?

1.5. Thesis structure

This thesis is organised as follows.

Chapter 2 introduces the fundamental theoretical and numerical models used throughout the work. It first presents the breakup model adopted to generate the debris population and the dynamical framework used to describe its evolution in the Earth–Moon system. The variational relationships required to propagate infinitesimal perturbations are then recalled, providing the basis for the numerical computation of periodic Halo orbits and their invariant manifolds. Finally, stability and chaos indicators are discussed.

Chapter 3 defines the simulation setup adopted for the analyses. The reference breakup scenario is selected and the resulting debris population is characterised. The parent Halo orbits and cislunar disposal trajectories considered for the fragmentation events are then identified. Finally, the cislunar breakup framework is presented, describing how the debris population is initialised, propagated and analysed.

Chapter 4 presents the results of the cislunar breakup simulations. The analysis first focuses on fragmentation events along a single reference NRHO, combining a numerical characterisation of debris evolution with a dynamical interpretation of the observed behaviour. The investigation is then extended to the entire family of southern Earth–Moon L_2 Halo orbits, in order to assess how the breakup location and the stability properties of the parent orbit affect debris dispersion. Finally, breakup events associated with unstable manifold trajectories are analysed, highlighting the role of natural transport mechanisms in shaping fragment evolution.

Chapter 5 concludes the thesis by summarising the main findings and contributions of the work. The limitations of the adopted methodology are then discussed, and possible directions for future developments are identified.

2 | Fundamental models

This chapter introduces the theoretical and numerical foundations adopted to model fragmentation events and analyse the evolution of the resulting debris in the cislunar environment. First, the NASA SBM is presented as the statistical framework used to generate the debris population produced by a breakup event. The CR3BP is then introduced as the reference dynamical model for describing the motion of fragments in the Earth–Moon system. Subsequently, the variational relationships required to propagate infinitesimal perturbations are recalled, providing the basis for the numerical computation of periodic Halo orbits and their associated invariant manifolds. Finally, the stability and chaos indicators adopted to characterise the dynamical behaviour of both the reference orbits and the debris trajectories are discussed.

2.1. NASA Standard Breakup Model

The NASA SBM provides a statistical description of the debris cloud generated by an orbital fragmentation event, such as an explosion or a collision. Implemented within the NASA long-term orbital debris environment model EVOLVE 4.0, this framework is based on semi-empirical relationships derived from ground-based experimental campaigns and extensive analyses of on-orbit breakup data [13].

In particular, the revision of the model relied on:

- the deliberate hypervelocity collisions in low Earth orbit involving Solwind (P-78) in 1985 [53] and USA-19 (Delta-180) in 1986 [54, 55];
- the ground-based Satellite Orbital Debris Characterization Impact Test (SOCIT) series, performed in 1991 and 1992 [56];
- the Ariane upper stage sub-scale explosion tests supervised by ESA [57];
- an extensive compilation of historical orbital data, including TLE sets, used to infer ejection-velocity and area-to-mass-ratio distributions [58].

The model defines the number N, the characteristic length L, the area-to-mass ratio A/M and the ejection velocity Δv of the fragments generated by a breakup event. These quantities are the minimal set of parameters required to reconstruct a representative debris cloud, allowing its subsequent propagation and analysis in orbital environment models.

2.1.1. Number of fragments

The first quantity introduced by the NASA SBM is the cumulative number of fragments with characteristic length greater than or equal to a prescribed lower bound L_0. Starting from the formulation introduced in [13] and following the compact probabilistic notation adopted in [17, 59], its general expression is given by:

$$N(L_0) = k \left(\frac{L_0[\mathrm{m}]}{1[\mathrm{m}]} \right)^{-\beta} \tag{2.1}$$

where $k > 0$ and $\beta > 0$ are dimensionless model parameters that depend on the breakup type and on the physical properties of the objects involved.

For collision events, the cumulative number of fragments is expressed as:

$$N(L_0) = 0.1 \left(\frac{M_e[\mathrm{kg}]}{1[\mathrm{kg}]} \right)^{0.75} \left(\frac{L_0[\mathrm{m}]}{1[\mathrm{m}]} \right)^{-1.71} \tag{2.2}$$

where M_e is the reference mass associated with the collision. Its definition depends on whether the collision is classified as catastrophic or non-catastrophic. A collision is considered catastrophic when the impact causes the complete fragmentation of both the projectile and the target. Conversely, in a non-catastrophic collision the larger object is assumed not to be fully disrupted [13, 59]. Within the NASA SBM, this classification is based on the impact kinetic energy per unit target mass, defined as:

$$\epsilon = \frac{1}{2} \frac{m_p}{m_t} v_c^2 \tag{2.3}$$

where m_p and m_t are the masses of the projectile and the target, respectively, while v_c is the relative impact velocity. As a rule of thumb, a collision is conventionally classified as catastrophic when $\epsilon \geq 40\,\mathrm{Jg}^{-1}$. Accordingly, the reference mass M_e is computed as:

$$M_e[\mathrm{kg}] = \begin{cases} m_t[\mathrm{kg}] + m_p[\mathrm{kg}] & \text{if catastrophic collision} \\ m_p[\mathrm{kg}] \left(\dfrac{v_c[\mathrm{km/s}]}{1[\mathrm{km/s}]} \right)^2 & \text{if non-catastrophic collision} \end{cases} \tag{2.4}$$

For explosion events, the cumulative number of fragments is expressed as:

$$N(L_0) = 6S \left(\frac{L_0[\mathrm{m}]}{1[\mathrm{m}]} \right)^{-1.6} \tag{2.5}$$

where $S \in [0.1, 1]$ is an empirically derived, dimensionless scaling factor that depends on the type and mass of the exploding object.

Table 2.1 summarizes the values of the parameters k and β appearing in Eq. (2.1) for the different breakup types. In the following, the normalization in the units (e.g., $L_0[\mathrm{m}]/1[\mathrm{m}]$) is omitted. Unless otherwise specified, all variables are expressed in SI units.

Table 2.1: Values of the parameters k and β for different breakup types.

Fragmentation	k	β
Collision	$0.1 M_e^{0.75}$	1.71
Explosion	$6S$	1.6

The expressions reported above provide the cumulative number of fragments with characteristic length greater than or equal to a prescribed lower bound L_0. However, in practical implementations, the debris population is usually generated over a finite characteristic-length interval $[L_0, L_1]$, where L_1 denotes the prescribed upper bound. Therefore, the number of fragments within the considered size range is obtained as:

$$N = N(L_0) - N(L_1) \tag{2.6}$$

In the following, N denotes the number of fragments in the selected size interval.

2.1.2. Characteristic length distribution

Once the number of fragments has been defined, a distribution in characteristic length is introduced to assign an individual size to each fragment [59]. This is obtained by converting Eq. (2.1) into a probability density function in L over the interval $[L_0, L_1]$, as:

$$p_L = \frac{k\beta}{N} L^{-(\beta+1)} \qquad \forall\ L_0 \leq L \leq L_1 \tag{2.7}$$

By substituting Eqs. (2.1) and (2.6) into the previous expression, p_L can be written as:

$$p_L = \beta \frac{L^{-(\beta+1)}}{L_0^{-\beta} - L_1^{-\beta}} \qquad \forall\ L_0 \leq L \leq L_1 \tag{2.8}$$

It follows that p_L is independent of the number of fragments. Eq. (2.8) can be reformulated in terms of the logarithm to base 10 of the characteristic length, $\lambda = \log_{10}(L)$, as:

$$p_\lambda = \ln(10) 10^\lambda p_L(10^\lambda) \qquad \forall\ \lambda_0 \leq \lambda \leq \lambda_1 \tag{2.9}$$

Combining Eqs. (2.8) and (2.9), the following expression is obtained:

$$p_\lambda = \ln(10)\beta \frac{10^{-\beta\lambda}}{10^{-\beta\lambda_0} - 10^{-\beta\lambda_1}} \qquad \forall\ \lambda_0 \leq \lambda \leq \lambda_1 \tag{2.10}$$

The corresponding cumulative distribution function can be computed as:

$$P_\lambda = \int_{\lambda_0}^{\lambda} p_\lambda(\lambda')\,\mathrm{d}\lambda' = \frac{10^{-\beta\lambda_0} - 10^{-\beta\lambda}}{10^{-\beta\lambda_0} - 10^{-\beta\lambda_1}} \tag{2.11}$$

An explicit sampling law for λ is then obtained by inverting Eq. (2.11) as:

$$\lambda = -\frac{1}{\beta}\log_{10}\left[10^{-\beta\lambda_0} - P_\lambda\left(10^{-\beta\lambda_0} - 10^{-\beta\lambda_1}\right)\right] \tag{2.12}$$

where P_λ is uniformly sampled from $[0, 1]$ for each fragment of the debris population.

2.1.3. Area-to-mass ratio distribution

The distribution in area-to-mass ratio depends on the fragment size and, for sufficiently large fragments, also on the type of parent object. Fragments with $L > 11\,\mathrm{cm}$ are differentiated depending on whether they originate from a payload or from a rocket body, whereas a single distribution is adopted for small fragments [13]. Let $\chi = \log_{10}(A/M)$ be the logarithm to base 10 of the area-to-mass ratio. Following the compact probabilistic notation adopted in [17], the conditional probability density function of χ, for a given λ, can be written as a weighted sum of normal distributions:

$$p_{\chi|\lambda} = \sum_{i=1}^{N_c} \alpha_i(\lambda)\,\mathcal{N}\left(\mu_\chi^{(i)}(\lambda), \sigma_\chi^{(i)}(\lambda)\right) \tag{2.13}$$

where $\alpha_i(\lambda)$ are the weighting coefficients, $\mathcal{N}$ denotes the normal probability density function, $\mu_\chi^{(i)}(\lambda)$ and $\sigma_\chi^{(i)}(\lambda)$ are the mean and standard deviation of the corresponding normal component, and N_c is the number of components. For each fragment, once λ has been sampled, χ is generated by first selecting a normal component according to the weights $\alpha_i(\lambda)$ and then sampling from the corresponding distribution. The physical area-to-mass ratio is finally recovered as $A/M = 10^\chi$.

For rocket bodies, the model parameters for fragments with $L > 11\,\text{cm}$ are:

$$\alpha_1 = \begin{cases} 1 & \lambda \leq -1.4 \\ 1 - 0.3571(\lambda + 1.4) & -1.4 < \lambda < 0 \\ 0.5 & \lambda \geq 0 \end{cases} \tag{2.14a}$$

$$\mu_\chi^{(1)} = \begin{cases} -0.45 & \lambda \leq -0.5 \\ -0.45 - 0.9(\lambda + 0.5) & -0.5 < \lambda < 0 \\ -0.9 & \lambda \geq 0 \end{cases} \tag{2.14b}$$

$$\sigma_\chi^{(1)} = 0.55 \tag{2.14c}$$

$$\alpha_2 = 1 - \alpha_1 \tag{2.14d}$$

$$\mu_\chi^{(2)} = -0.9 \tag{2.14e}$$

$$\sigma_\chi^{(2)} = \begin{cases} 0.28 & \lambda \leq -1.0 \\ 0.28 - 0.1636(\lambda + 1) & -1.0 < \lambda < 0.1 \\ 0.1 & \lambda \geq 0.1 \end{cases} \tag{2.14f}$$

For payloads, the model parameters for fragments with $L > 11\,\text{cm}$ are:

$$\alpha_1 = \begin{cases} 0 & \lambda \leq -1.95 \\ 0.3 + 0.4(\lambda + 1.2) & -1.95 < \lambda < 0.55 \\ 1 & \lambda \geq 0.55 \end{cases} \tag{2.15a}$$

$$\mu_\chi^{(1)} = \begin{cases} -0.6 & \lambda \leq -1.1 \\ -0.6 - 0.318(\lambda + 1.1) & -1.1 < \lambda < 0 \\ -0.95 & \lambda \geq 0 \end{cases} \tag{2.15b}$$

$$\sigma_\chi^{(1)} = \begin{cases} 0.1 & \lambda \leq -1.3 \\ 0.1 + 0.2(\lambda + 1.3) & -1.3 < \lambda < -0.3 \\ 0.3 & \lambda \geq -0.3 \end{cases} \tag{2.15c}$$

$$\alpha_2 = 1 - \alpha_1 \tag{2.15d}$$

$$\mu_{\chi}^{(2)} = \begin{cases} -1.2 & \lambda \leq -0.7 \\ -1.2 - 1.333(\lambda + 0.7) & -0.7 < \lambda < -0.1 \\ -2.0 & \lambda \geq -0.1 \end{cases} \tag{2.15e}$$

$$\sigma_{\chi}^{(2)} = \begin{cases} 0.5 & \lambda \leq -0.5 \\ 0.5 - (\lambda + 0.5) & -0.5 < \lambda < -0.3 \\ 0.3 & \lambda \geq -0.3 \end{cases} \tag{2.15f}$$

For fragments with $L < 8\,\text{cm}$, the model adopts an identical single-distribution representation for both rocket bodies and payloads, with parameters:

$$\alpha_1 = 1 \tag{2.16a}$$

$$\mu_{\chi}^{(1)} = \begin{cases} -0.3 & \lambda \leq -1.75 \\ -0.3 - 1.4(\lambda + 1.75) & -1.75 < \lambda < -1.25 \\ -1.0 & \lambda \geq -1.25 \end{cases} \tag{2.16b}$$

$$\sigma_{\chi}^{(1)} = \begin{cases} 0.2 & \lambda \leq -3.5 \\ 0.2 + 0.1333(\lambda + 3.5) & \lambda > -3.5 \end{cases} \tag{2.16c}$$

Following the approach proposed in [59], for the intermediate size range $L \in [8, 11]\,\text{cm}$ a linear transition in λ is employed:

$$p_{\chi|\lambda}^{\text{transition}} = \alpha_\lambda\, p_{\chi|\lambda}^{\text{large}} + (1 - \alpha_\lambda)\, p_{\chi|\lambda}^{\text{small}} \tag{2.17}$$

where the interpolation factor α_λ is defined as:

$$\alpha_\lambda = \frac{\lambda - \lambda_s}{\lambda_l - \lambda_s} \qquad \forall\, \lambda_s = \log_{10}(0.08) \leq \lambda \leq \lambda_l = \log_{10}(0.11) \tag{2.18}$$

Given the characteristic length, the cross-sectional area A_x is computed as:

$$A_x = \begin{cases} 0.540424\, L^2 & \text{if } L < 0.00167 \text{ m} \\ 0.556945\, L^{2.0047077} & \text{if } L \geq 0.00167 \text{ m} \end{cases} \tag{2.19}$$

Finally, the conversion to mass can simply be obtained by:

$$M = \frac{A_x}{A/M} \tag{2.20}$$

2.1.4. Ejection velocity distribution

The distribution of the ejection velocity depends on the fragment area-to-mass ratio and on the breakup type. Let $\nu = \log_{10}(\Delta v)$ be the logarithm to base 10 of the ejection velocity. The conditional probability density function of ν, for a given χ, is modelled as a normal distribution [13, 17, 59]:

$$p_{\nu|\chi} = \mathcal{N}(\mu_\nu(\chi), \sigma_\nu(\chi)) \tag{2.21}$$

where $\mu_\nu(\chi)$ and $\sigma_\nu(\chi)$ are the mean and standard deviation of the normal distribution, respectively, and depend on the breakup type.

For collision events, the model parameters are given by:

$$\mu_\nu = 0.9\chi + 2.9 \tag{2.22a}$$

$$\sigma_\nu = 0.4 \tag{2.22b}$$

while for explosion events, the corresponding parameters are:

$$\mu_\nu = 0.2\chi + 1.85 \tag{2.23a}$$

$$\sigma_\nu = 0.4 \tag{2.23b}$$

The corresponding physical ejection velocity is then recovered as $\Delta v = 10^\nu$.

Finally, as the probability density function in Eq. (2.21) provides only the magnitude of the ejection velocity, a random direction is assigned to each fragment by assuming an omnidirectional breakup event:

$$\Delta \boldsymbol{v} = \begin{pmatrix} \Delta v \sqrt{1-u^2} \cos\theta \\ \Delta v \sqrt{1-u^2} \sin\theta \\ \Delta v \, u \end{pmatrix} \tag{2.24}$$

where u is a random number uniformly sampled between -1 and 1, and θ is a random angle uniformly sampled between 0 and 2π.

2.1.5. Mass conservation

The NASA SBM is not inherently mass conserving. Therefore, an additional correction is required to ensure that the total mass of the generated fragments is consistent with the initial mass involved in the breakup event. This is achieved either by removing fragments when the sampled debris population leads to an excess mass, or by introducing additional fragments when the generated mass is insufficient. Following the considerations reported in [14], the latter case is treated differently depending on the breakup type.

For explosion events, the nominal distribution of fragments is applied over the characteristic length interval from 1 mm to 1 m, following the power law reported in Eq. (2.5). Mass conservation is enforced by adding two to eight fragments larger than 1 m. These larger fragments are representative of more massive components farther from the explosion centre (e.g., remnants of equipment shelves, pressurant tanks, nozzle bells) that do not necessarily follow the power law distribution.

Collision events are implemented differently depending on whether they are classified as catastrophic or non-catastrophic. For catastrophic collisions, the nominal distribution of fragments is applied over the characteristic length interval from 1 mm up to the bin before 1 m, following the power law reported in Eq. (2.2). To enforce mass conservation, the remaining mass is assigned to several large fragments deposited in that last bin. For non-catastrophic collisions, the nominal distribution of fragments is applied from 1 mm upward, again following the power law reported in Eq. (2.2). In this case, fragments are generated until the reference collisional mass is reached, and the final fragment is assigned to a single massive fragment reminiscent of the cratered target mass.

2.1.6. Breakup model scheme

The application of the NASA SBM can be summarised as a sequential procedure for generating the initial debris cloud. Starting from the selected breakup type, parent object type and characteristic length interval, the model: (1) evaluates the number of fragments from the cumulative size distribution, (2) samples the characteristic length of each fragment, (3) assigns the corresponding area-to-mass ratio and derives the fragment mass, (4) samples the ejection velocity magnitude, (5) assigns an omnidirectional ejection direction and adds the resulting velocity increment to the parent state and (6) applies a mass balance correction when required. The resulting set of fragment states represents the initial condition for the subsequent dynamical propagation.

2.2. Circular Restricted Three-Body Problem

The CR3BP is a classical model in astrodynamics used to describe the motion of an infinitesimal body under the gravitational attraction of two massive bodies, referred to as the primaries, which revolve in circular orbits about their common centre of mass [60, 61]. This framework provides a reasonable approximation of the complex dynamics characterising the cislunar environment, where the motion of a spacecraft is primarily governed by the combined gravitational attraction of the Earth and the Moon.

The mathematical formulation of the CR3BP is based on the following assumptions:

- *Circular*: the two primaries move on circular orbits about their common centre of mass under their mutual gravitational attraction.
- *Restricted*: the third body has a negligible mass compared to the primaries and therefore does not affect their motion.
- *Three-Body*: the dynamical system consists of three bodies, namely the two massive primaries and the infinitesimal body, all treated as point masses.

In the Earth–Moon case, these approximations are representative of many astrodynamical applications, since the orbital eccentricity of the Moon is sufficiently small [62] and the mass of the spacecraft is negligible with respect to those of the primaries.

Despite its simplifying assumptions, the CR3BP remains remarkably effective for analysing the dynamical mechanisms governing the cislunar environment. When formulated in the rotating frame, the system becomes autonomous, or time-invariant, and the governing equations no longer depend explicitly on the specific simulation epoch. This provides a general and consistent framework in which the main dynamical properties are intrinsic to the model itself, rather than tied to a particular time instant. Moreover, the CR3BP admits an energy integral, known as the JC, together with the associated ZVCs. These quantities provide an energy-based interpretation of the problem and make it possible to determine dynamically accessible or forbidden regions of space. At the same time, the model allows the identification of equilibrium points, families of periodic orbits, invariant manifolds, stability and chaos indicators. These features make the CR3BP effective for interpreting transport mechanisms and identifying relevant capture and escape trajectories. Finally, its relatively simple mathematical structure also results in a low computational cost, making it particularly efficient for extensive numerical simulations. All these aspects are discussed in further detail in the following sections.

In conclusion, the CR3BP is well suited to preliminary design, parametric analyses and the interpretation of complex behaviours in cislunar dynamics that would be much harder to isolate in fully numerical models. The solutions obtained within this dynamical framework provide meaningful baseline trajectories that can subsequently be refined and validated in higher-fidelity ephemeris models for operational applications.

2.2.1. Reference frames and coordinate transformations

This section introduces the reference frames and coordinate transformations adopted to derive the equations of motion in the CR3BP. Let P_1 and P_2 denote the two primaries, with masses m_1 and m_2, respectively, and let P_3 denote the infinitesimal body of negligible mass. When the primaries have different masses, P_1 refers to the more massive body.

Let $(\hat{X}, \hat{Y}, \hat{Z})$ be an inertial reference frame with origin at the centre of mass $\mathcal{O}$ of the P_1–P_2 system, as shown in Fig. 2.1. The frame is defined such that the $\hat{X}$-$\hat{Y}$ plane coincides with the orbital plane of the primaries, while the $\hat{Z}$-axis completes a right-handed coordinate system. In this frame, $\boldsymbol{R}_1$, $\boldsymbol{R}_2$ and $\boldsymbol{R}_3$ denote the position vectors of P_1, P_2 and P_3, respectively. Moreover, $\boldsymbol{R}_{13}$ and $\boldsymbol{R}_{23}$ represent the position vectors of P_3 relative to P_1 and P_2, respectively.

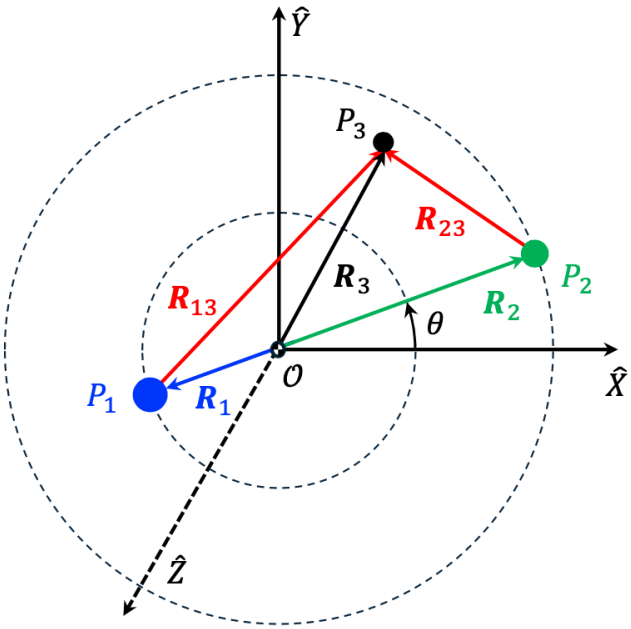


Figure 2.1: Inertial reference frame.

Let $(\hat{x}, \hat{y}, \hat{z})$ be a rotating reference frame, also centred at the centre of mass $\mathcal{O}$ of the P_1–P_2 system, as shown in Fig. 2.2. The frame is defined such that the $\hat{x}$-axis is aligned with the line joining P_1 and P_2, the $\hat{z}$-axis is perpendicular to the orbital plane of the primaries, and the $\hat{y}$-axis completes a right-handed coordinate system. The frame rotates counterclockwise about the $\hat{z}$-axis with constant angular velocity n, equal to the mean motion of the primaries with respect to the inertial frame. The inertial and rotating frames are assumed to coincide at $t = 0$. In this frame, $\boldsymbol{r}_1$, $\boldsymbol{r}_2$ and $\boldsymbol{r}_3$ denote the position vectors of P_1, P_2 and P_3, respectively. Moreover, $\boldsymbol{r}_{13}$ and $\boldsymbol{r}_{23}$ represent the position vectors of P_3 relative to P_1 and P_2, respectively.

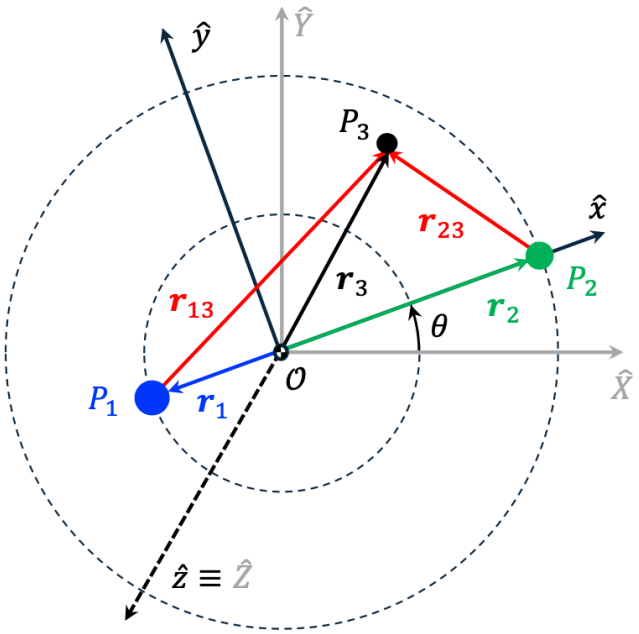


Figure 2.2: Rotating reference frame.

The transformation of the position vector between the inertial and rotating frames is now introduced. For notational simplicity, the subscript associated with the infinitesimal body is omitted throughout this section, so that the transformations are written in a more general form (i.e., $\boldsymbol{R}_3 \to \boldsymbol{R}$ and $\boldsymbol{r}_3 \to \boldsymbol{r}$). The two representations are related by:

$$\boldsymbol{R} = A(t)\boldsymbol{r} \tag{2.25}$$

where:

$$A(t) = \begin{bmatrix} \cos\theta & -\sin\theta & 0 \\ \sin\theta & \cos\theta & 0 \\ 0 & 0 & 1 \end{bmatrix} \tag{2.26}$$

is the transformation matrix of the position vector from the rotating to the inertial frame, and $\theta = nt$ is the angle between the $\hat{X}$-axis and the $\hat{x}$-axis, measured counterclockwise.

By differentiating Eq. (2.25), the transformation of the velocity vector from the rotating to the inertial frame is obtained as:

$$\begin{aligned} \dot{\boldsymbol{R}} &= \dot{A}(t)\boldsymbol{r} + A(t)\dot{\boldsymbol{r}} = \\ &= A(t)J\boldsymbol{r} + A(t)\dot{\boldsymbol{r}} = \\ &= A(t)(\dot{\boldsymbol{r}} + J\boldsymbol{r}) \end{aligned} \tag{2.27}$$

where:

$$J = \begin{bmatrix} 0 & -n & 0 \\ n & 0 & 0 \\ 0 & 0 & 0 \end{bmatrix} \tag{2.28}$$

Overall, by defining the velocity vectors as $\boldsymbol{V} \equiv \dot{\boldsymbol{R}}$ and $\boldsymbol{v} \equiv \dot{\boldsymbol{r}}$, the transformation of the state vector from the rotating to the inertial frame can be expressed as:

$$\begin{bmatrix} \boldsymbol{R} \\ \boldsymbol{V} \end{bmatrix} = C_{R\to I} \begin{bmatrix} \boldsymbol{r} \\ \boldsymbol{v} \end{bmatrix} \tag{2.29}$$

where:

$$C_{R\to I} = \begin{bmatrix} A(t) & 0 \\ A(t)J & A(t) \end{bmatrix} \tag{2.30}$$

is the transformation matrix from the rotating to the inertial frame. Observe that $C_{R\to I}$ is not an orthogonal matrix. Consequently, the inverse transformation cannot be obtained simply by taking its transpose (i.e., $C_{I\to R} \neq C_{R\to I}^{\mathrm{T}}$).

2.2.2. Equations of motion in the inertial frame

The equations of motion of the CR3BP in the inertial frame can be derived from the general formulation of the N-body problem. Consider a system of N mutually interacting bodies $(P_1, P_2, \ldots, P_N)$, all treated as point masses. Let $(m_1, m_2, \ldots, m_N)$ and $(\boldsymbol{R}_1, \boldsymbol{R}_2, \ldots, \boldsymbol{R}_N)$ be their masses and position vectors in the inertial frame, respectively. The equations of motion of a generic body P_i can be written as:

$$\frac{d^2\boldsymbol{R}_i}{dt^2} = -G\sum_{\substack{j=1 \\ j\neq i}}^{N} m_j \frac{\boldsymbol{R}_{ji}}{R_{ji}^3}, \qquad i = 1, \ldots, N \tag{2.31}$$

where:

$$\boldsymbol{R}_{ji} = \boldsymbol{R}_i - \boldsymbol{R}_j \tag{2.32}$$

is the relative vector from P_j to P_i, $G = 6.674 \cdot 10^{-11}\,\mathrm{m^3\,kg^{-1}\,s^{-2}}$ is the gravitational constant, and the time t is the independent variable.

By restricting the formulation to $N = 3$ and in accordance with the notation introduced in Sec. 2.2.1, the equations of motion of the infinitesimal body P_3 are given by:

$$\frac{d^2\boldsymbol{R}_3}{dt^2} = -Gm_1\frac{\boldsymbol{R}_{13}}{R_{13}^3} - Gm_2\frac{\boldsymbol{R}_{23}}{R_{23}^3} \tag{2.33}$$

where P_1 and P_2 are the Earth and the Moon, respectively. In the inertial frame, the position vectors of the primaries can be written as:

$$\begin{aligned} \boldsymbol{R}_1 &= -R_1\cos(nt)\hat{X} - R_1\sin(nt)\hat{Y} \\ \boldsymbol{R}_2 &= +R_2\cos(nt)\hat{X} + R_2\sin(nt)\hat{Y} \end{aligned} \tag{2.34}$$

By writing the position vector of P_3 as $\boldsymbol{R}_3 = X\hat{X}+Y\hat{Y}+Z\hat{Z}$, the relative position vectors of P_3 with respect to P_1 and P_2 can be expressed as:

$$\begin{aligned} \boldsymbol{R}_{13} &= (X + R_1\cos(nt))\hat{X} + (Y + R_1\sin(nt))\hat{Y} + Z\hat{Z} \\ \boldsymbol{R}_{23} &= (X - R_2\cos(nt))\hat{X} + (Y - R_2\sin(nt))\hat{Y} + Z\hat{Z} \end{aligned} \tag{2.35}$$

By combining Eqs. (2.33) and (2.35), the equations of motion for P_3 in the inertial frame can be written component-wise as:

$$\begin{cases} \dfrac{d^2X}{dt^2} = -Gm_1\dfrac{X + R_1\cos(nt)}{R_{13}^3} - Gm_2\dfrac{X - R_2\cos(nt)}{R_{23}^3} \\ \dfrac{d^2Y}{dt^2} = -Gm_1\dfrac{Y + R_1\sin(nt)}{R_{13}^3} - Gm_2\dfrac{Y - R_2\sin(nt)}{R_{23}^3} \\ \dfrac{d^2Z}{dt^2} = -Gm_1\dfrac{Z}{R_{13}^3} - Gm_2\dfrac{Z}{R_{23}^3} \end{cases} \tag{2.36}$$

Equation (2.36) is a nonlinear system of second-order differential equations that does not admit a closed-form analytical solution. Consequently, numerical methods must be employed to compute the time evolution of the state of P_3. Moreover, the system is non-autonomous, as the time t appears explicitly in the equations of motion.

2.2.3. Equations of motion in the rotating frame

The CR3BP is commonly formulated in the rotating frame, as this representation offers several advantages which are discussed throughout this section. Different derivations can be employed to obtain the corresponding equations of motion. In this work, a Newtonian approach is adopted, exploiting both the normalisation of the system and the coordinate transformation from the inertial to the rotating frame. Alternative formulations based on Lagrangian or Hamiltonian formalisms are discussed in [61].

First, the system is made nondimensional by introducing a suitable set of characteristic units. The unit of mass is defined as $m^* = m_1 + m_2$, namely the total mass of the system, while the unit of length is chosen as $l^* = R_1 + R_2$, namely the distance between the two primaries. The unit of time is selected such that the orbital period of P_1 and P_2 about their centre of mass results equal to 2π. With this choice, both the gravitational constant G and the mean motion of the primaries n become equal to unity.

This normalisation is particularly convenient as it reduces the problem to a dimensionless formulation governed by a single parameter, namely the mass parameter μ, defined as:

$$\mu = \frac{m_2}{m_1 + m_2} \tag{2.37}$$

Accordingly, the nondimensional masses of P_1 and P_2 become $\mu_1 = 1 - \mu$ and $\mu_2 = \mu$, respectively, while their corresponding nondimensional distances from the centre of mass of the system are $r_1 = \mu$ and $r_2 = 1 - \mu$. By writing the nondimensional position vector of the infinitesimal body P_3 in the rotating frame as $\boldsymbol{r}_3 = x\hat{x} + y\hat{y} + z\hat{z}$, the relative position vectors of P_3 with respect to P_1 and P_2 are given by:

$$\begin{aligned} \boldsymbol{r}_{13} &= \boldsymbol{r}_3 - \boldsymbol{r}_1 = (x + \mu)\hat{x} + y\hat{y} + z\hat{z} \\ \boldsymbol{r}_{23} &= \boldsymbol{r}_3 - \boldsymbol{r}_2 = (x + \mu - 1)\hat{x} + y\hat{y} + z\hat{z} \end{aligned} \tag{2.38}$$

Introducing the nondimensional variables and in accordance with the notation defined in Sec. 2.2.1, Eq. (2.33) can be rewritten as:

$$\frac{d^2\boldsymbol{r}_3}{dt^2} = -\frac{1-\mu}{r_{13}^3}\boldsymbol{r}_{13} - \frac{\mu}{r_{23}^3}\boldsymbol{r}_{23} \tag{2.39}$$

where the position vectors are expressed in the nondimensional rotating frame, while the derivative on the left-hand side is still expressed with respect to the inertial frame.

The relation between the inertial and rotating time derivatives is provided by the transport theorem. Applied to the position vector $\boldsymbol{r}_3$, it yields:

$$\frac{d\boldsymbol{r}_3}{dt} = \dot{\boldsymbol{r}}_3 + \boldsymbol{\omega} \times \boldsymbol{r}_3 \tag{2.40}$$

where $d\boldsymbol{r}_3/dt$ and $\dot{\boldsymbol{r}}_3$ are the first time derivatives with respect to the inertial and rotating frames, respectively, while $\boldsymbol{\omega} \times \boldsymbol{r}_3$ is the transport term associated with the rotation of the frame. Here, $\boldsymbol{\omega} = n\hat{z}$ denotes the angular velocity of the rotating frame with respect to the inertial one, with $n = 1$ in the nondimensional system.

Applying the transport theorem once again to Eq. (2.40) yields:

$$\frac{d^2\boldsymbol{r}_3}{dt^2} = \ddot{\boldsymbol{r}}_3 + 2\boldsymbol{\omega} \times \dot{\boldsymbol{r}}_3 + \boldsymbol{\omega} \times (\boldsymbol{\omega} \times \boldsymbol{r}_3) + \dot{\boldsymbol{\omega}} \times \boldsymbol{r}_3 \tag{2.41}$$

where $d^2\boldsymbol{r}_3/dt^2$ and $\ddot{\boldsymbol{r}}_3$ are the second time derivatives with respect to the inertial and rotating frames, respectively, while the remaining terms are the apparent accelerations associated with the non-inertial nature of the rotating frame. In particular, $2\boldsymbol{\omega} \times \dot{\boldsymbol{r}}_3$ is the Coriolis acceleration, $\boldsymbol{\omega} \times (\boldsymbol{\omega} \times \boldsymbol{r}_3)$ is the centrifugal acceleration, and $\dot{\boldsymbol{\omega}} \times \boldsymbol{r}_3$ is the Euler acceleration. Since in the CR3BP the rotating frame is assumed to have a constant angular velocity, it follows that $\dot{\boldsymbol{\omega}} = 0$ and thus the Euler term vanishes.

By substituting Eq. (2.41) into Eq. (2.39) and rearranging the resulting terms, the equations of motion with respect to the nondimensional rotating frame are obtained:

$$\ddot{\boldsymbol{r}}_3 = -2\boldsymbol{\omega} \times \dot{\boldsymbol{r}}_3 - \boldsymbol{\omega} \times (\boldsymbol{\omega} \times \boldsymbol{r}_3) - \frac{1-\mu}{r_{13}^3}\boldsymbol{r}_{13} - \frac{\mu}{r_{23}^3}\boldsymbol{r}_{23} \tag{2.42}$$

Expanding the cross products, Eq. (2.42) can be expressed component-wise as:

$$\begin{cases} \ddot{x} = 2\dot{y} + x - \dfrac{1-\mu}{r_{13}^3}(x+\mu) - \dfrac{\mu}{r_{23}^3}(x+\mu-1) \\ \ddot{y} = -2\dot{x} + y - \dfrac{1-\mu}{r_{13}^3}y - \dfrac{\mu}{r_{23}^3}y \\ \ddot{z} = -\dfrac{1-\mu}{r_{13}^3}z - \dfrac{\mu}{r_{23}^3}z \end{cases} \tag{2.43}$$

This system of second-order differential equations can be written in a more compact form by introducing the scalar pseudo-potential function U, defined as:

$$U = \frac{1}{2}(x^2 + y^2) + \frac{1-\mu}{r_{13}} + \frac{\mu}{r_{23}} \tag{2.44}$$

Its partial derivatives with respect to the rotating frame coordinates are:

$$\begin{cases} \dfrac{\partial U}{\partial x} = x - \dfrac{1-\mu}{r_{13}^3}(x+\mu) - \dfrac{\mu}{r_{23}^3}(x+\mu-1) \\ \dfrac{\partial U}{\partial y} = y - \dfrac{1-\mu}{r_{13}^3}y - \dfrac{\mu}{r_{23}^3}y \\ \dfrac{\partial U}{\partial z} = -\dfrac{1-\mu}{r_{13}^3}z - \dfrac{\mu}{r_{23}^3}z \end{cases} \tag{2.45}$$

By substituting these expressions into Eq. (2.43), the component-wise equations of motion in the nondimensional rotating frame become:

$$\begin{cases} \ddot{x} - 2\dot{y} = \dfrac{\partial U}{\partial x} \\ \ddot{y} + 2\dot{x} = \dfrac{\partial U}{\partial y} \\ \ddot{z} = \dfrac{\partial U}{\partial z} \end{cases} \tag{2.46}$$

Equation (2.46) can be rewritten in canonical form as a first-order dynamical system, namely $\dot{\boldsymbol{x}} = \boldsymbol{f}(\boldsymbol{x})$. As anticipated, this system is autonomous, or time-invariant, since the vector field $\boldsymbol{f}$ depends only on the state vector $\boldsymbol{x}$ and does not depend explicitly on time t. This formulation is particularly convenient as all dynamical properties are intrinsic to the model itself and are independent of the specific simulation epoch.

2.2.4. Equilibrium solutions

The CR3BP formulated in the rotating frame admits five equilibrium solutions, known as Lagrange or libration points. Their coordinates are obtained by writing the equations of motion in first-order form, $\dot{\boldsymbol{x}} = \boldsymbol{f}(\boldsymbol{x})$, and imposing the equilibrium condition $\boldsymbol{f}(\boldsymbol{x}) = 0$. By defining the state vector $\boldsymbol{x} = (x, y, z, v_x, v_y, v_z)^\top$, Eq. (2.46) becomes:

$$\begin{cases} \dot{x} = v_x \\ \dot{y} = v_y \\ \dot{z} = v_z \\ \dot{v}_x = 2v_y + \dfrac{\partial U}{\partial x} \\ \dot{v}_y = -2v_x + \dfrac{\partial U}{\partial y} \\ \dot{v}_z = \dfrac{\partial U}{\partial z} \end{cases} \tag{2.47}$$

At equilibrium, the velocity components with respect to the rotating frame must vanish, so that $v_x = v_y = v_z = 0$. Consequently, the equilibrium condition reduces to requiring that the partial derivatives of the scalar pseudo-potential function U are equal to zero. Substituting Eq. (2.45) into the last three equations of Eq. (2.47) gives:

$$\begin{cases} 0 = x - \dfrac{1-\mu}{r_{13}^3}(x+\mu) - \dfrac{\mu}{r_{23}^3}(x+\mu-1) & \text{(2.48a)} \\ 0 = y - \dfrac{1-\mu}{r_{13}^3}y - \dfrac{\mu}{r_{23}^3}y & \text{(2.48b)} \\ 0 = -\dfrac{1-\mu}{r_{13}^3}z - \dfrac{\mu}{r_{23}^3}z & \text{(2.48c)} \end{cases}$$

From Eq. (2.48c), it is apparent that the Lagrange points lie on the $\hat{x}$-$\hat{y}$ plane, as $z = 0$ must be satisfied. Moreover, Eq. (2.48b) can be rewritten by collecting y as:

$$y\left(1 - \frac{1-\mu}{r_{13}^3} - \frac{\mu}{r_{23}^3}\right) = 0 \tag{2.49}$$

It follows that the equilibrium solutions can be classified into two distinct families: those with $y = 0$ and those with $y \neq 0$.

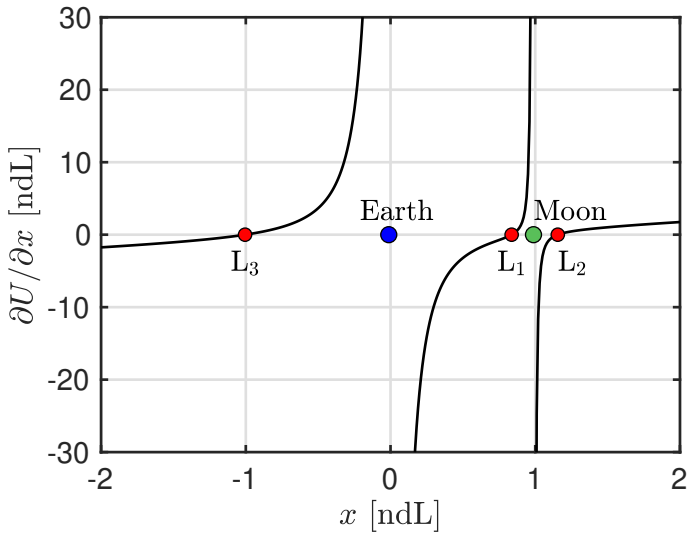
Three equilibrium points L_1, L_2 and L_3, known as collinear Lagrange points, can be found by imposing $y = 0$ (e.g., [63]). With this choice, Eq. (2.48b) is identically satisfied, and the coordinates of the equilibrium points along the $\hat{x}$-axis are obtained from Eq. (2.48a), by imposing $y = z = 0$ and solving the resulting expression:

$$x - (1-\mu)\frac{x+\mu}{|x+\mu|^3} - \mu\frac{x+\mu-1}{|x+\mu-1|^3} = 0 \tag{2.50}$$

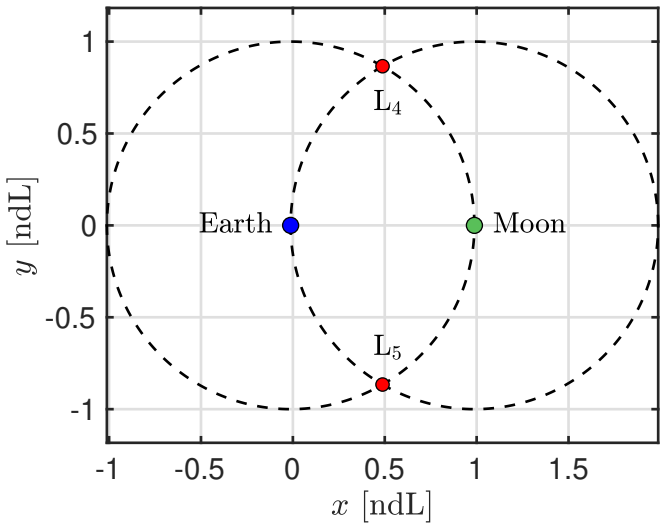
The remaining two equilibrium points L_4 and L_5, known as triangular or equilateral Lagrange points, correspond instead to the case $y \neq 0$ (e.g., [64]). These points are located at the intersection of two circles of radius $r_{13} = r_{23} = 1$ centred at the two primaries P_1 and P_2. Under this condition, Eqs. (2.48a) and (2.48b) are both satisfied, and the position of the equilibrium points can be found analytically by solving:

$$\begin{cases} (x+\mu)^2 + y^2 = 1 \\ (x+\mu-1)^2 + y^2 = 1 \end{cases} \tag{2.51}$$

Figure 2.3a shows the collinear Lagrange points on the $\hat{x}$-axis of the Earth–Moon Barycentric (EMB) rotating frame, while Fig. 2.3b shows the triangular Lagrange points in the corresponding $\hat{x}$-$\hat{y}$ plane. Coordinates are expressed in nondimensional length units, ndL.



(a) Collinear Lagrange points.



(b) Triangular Lagrange points.

Figure 2.3: Collinear and triangular Lagrange points.

2.2.5. Integral of the motion

In the rotating frame, the CR3BP is an autonomous Hamiltonian system. As a result, it admits an integral of motion known as the JC [60, 61]. This quantity can be obtained directly by manipulating the corresponding equations of motion. In particular, multiplying the three second-order differential equations in Eq. (2.46) by $\dot{x}$, $\dot{y}$ and $\dot{z}$, respectively, and then summing them yields:

$$\dot{x}\ddot{x} + \dot{y}\ddot{y} + \dot{z}\ddot{z} = \dot{x}\frac{\partial U}{\partial x} + \dot{y}\frac{\partial U}{\partial y} + \dot{z}\frac{\partial U}{\partial z} \tag{2.52}$$

The right-hand side of Eq. (2.52) corresponds to the total time derivative of the scalar pseudo-potential U, which can be written as:

$$\frac{dU}{dt} = \dot{x}\frac{\partial U}{\partial x} + \dot{y}\frac{\partial U}{\partial y} + \dot{z}\frac{\partial U}{\partial z} \tag{2.53}$$

Substituting this expression into Eq. (2.52) and integrating with respect to time gives:

$$\dot{x}^2 + \dot{y}^2 + \dot{z}^2 = 2U - JC \tag{2.54}$$

where JC denotes the constant of integration. Introducing the squared norm of the velocity vector in the rotating frame, $v^2 = \dot{x}^2 + \dot{y}^2 + \dot{z}^2$, Eq. (2.54) can be rewritten as:

$$v^2 = 2U - JC \tag{2.55}$$

The JC can also be related to the energy integral E of the system through:

$$JC = -2E \tag{2.56}$$

Therefore, higher values of the energy integral correspond to lower values of the JC.

2.2.6. Zero Velocity Surfaces

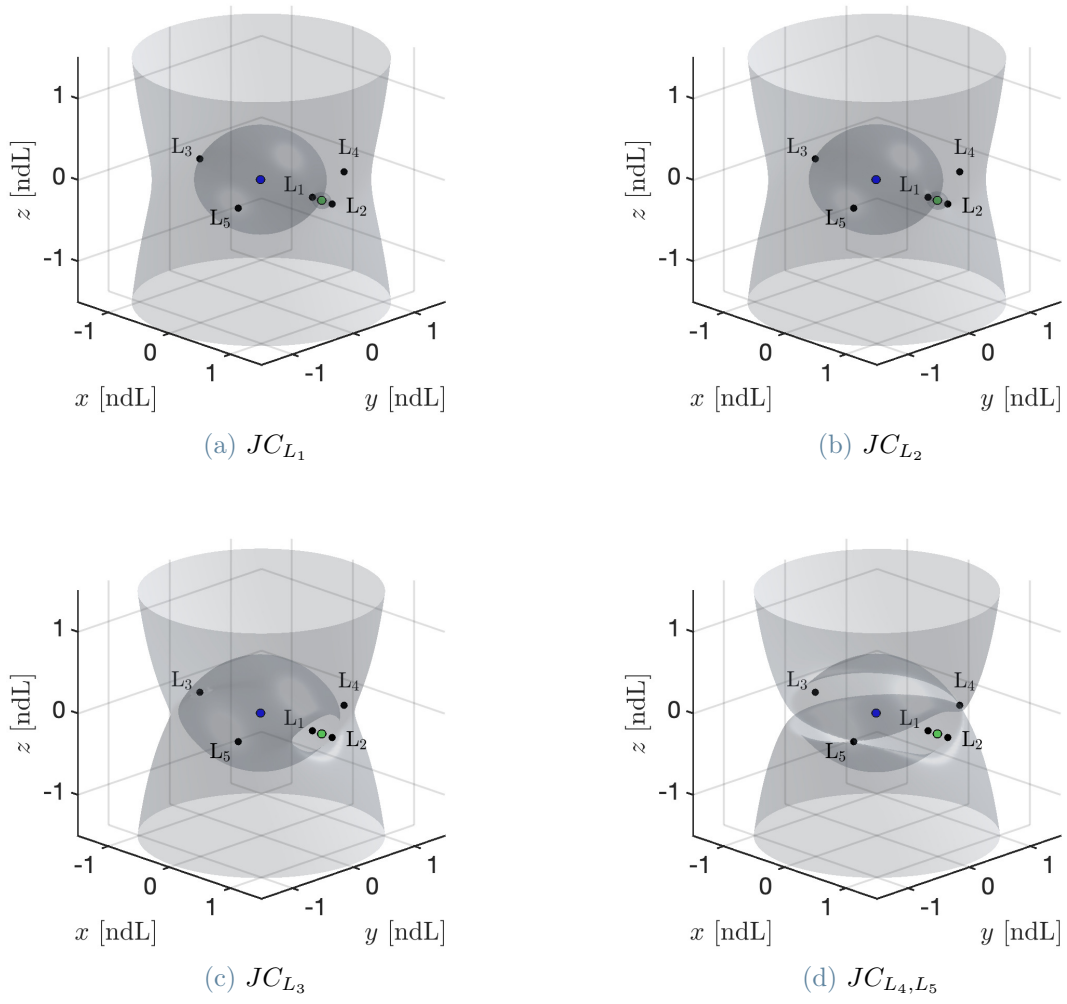
The expression of the JC provides key insight into the dynamical structure of the CR3BP from an energy perspective. Since the squared norm of the velocity vector in the rotating frame must be non-negative, the condition $v^2 \geq 0$ must be satisfied. Therefore, enforcing this constraint on Eq. (2.55) yields:

$$U(x, y, z) \geq \frac{JC}{2} \tag{2.57}$$

This relation defines a fundamental constraint on the motion in the CR3BP, and all points that violate Eq. (2.57) define a dynamically *forbidden* region. For a given value of JC, the set of points (x, y, z) satisfying the equality:

$$U(x, y, z) = \frac{JC}{2} \tag{2.58}$$

defines the Zero Velocity Surfaces (ZVSs), which represent a boundary between the *admissible* and *forbidden* regions of motion [61, 65]. Figure 2.4 shows the ZVSs associated with the JC values of the Lagrange points in the Earth–Moon system. Consistently with the colour code introduced in Sec. 2.2.1, the blue and the green dots represent the Earth and the Moon, respectively, while the gray surfaces represent the ZVSs.

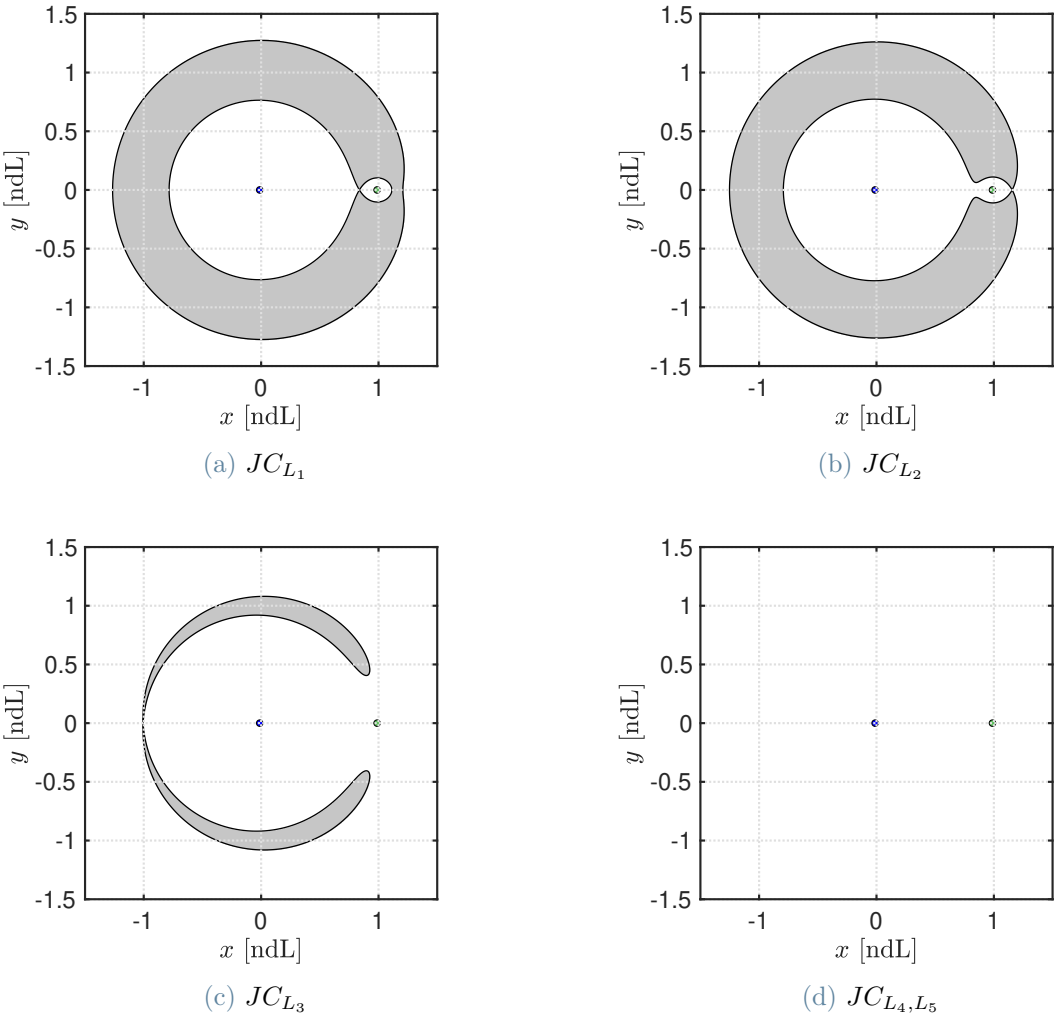


(a) JC_{L_1} (b) JC_{L_2}

(c) JC_{L_3} (d) JC_{L_4,L_5}

Figure 2.4: Zero Velocity Surfaces.

When the analysis is restricted to planar motion, the ZVSs reduce to the ZVCs, providing a convenient two-dimensional representation of the *admissible* region of motion. Figure 2.5 shows the ZVCs associated with the JC values of the Lagrange points in the Earth–Moon system. In accordance with the colour code introduced in Sec. 2.2.1, the blue and the green dots represent the Earth and the Moon, respectively, the gray areas are the *forbidden* regions, and the white areas are the *admissible* ones.



(a) JC_{L_1} (b) JC_{L_2}

(c) JC_{L_3} (d) JC_{L_4,L_5}

Figure 2.5: Zero Velocity Curves.

It can be observed that, for $JC > JC_{L_1}$, no opening exists between P_1 and P_2, and transfers between the primaries are not admitted. When $JC = JC_{L_1}$, a first opening appears in correspondence with L_1, making interior transfers between P_1 and P_2 possible. As the mechanical energy of the system increases (i.e., the JC decreases), a second neck opens at L_2 when $JC = JC_{L_2}$, thus allowing both interior and exterior transfers. By further increasing the mechanical energy, the *forbidden* regions shrink progressively, and a third opening appears at L_3 when $JC = JC_{L_3}$. Finally, when the JC of the system decreases to $JC = JC_{L_4,L_5}$, the projection of the *forbidden* region on the $\hat{x}$-$\hat{y}$ plane of the rotating frame disappears, so that a particle is no longer restricted to planar motion. However, as evident from Fig. 2.4d, in this last case a constraint in the out-of-plane direction is still present in the full three-dimensional case [65].

2.3. Fundamental variational relationships

This chapter presents the fundamental variational relationships underlying the analysis of nonlinear spacecraft dynamics. In particular, it introduces the definition of the State Transition Matrix (STM), its computation through finite-difference and variational approaches, and its main properties [61, 66]. These concepts provide the theoretical and numerical foundation for the computation of cislunar periodic orbits and their associated invariant manifolds, which are discussed in the following sections.

2.3.1. Definition of the State Transition Matrix

Consider the dynamics of a spacecraft described by the nonlinear initial value problem:

$$\begin{cases} \dot{\boldsymbol{x}} = \boldsymbol{f}(\boldsymbol{x}, t) \\ \boldsymbol{x}(t_0) = \boldsymbol{x}_0 \end{cases} \tag{2.59}$$

where $\boldsymbol{x}(t) \in \mathbb{R}^n$ is the state vector at time t, $\boldsymbol{f} : \mathbb{R}^n \times \mathbb{R} \to \mathbb{R}^n$ is the vector field governing the dynamics, and $\boldsymbol{x}_0 \in \mathbb{R}^n$ is the initial state vector at the initial epoch t_0.

The solution of the system can be expressed through the flow map as:

$$\boldsymbol{x}(t) = \varphi(t, \boldsymbol{x}_0) \tag{2.60}$$

where $\varphi(t, \boldsymbol{x}_0)$ denotes the state reached at time t by the trajectory originating from $\boldsymbol{x}_0$ at time t_0. In general, the flow is not available in closed form, and the corresponding solution must therefore be obtained by numerically integrating the equations of motion.

Consider now a perturbation $\delta\boldsymbol{x}_0$ applied to the nominal initial condition $\boldsymbol{x}_0$. The corresponding perturbed solution can be written as:

$$\boldsymbol{x}(t) + \delta\boldsymbol{x}(t) = \varphi(t, \boldsymbol{x}_0 + \delta\boldsymbol{x}_0) \tag{2.61}$$

where $\delta\boldsymbol{x}(t)$ denotes the deviation of the perturbed trajectory from the nominal one at time t. In general, evaluating this expression for different initial perturbations $\delta\boldsymbol{x}_0$ would require multiple numerical integrations of the full nonlinear system, which may become computationally expensive. However, if the perturbed trajectory remains sufficiently close to the nominal one, the flow can be linearised with respect to the initial condition by performing a first-order Taylor expansion about $\boldsymbol{x}_0$. Under this assumption, one obtains:

$$\varphi(t, \boldsymbol{x}_0 + \delta\boldsymbol{x}_0) \simeq \varphi(t, \boldsymbol{x}_0) + \frac{\partial\varphi}{\partial\boldsymbol{x}_0}(t, \boldsymbol{x}_0)\delta\boldsymbol{x}_0 \tag{2.62}$$

where $\partial\varphi/\partial\boldsymbol{x}_0 \in \mathbb{R}^{n\times n}$ denotes the Jacobian of the flow with respect to the initial state, evaluated along the nominal trajectory.

Substituting the previous expression into Eq. (2.61) yields:

$$\boldsymbol{x}(t) + \delta\boldsymbol{x}(t) = \varphi(t, \boldsymbol{x}_0) + \frac{\partial\varphi}{\partial\boldsymbol{x}_0}(t, \boldsymbol{x}_0)\delta\boldsymbol{x}_0 \tag{2.63}$$

Recalling that $\boldsymbol{x}(t) = \varphi(t, \boldsymbol{x}_0)$, the common terms in Eq. (2.63) cancel out, giving:

$$\delta\boldsymbol{x}(t) = \frac{\partial\varphi}{\partial\boldsymbol{x}_0}(t, \boldsymbol{x}_0)\delta\boldsymbol{x}_0 \tag{2.64}$$

The matrix:

$$\Phi(t, t_0) = \frac{\partial\varphi}{\partial\boldsymbol{x}_0}(t, \boldsymbol{x}_0) \tag{2.65}$$

is referred to as the STM. The STM provides a first-order mapping between an infinitesimal perturbation in the initial state and the corresponding perturbation at time t [66]. Accordingly, Eq. (2.64) can be rewritten in compact form as:

$$\delta\boldsymbol{x}(t) = \Phi(t, t_0)\delta\boldsymbol{x}_0 \tag{2.66}$$

The validity of this linear approximation is limited to perturbations that remain sufficiently small over the time interval of interest. Consequently, the model may lose accuracy in the presence of large initial displacements, long propagation times, or highly nonlinear dynamics. Finally, by definition, the STM satisfies the initial condition:

$$\Phi(t_0, t_0) = \mathbf{I} \tag{2.67}$$

that is, at the initial epoch t_0, the state perturbation $\delta\boldsymbol{x}_0$ is mapped onto itself.

2.3.2. Computation of the STM: finite differences

A first approach for computing the STM consists of approximating the Jacobian of the flow by finite differences [67]. In orbital dynamics, the state vector can be written as:

$$\boldsymbol{x} = (x, y, z, v_x, v_y, v_z)^\top \tag{2.68}$$

Since the flow map in Eq. (2.60) is a vector-valued function, it follows that:

$$\begin{cases} x(t) = \varphi_x(t, \boldsymbol{x}_0) \\ y(t) = \varphi_y(t, \boldsymbol{x}_0) \\ \quad \vdots \\ v_z(t) = \varphi_{v_z}(t, \boldsymbol{x}_0) \end{cases} \tag{2.69}$$

As a consequence, the STM can be written explicitly in matrix form as:

$$\Phi(t, t_0) = \frac{\partial \varphi}{\partial \boldsymbol{x}_0}(t, \boldsymbol{x}_0) = \begin{bmatrix} \dfrac{\partial \varphi_x}{\partial x_0} & \dfrac{\partial \varphi_x}{\partial y_0} & \cdots & \dfrac{\partial \varphi_x}{\partial v_{z_0}} \\ \dfrac{\partial \varphi_y}{\partial x_0} & \dfrac{\partial \varphi_y}{\partial y_0} & \cdots & \dfrac{\partial \varphi_y}{\partial v_{z_0}} \\ \vdots & \vdots & \ddots & \vdots \\ \dfrac{\partial \varphi_{v_z}}{\partial x_0} & \dfrac{\partial \varphi_{v_z}}{\partial y_0} & \cdots & \dfrac{\partial \varphi_{v_z}}{\partial v_{z_0}} \end{bmatrix} \tag{2.70}$$

Each column of the STM can be approximated using forward finite differences as:

$$\frac{\partial \varphi}{\partial x_{0,j}} \simeq \frac{\varphi(t, \boldsymbol{x}_0 + \boldsymbol{\varepsilon}_j) - \varphi(t, \boldsymbol{x}_0)}{\varepsilon_j}, \qquad j = 1, \ldots, 6 \tag{2.71}$$

where the perturbation $\boldsymbol{\varepsilon}_j$ associated with the j-th column is defined as:

$$\boldsymbol{\varepsilon}_j = (0, \ldots, \varepsilon_j, \ldots, 0), \qquad j = 1, \ldots, 6 \tag{2.72}$$

A suitable choice for ε_j, based on the machine precision `eps`, is:

$$\varepsilon_j = \begin{cases} \sqrt{\texttt{eps}} & \text{if } |x_{0,j}| < 1 \\ |x_{0,j}| \sqrt{\texttt{eps}} & \text{if } |x_{0,j}| \geq 1 \end{cases} \tag{2.73}$$

The computation of the STM requires seven numerical propagations: one nominal propagation, corresponding to $\varphi(t, \boldsymbol{x}_0)$, and six perturbed propagations, corresponding to $\varphi(t, \boldsymbol{x}_0 + \boldsymbol{\varepsilon}_j)$, for $j = 1, \ldots, 6$. Since $\dot{\boldsymbol{x}} = \boldsymbol{f}(\boldsymbol{x}, t)$ is a system of six scalar first-order ordinary differential equations (ODEs), the overall computational cost corresponds to the integration of 42 scalar ODEs.

2.3.3. Computation of the STM: variational approach

The variational approach computes the STM by linearising the equations of motion about a nominal trajectory and integrating the resulting variational equations together with the reference state [67]. Unlike the finite-difference method, which approximates the STM through multiple propagations of perturbed trajectories, this formulation determines it directly from its associated matrix differential equation derived below.

Let $\boldsymbol{x}^*(t)$ denote the nominal solution of the nonlinear initial value problem in Eq. (2.59). Consider now a neighbouring trajectory $\boldsymbol{x}(t)$ that remains sufficiently close to $\boldsymbol{x}^*(t)$, and define the corresponding state deviation as:

$$\delta\boldsymbol{x}(t) = \boldsymbol{x}(t) - \boldsymbol{x}^*(t) \tag{2.74}$$

The aim is to derive a linear differential equation governing the evolution of $\delta\boldsymbol{x}(t)$, and then use it to determine the governing equation for the STM. To this end, consider the first-order expansion of the vector field $\boldsymbol{f}(\boldsymbol{x}, t)$ about the reference trajectory $\boldsymbol{x}^*(t)$:

$$\dot{\boldsymbol{x}}(t) = \boldsymbol{f}(\boldsymbol{x}, t) \simeq \boldsymbol{f}(\boldsymbol{x}^*, t) + \left.\frac{\partial \boldsymbol{f}}{\partial \boldsymbol{x}}\right|_{\boldsymbol{x}=\boldsymbol{x}^*(t)} (\boldsymbol{x}(t) - \boldsymbol{x}^*(t)) \tag{2.75}$$

For notational compactness, let us introduce the time-varying Jacobian matrix:

$$A(t) = \left.\frac{\partial \boldsymbol{f}}{\partial \boldsymbol{x}}\right|_{\boldsymbol{x}=\boldsymbol{x}^*(t)} \tag{2.76}$$

Moreover, recalling the definition of state deviation introduced in Eq. (2.74), the perturbed state $\boldsymbol{x}(t)$ and its time derivative $\dot{\boldsymbol{x}}(t)$ can be written as:

$$\begin{aligned} \boldsymbol{x}(t) &= \boldsymbol{x}^*(t) + \delta\boldsymbol{x}(t) \\ \dot{\boldsymbol{x}}(t) &= \dot{\boldsymbol{x}}^*(t) + \delta\dot{\boldsymbol{x}}(t) \end{aligned} \tag{2.77}$$

Substituting Eqs. (2.74), (2.76) and (2.77) into Eq. (2.75) yields:

$$\dot{\boldsymbol{x}}^*(t) + \delta\dot{\boldsymbol{x}}(t) \simeq \boldsymbol{f}(\boldsymbol{x}^*, t) + A(t)\delta\boldsymbol{x}(t) \tag{2.78}$$

Since the nominal trajectory satisfies the original nonlinear equations of motion, that is $\dot{\boldsymbol{x}}^*(t) = \boldsymbol{f}(\boldsymbol{x}^*, t)$, the common terms cancel out and the following expression is obtained:

$$\delta\dot{\boldsymbol{x}}(t) = A(t)\delta\boldsymbol{x}(t) \tag{2.79}$$

This is a linear time-varying system that governs the first-order evolution of an infinitesimal perturbation $\delta\boldsymbol{x}(t)$ along the nominal trajectory $\boldsymbol{x}^*(t)$.

Recall that the general solution of Eq. (2.79) can be expressed in terms of the STM as:

$$\delta\boldsymbol{x}(t) = \Phi(t, t_0)\delta\boldsymbol{x}_0 \tag{2.80}$$

In order to derive the matrix differential equation governing the evolution of the STM, differentiate the previous expression with respect to time:

$$\delta\dot{\boldsymbol{x}}(t) = \dot{\Phi}(t, t_0)\delta\boldsymbol{x}_0 \tag{2.81}$$

Substituting Eqs. (2.80) and (2.81) into Eq. (2.79) yields:

$$\dot{\Phi}(t, t_0)\delta\boldsymbol{x}_0 = A(t)\Phi(t, t_0)\delta\boldsymbol{x}_0 \tag{2.82}$$

Since this relation must hold for any initial perturbation $\delta\boldsymbol{x}_0$, it follows that the STM satisfies the matrix differential equation:

$$\dot{\Phi}(t, t_0) = A(t)\Phi(t, t_0) \tag{2.83}$$

which can be integrated starting from the initial condition:

$$\Phi(t_0, t_0) = \mathbf{I} \tag{2.84}$$

Observe that the initial value problem defined by Eqs. (2.83) and (2.84) consists of 36 scalar first-order ODEs, corresponding to the entries of the STM. However, integrating this system also requires the reference trajectory $\boldsymbol{x}^*(t)$, since the matrix $A(t)$ must be evaluated along the nominal solution. Consequently, the complete variational system to be integrated for the computation of the STM is:

$$\begin{cases} \dot{\boldsymbol{x}} = \boldsymbol{f}(\boldsymbol{x}, t) \\ \dot{\Phi}(t, t_0) = A(t)\Phi(t, t_0) \end{cases} \quad \text{with ICs:} \quad \begin{cases} \boldsymbol{x}(t_0) = \boldsymbol{x}_0 \\ \Phi(t_0, t_0) = \mathbf{I} \end{cases} \tag{2.85}$$

The reference trajectory and the STM are propagated simultaneously: the first 6 scalar ODEs describe the evolution of the nominal state, which is used to evaluate $A(t)$, while the remaining 36 scalar ODEs govern the evolution of the STM. Therefore, as in the finite-difference approach, the overall computational cost corresponds to the integration of 42 scalar first-order ODEs.

2.4. Numerical computation of periodic orbits

This section introduces the numerical procedure adopted to compute the periodic Halo orbits considered in this work. First, the main properties of the Earth–Moon L_2 Halo family are recalled, with particular attention to the southern branch and to NRHOs. Then, the differential correction algorithm used to obtain a single periodic solution is described. Finally, the numerical continuation method employed to generate the corresponding family of periodic orbits is presented.

2.4.1. Family of Halo orbits

Periodic orbits are trajectories that repeat the same state after a finite time interval, referred to as the orbital period T [60]. In the CR3BP, several families of periodic orbits can be identified in the rotating frame [68, 69]. In general, these orbits evolve either around one of the five Lagrange points or around one of the two primaries, providing fundamental dynamical structures for cislunar mission design [70].

Among the periodic orbits associated with the collinear Lagrange points, Halo orbits represent one of the most relevant three-dimensional classes [71]. They bifurcate from the planar Lyapunov families and exhibit an out-of-plane motion around the corresponding libration point [72, 73]. Due to the symmetry of the CR3BP with respect to the $\hat{x}$-$\hat{y}$ plane, each Halo family consists of two mirrored branches: a northern branch, characterised by positive out-of-plane motion, and a southern branch, characterised by negative out-of-plane motion [61].

In this work, the southern branch of the Earth–Moon L_2 Halo family is considered, with particular attention to the NRHOs [74]. These orbits are especially attractive for cislunar operations because of their favourable stability properties, accessibility from Earth, access to the lunar surface and to interplanetary destinations, and communication coverage of lunar south-polar regions [75–78]. In particular, a southern Earth–Moon L_2 NRHO in a 9:2 synodic resonance was considered in the original Lunar Gateway mission design as the baseline orbit for a long-term cislunar outpost around the Moon [79].

Halo orbits are not available as closed-form solutions of the CR3BP. Although analytical approximations can provide suitable initial guesses, numerical procedures are required to compute them accurately [61, 73, 80]. The following sections introduce the differential correction scheme used to obtain a single periodic Halo orbit, and the numerical continuation method employed to generate the complete family.

2.4.2. Differential correction

The solutions of the three-dimensional CR3BP satisfy the symmetry:

$$\mathcal{S} : (x, y, z, v_x, v_y, v_z, t) \rightarrow (x, -y, z, -v_x, v_y, -v_z, -t) \tag{2.86}$$

This symmetry can be exploited to compute cislunar periodic orbits. In particular, for Halo orbits, the trajectory is required to intersect the $\hat{x}$-$\hat{z}$ symmetry plane orthogonally at two consecutive crossings, separated by half of the orbital period. Let us consider an initial state $\boldsymbol{x}_0$ satisfying the orthogonal crossing condition:

$$\boldsymbol{x}_0 = (x_0, 0, z_0, 0, v_{y0}, 0)^\top \tag{2.87}$$

By propagating $\boldsymbol{x}_0$ up to an initial guess of the half-period t, corresponding approximately to the next crossing of the $\hat{x}$-$\hat{z}$ plane, one obtains:

$$\boldsymbol{x}(t) = \varphi(t, \boldsymbol{x}_0) = (x, y, z, v_x, v_y, v_z)^\top \tag{2.88}$$

The differential correction algorithm is then used to determine a periodic Halo orbit by iteratively computing a correction $\Delta\boldsymbol{x}_0$ to the initial state:

$$\Delta\boldsymbol{x}_0 = (\Delta x_0, 0, \Delta z_0, 0, \Delta v_{y0}, 0)^\top \tag{2.89}$$

and a correction Δt to the propagation time, such that the corrected trajectory intersects the $\hat{x}$-$\hat{z}$ plane orthogonally at the next crossing. The desired terminal state is therefore:

$$\tilde{\boldsymbol{x}} = \varphi(t + \Delta t, \boldsymbol{x}_0 + \Delta\boldsymbol{x}_0) = (\tilde{x}, 0, \tilde{z}, 0, \tilde{v}_y, 0)^\top \tag{2.90}$$

To compute these corrections, consider the first-order Taylor expansion of the flow with respect to both the initial state and the propagation time, evaluated about $(t, \boldsymbol{x}_0)$:

$$\varphi(t + \Delta t, \boldsymbol{x}_0 + \Delta\boldsymbol{x}_0) \simeq \varphi(t, \boldsymbol{x}_0) + \frac{\partial\varphi}{\partial\boldsymbol{x}_0}(t, \boldsymbol{x}_0)\Delta\boldsymbol{x}_0 + \frac{\partial\varphi}{\partial t}(t, \boldsymbol{x}_0)\Delta t \tag{2.91}$$

Recalling the definition of the STM introduced in Eq. (2.65), and observing that:

$$\frac{\partial\varphi}{\partial t}(t, \boldsymbol{x}_0) = \dot{\boldsymbol{x}}(t) = \boldsymbol{f}(\boldsymbol{x}(t), t) \tag{2.92}$$

Equation (2.91) can be rearranged as:

$$\Phi(t, t_0)\Delta\boldsymbol{x}_0 + \boldsymbol{f}(\boldsymbol{x}(t), t)\Delta t = \varphi(t + \Delta t, \boldsymbol{x}_0 + \Delta\boldsymbol{x}_0) - \varphi(t, \boldsymbol{x}_0) \tag{2.93}$$

By substituting the component expressions of the vectors introduced in Eqs. (2.88), (2.89), and (2.90), Eq. (2.93) can be written in expanded matrix form as:

$$\begin{bmatrix} \Phi_{11} & \Phi_{12} & \Phi_{13} & \Phi_{14} & \Phi_{15} & \Phi_{16} & f_1(t) \\ \Phi_{21} & \Phi_{22} & \Phi_{23} & \Phi_{24} & \Phi_{25} & \Phi_{26} & f_2(t) \\ \Phi_{31} & \Phi_{32} & \Phi_{33} & \Phi_{34} & \Phi_{35} & \Phi_{36} & f_3(t) \\ \Phi_{41} & \Phi_{42} & \Phi_{43} & \Phi_{44} & \Phi_{45} & \Phi_{46} & f_4(t) \\ \Phi_{51} & \Phi_{52} & \Phi_{53} & \Phi_{54} & \Phi_{55} & \Phi_{56} & f_5(t) \\ \Phi_{61} & \Phi_{62} & \Phi_{63} & \Phi_{64} & \Phi_{65} & \Phi_{66} & f_6(t) \end{bmatrix} \begin{pmatrix} \Delta x_0 \\ 0 \\ \Delta z_0 \\ 0 \\ \Delta v_{y0} \\ 0 \\ \Delta t \end{pmatrix} = \begin{pmatrix} \tilde{x} - x(t) \\ 0 - y(t) \\ \tilde{z} - z(t) \\ 0 - v_x(t) \\ \tilde{v}_y - v_y(t) \\ 0 - v_z(t) \end{pmatrix} \tag{2.94}$$

Only the second, fourth and sixth rows are required to enforce the orthogonal crossing of the $\hat{x}$-$\hat{z}$ plane, namely $y(t) = 0$, $v_x(t) = 0$, and $v_z(t) = 0$. This gives the reduced system:

$$\begin{bmatrix} \Phi_{21} & \Phi_{23} & \Phi_{25} & f_2(t) \\ \Phi_{41} & \Phi_{43} & \Phi_{45} & f_4(t) \\ \Phi_{61} & \Phi_{63} & \Phi_{65} & f_6(t) \end{bmatrix} \begin{pmatrix} \Delta x_0 \\ \Delta z_0 \\ \Delta v_{y0} \\ \Delta t \end{pmatrix} = \begin{pmatrix} -y(t) \\ -v_x(t) \\ -v_z(t) \end{pmatrix} \tag{2.95}$$

This linear system is underdetermined and therefore admits infinitely many solutions. However, the remaining degree of freedom can be used to prescribe one component of the initial state, thus controlling the characteristics of the resulting Halo orbit. For example, by fixing the initial x-coordinate, Eq. (2.95) reduces to:

$$\begin{bmatrix} \Phi_{23} & \Phi_{25} & f_2(t) \\ \Phi_{43} & \Phi_{45} & f_4(t) \\ \Phi_{63} & \Phi_{65} & f_6(t) \end{bmatrix} \begin{pmatrix} \Delta z_0 \\ \Delta v_{y0} \\ \Delta t \end{pmatrix} = \begin{pmatrix} -y(t) \\ -v_x(t) \\ -v_z(t) \end{pmatrix} \tag{2.96}$$

The solution of this linear system yields the corrections $\Delta\boldsymbol{x}_0$ and Δt applied to the current guess of the initial state and propagation time. The procedure is repeated by updating:

$$\begin{aligned} \boldsymbol{x}_0^{(i+1)} &= \boldsymbol{x}_0^{(i)} + \Delta\boldsymbol{x}_0^{(i)} \\ t^{(i+1)} &= t^{(i)} + \Delta t^{(i)} \end{aligned} \tag{2.97}$$

until the terminal constraints:

$$y(t) = 0, \qquad v_x(t) = 0, \qquad v_z(t) = 0 \tag{2.98}$$

are satisfied within a prescribed tolerance.

2.4.3. Numerical continuation

A numerical continuation method is adopted to generate the family of periodic Halo orbits from a known periodic solution. Since the differential correction scheme is locally convergent, each corrected solution can be used to initialise the computation of a neighbouring orbit. In this work, a Natural Parameter Continuation Method (NPCM) is employed by choosing the initial x-coordinate of the orbit as the continuation parameter [81]. An equivalent formulation could be obtained by prescribing the initial z-coordinate.

At the k-th continuation step, x_0 is fixed to the prescribed value $x_0^{(k)}$, while the remaining free variables are corrected until the periodicity constraints imposed by the differential correction algorithm are satisfied. The converged solution is then used as the initial guess for the next orbit, obtained by updating the continuation parameter as:

$$x_0^{(k+1)} = x_0^{(k)} + \delta x_0. \tag{2.99}$$

Figure 2.6 shows the corresponding family of southern Earth–Moon L_2 Halo orbits with a colormap based on the continuation parameter x_0, expressed in ndL.

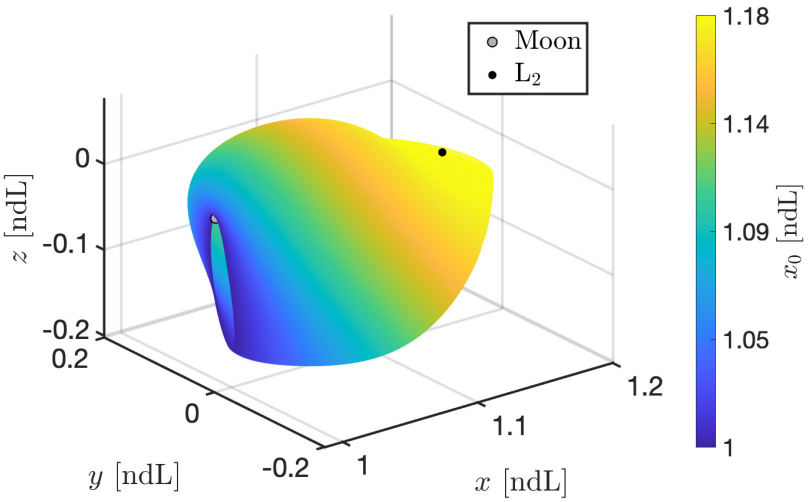


Figure 2.6: Family of southern Earth–Moon L_2 Halo orbits.

2.5. Invariant manifolds

The invariant manifolds associated with LPOs are among the most important phase-space structures governing transport mechanisms in the CR3BP. They organise the flow in the neighbourhood of a periodic orbit by identifying the natural dynamical channels through which trajectories can approach, depart from, or transit between different regions of the phase space [61, 82]. Given an unstable periodic orbit Γ, its stable manifold $W^s(\Gamma)$ is the set of trajectories that asymptotically approach Γ in forward time, whereas its unstable manifold $W^u(\Gamma)$ is the set of trajectories that asymptotically depart from Γ in forward time. For this reason, the invariant manifolds have been extensively exploited in low-energy trajectory design for cislunar space missions [70].

In the present work, the focus is placed on the unstable invariant manifolds associated with periodic Halo orbits. This choice is motivated by their role in describing the natural departure structures from the reference LPOs, which makes them particularly relevant for end-of-life analyses [51, 52, 83]. Moreover, they provide a meaningful framework for the analysis of fragmentation events, since debris generated in the neighbourhood of a reference Halo orbit may acquire components along the unstable directions and be rapidly transported away from the reference trajectory.

The numerical computation of the unstable invariant manifold starts from a periodic Halo orbit Γ, obtained through the differential correction algorithm described in Sec. 2.4.2. Let $\boldsymbol{x}_\Gamma(t)$ be the corresponding periodic solution with period T, such that:

$$\boldsymbol{x}_\Gamma(t+T) = \boldsymbol{x}_\Gamma(t) \tag{2.100}$$

The linearised dynamics along the periodic orbit is described by the STM $\Phi(t, t_0)$, which satisfies the variational system:

$$\begin{cases} \dot{\Phi}(t, t_0) = A(t)\Phi(t, t_0) \\ \Phi(t_0, t_0) = \mathbf{I} \end{cases} \tag{2.101}$$

where:

$$A(t) = \left.\frac{\partial \boldsymbol{f}}{\partial \boldsymbol{x}}\right|_{\boldsymbol{x}=\boldsymbol{x}_\Gamma(t)} \tag{2.102}$$

is the Jacobian matrix of the CR3BP vector field evaluated along the periodic solution.

The monodromy matrix $\mathbf{M}$ is defined as the STM evaluated after one orbital period:

$$\mathbf{M} = \Phi(t_0 + T, t_0) \tag{2.103}$$

According to Floquet theory, the eigendecomposition of the monodromy matrix provides a local linear description of the dynamics in the neighbourhood of the periodic orbit [61]. The eigenvalues of $\mathbf{M}$, also referred to as Floquet or characteristic multipliers, can therefore be used to study the linear stability properties of the orbit.

Before computing the unstable manifold, some relevant properties of the eigenvalues of $\mathbf{M}$ should be recalled [61]. Since the CR3BP is an autonomous Hamiltonian system, the monodromy matrix associated with a periodic orbit admits a trivial eigenvalue $+1$ with algebraic multiplicity of at least two. One unit multiplier is associated with the tangent direction to the periodic motion, reflecting the invariance of the autonomous flow under a shift of the initial time. The second one follows from the Hamiltonian structure of the system and from the conservation of the JC.

Moreover, it can be demonstrated that the monodromy matrix of an autonomous Hamiltonian system is symplectic, namely:

$$\mathbf{M}^T \mathbf{J} \mathbf{M} = \mathbf{J} \tag{2.104}$$

with:

$$\mathbf{J} = \begin{bmatrix} \mathbf{0}_{3\times3} & \mathbf{I}_{3\times3} \\ -\mathbf{I}_{3\times3} & \mathbf{0}_{3\times3} \end{bmatrix} \tag{2.105}$$

As a consequence of the symplectic structure, the eigenvalues of $\mathbf{M}$ occur in reciprocal pairs. Thus, if λ is an eigenvalue, then also $1/\lambda$ is an eigenvalue. Moreover, since the characteristic polynomial of $\mathbf{M}$ has real coefficients, its complex eigenvalues occur in conjugate pairs. Hence, if λ is a complex eigenvalue, then $\bar{\lambda}$ is also an eigenvalue.

Assume now that a pair of real eigenvalues λ^s and λ^u exists off the unit circle. From the properties of the monodromy matrix described above, it follows that:

$$|\lambda^s| < 1, \qquad |\lambda^u| > 1, \qquad \lambda^s = \frac{1}{\lambda^u} \tag{2.106}$$

The eigenvector $\boldsymbol{w}^u(t_0)$ associated with λ^u defines, at first order, the local unstable direction at the initial point of the periodic orbit. The unstable direction at a generic point of the orbit is then obtained by mapping this eigenvector through the STM:

$$\boldsymbol{w}^u(t) = \Phi(t, t_0)\boldsymbol{w}^u(t_0) \tag{2.107}$$

Equivalently, introducing the phase angle θ along the periodic orbit:

$$\theta = \frac{2\pi(t - t_0)}{T} \tag{2.108}$$

the unstable direction can be reparameterised as:

$$\boldsymbol{w}^u(\theta) = \Phi(t, t_0)\boldsymbol{w}^u(0) \tag{2.109}$$

Since only the direction of the eigenvector is relevant, it is normalised as:

$$\hat{\boldsymbol{w}}^u(\theta) = \frac{\boldsymbol{w}^u(\theta)}{||\boldsymbol{w}^u(\theta)||} \tag{2.110}$$

A local approximation of the initial conditions on the unstable manifold is then obtained by perturbing the orbital states $\boldsymbol{x}(\theta)$ in the corresponding normalised unstable direction:

$$\boldsymbol{x}_0^u(\theta) = \boldsymbol{x}(\theta) \pm \varepsilon\hat{\boldsymbol{w}}^u(\theta) \tag{2.111}$$

The perturbation ε must be chosen small enough for the linear approximation of the manifold direction to remain valid, but large enough to allow the trajectory to depart naturally from the periodic orbit within a reasonable propagation time. In the Sun–Earth system, this value is typically selected to generate an initial position displacement of 200 km [83]. After rescaling to the Earth–Moon system, this corresponds to a displacement of approximately 250 m, which gives a nondimensional perturbation ε of order 10^{-7} [52].

Moreover, the perturbation ε may be assigned either a positive or a negative sign. This accounts for the fact that the unstable manifold is composed of two branches: one directed towards the smaller primary, referred to as the *interior* manifold, and one directed away from it, referred to as the *exterior* manifold [70]. However, since the sign of the eigenvector is arbitrary, the physical interpretation of each branch cannot be inferred a priori from the sign of ε. Therefore, both branches are first generated and propagated, and then they are classified according to their dynamical behaviour [52].

Once the perturbed initial conditions have been generated, the global unstable manifold is obtained by propagating them in forward time under the CR3BP dynamics:

$$\boldsymbol{x}^u(t; \theta) = \varphi(t, \boldsymbol{x}_0^u(\theta)), \qquad t \geq t_0 \tag{2.112}$$

For the periodic orbits of interest, the unstable invariant manifold is a two-dimensional object. In fact, it is parametrised by the phase angle θ, which identifies the departure point along the periodic orbit, and by the time of flight t along the corresponding manifold.

Stable invariant manifolds can be computed analogously by perturbing the periodic orbit along the corresponding stable eigendirection and propagating the resulting initial conditions backward in time under the nonlinear CR3BP dynamics. However, since this work focuses on natural departure mechanisms and debris dispersion from the reference Halo orbit, only unstable invariant manifolds are included in the present analysis.

Figure 2.7 shows the initial velocity directions associated with the unstable manifolds of a periodic Halo orbit characterised by $JC = 3.1066\,[-]$, $T = 14.68$ days, and $SI = 250\,[-]$. For this case, the perturbation $-\varepsilon$ generates the *exterior* manifold, shown in red, whereas the perturbation $+\varepsilon$ generates the *interior* manifold, shown in blue.

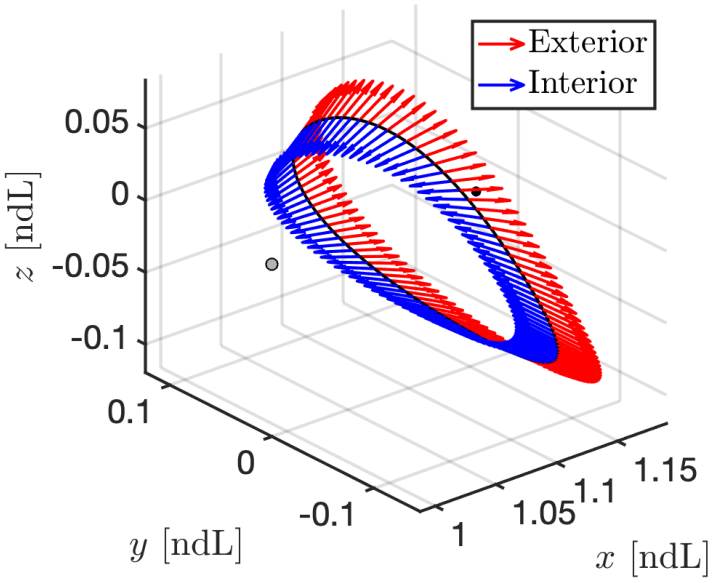


Figure 2.7: Unstable manifold directions.

Figures 2.8 and 2.9 show the global exterior branch of the unstable manifold associated with the same periodic Halo orbit. The trajectories are coloured according to the phase angle θ, which identifies the departure point of each manifold trajectory along the reference orbit. A negative perturbation of magnitude $\varepsilon = 10^{-4}$ was used to generate the manifold.

In Fig. 2.8, the unstable manifold is propagated up to $t_f = 22$ days. It is possible to observe that the trajectories wrap about themselves, forming a topological tube. Conversely, Fig. 2.9 shows the same manifold propagated up to $t_f = 60$ days. This longer propagation

time highlights the asymptotic departure of the manifold trajectories from the reference Halo orbit. Moreover, different departure rates can be observed depending on the phase angle θ at which each trajectory departs from the orbit.

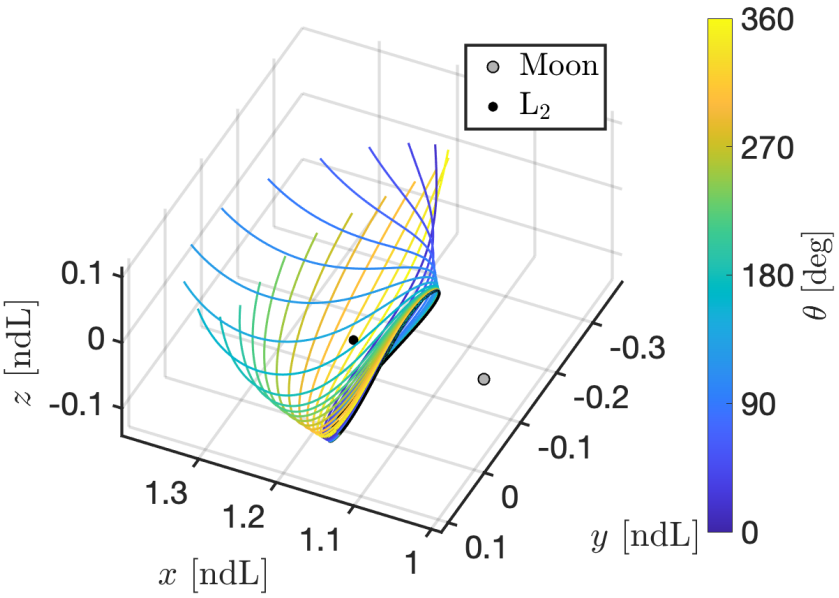


Figure 2.8: Unstable manifold trajectories ($t_f = 22$ days).

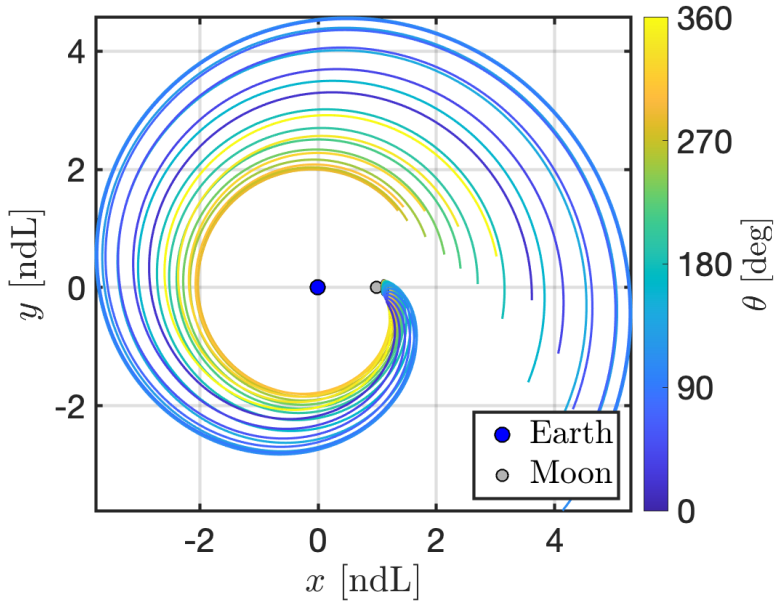


Figure 2.9: Unstable manifold trajectories ($t_f = 60$ days).

2.6. Stability and chaos indicators

This section introduces the indicators adopted in this work to characterise the dynamical behaviour of the reference periodic orbits and of the associated debris trajectories. First, the linear stability of periodic orbits is analysed through the Stability Index (SI). Then, the Cauchy-Green Strain Tensor (CGST) is introduced to describe the finite-time deformation of infinitesimal perturbations under the flow. Finally, the Finite-Time Lyapunov Exponent (FTLE) is derived and used as a local measure of trajectory chaoticity.

2.6.1. Linear stability and stability index

In orbital dynamics, stability describes the response of a trajectory to small perturbations in its initial state [84]. An orbit is considered stable when the effect of these perturbations remains bounded over time, so that nearby trajectories stay confined in the neighbourhood of the reference solution. Conversely, an unstable orbit amplifies small deviations, causing initially close trajectories to progressively depart from the nominal path.

The linear stability or instability of a periodic orbit in the CR3BP can be determined by analysing the eigenvalues of its monodromy matrix $\mathbf{M}$, defined as the STM computed after one orbital period. Recalling the properties introduced in Sec. 2.5, $\mathbf{M}$ has six eigenvalues, with one pair always equal to one. The remaining non-trivial pairs of eigenvalues can be classified as follows [50]:

- **Linear stability**: the two non-trivial eigenvalue pairs are complex conjugate and lie on the unit circle, corresponding to bounded oscillatory modes.
- **Linear instability**: at least one non-trivial pair is real and reciprocal, with one eigenvalue inside and the other outside the unit circle.
- **Complex instability**: the two non-trivial eigenvalue pairs are complex conjugate and do not lie on the unit circle, indicating the presence of bifurcations [85].

To reduce the accumulation of numerical errors, $\mathbf{M}$ is not obtained by integrating from t_0 to $t_0 + T$, but it is reconstructed from the STM evaluated over half a period, namely $\Phi(t_0 + T/2, t_0)$. Recalling the differential correction procedure introduced in Sec. 2.4.2, this matrix is already available from the correction scheme itself. Moreover, since one pair of eigenvalues is trivial, the system can be reduced so that the eigenvalues of the reduced monodromy matrix $\mathbf{M}_{red}$ correspond only to the non-trivial modes. These two simplifications are made possible by the mathematical transformations described in [73].

The resulting reduced system is:

$$\begin{bmatrix} \delta x_T \\ \delta z_T \\ \delta \dot{x}_T \\ \delta \dot{z}_T \end{bmatrix} = \mathbf{M}_{red} \begin{bmatrix} \delta x_0 \\ \delta z_0 \\ \delta \dot{x}_0 \\ \delta \dot{z}_0 \end{bmatrix} \tag{2.113}$$

Finally, the SI of a periodic orbit in the CR3BP is defined as:

$$SI = \frac{1}{2} \left| \left(\lambda_{max} + \frac{1}{\lambda_{max}} \right) \right| \tag{2.114}$$

where λ_{max} is the maximum eigenvalue of $\mathbf{M}_{red}$. For $SI < 1$, the orbit is considered linearly stable, while for $SI > 1$, the orbit is linearly unstable [73].

2.6.2. Cauchy-Green Strain Tensor

The CGST describes the relative stretching of nearby trajectories over a finite time interval, providing a local measure of the principal directions and magnitudes of expansion induced by the flow [86]. Given the STM that maps perturbations about an initial condition $\boldsymbol{x}_0$ from t_0 to t, the CGST is defined as:

$$\mathbf{C}(t, t_0) = \Phi(t, t_0)^\top \Phi(t, t_0) \tag{2.115}$$

Since the STM describes the evolution of infinitesimal perturbations about a reference trajectory, the CGST represents a natural measure of their growth or decay over the considered time interval. As $\mathbf{C}(t, t_0)$ is symmetric and positive definite, its eigendecomposition provides real positive eigenvalues λ_i and mutually orthogonal eigenvectors $\boldsymbol{\xi}_i$:

$$\mathbf{C}(t, t_0)\boldsymbol{\xi}_i = \lambda_i \boldsymbol{\xi}_i \tag{2.116}$$

The eigenvectors $\boldsymbol{\xi}_i$ identify the principal directions of deformation, while the corresponding stretching factors are given by $\sqrt{\lambda_i}$, since:

$$\|\Phi(t, t_0)\boldsymbol{\xi}_i\| = \sqrt{\lambda_i} \|\boldsymbol{\xi}_i\|. \tag{2.117}$$

In particular, the eigenvector associated with the largest eigenvalue identifies the direction of maximum stretching, whereas the eigenvector associated with the smallest eigenvalue identifies the direction of minimum stretching or maximum contraction.

2.6.3. Finite-Time Lyapunov Exponent

Lyapunov exponents are classical indicators in dynamical systems theory used to estimate the rate of divergence between initially infinitesimally close solutions. They provide a local measure of the chaoticity of a given trajectory by quantifying its sensitivity to small perturbations [87]. For a dynamical system, the number of Lyapunov exponents is equal to the dimension of the phase space, and their complete set forms the Lyapunov spectrum. Particular attention is typically given to the exponent that dominates the local expansion of the flow, namely the maximum Lyapunov exponent. For continuous dynamical systems, this quantity can be computed as:

$$\Lambda_{\max} = \lim_{t\to\infty} \frac{1}{t} \ln\left(\frac{\|\delta\boldsymbol{x}(t)\|}{\|\delta\boldsymbol{x}(t_0)\|}\right) \tag{2.118}$$

The definition of the Lyapunov exponent requires knowledge of the system evolution over an asymptotically infinite time horizon. However, in many astrodynamical applications, this limit is not readily available. Therefore, a finite-time counterpart of the classical Lyapunov exponent, known as the FTLE, is typically preferred. The largest FTLE can be derived directly from the eigendecomposition of the CGST as:

$$\text{FTLE} = \frac{1}{t^*} \ln\left(\lambda_{\max}\left(\sqrt{\mathbf{C}(t^*, t_0)}\right)\right) \tag{2.119}$$

where $\lambda_{\max}(\cdot)$ denotes the operation that extracts the largest eigenvalue of its argument, and t^* is the finite integration time over which the FTLE is evaluated [50, 86]. The value of t^* can be arbitrarily selected according to the characteristic timescale of interest.

3 | Simulation setup

This chapter defines the simulation setup adopted for the cislunar breakup analyses. First, the reference fragmentation scenario is introduced and the resulting debris population is characterised. The parent trajectories are then identified, including the selected Halo orbits and the prescribed breakup locations. Finally, the reference disposal trajectories associated with the unstable invariant manifolds are presented.

3.1. Reference breakup scenario

The debris population considered in this analysis was generated using the NASA SBM described in Sec. 2.1, assuming a spacecraft explosion as the reference scenario. This choice is motivated by the fact that the cislunar environment is still sparsely populated over a very large spatial domain, making accidental collisions less likely to occur than fragmentation events caused by explosions or internal failures. Future studies may extend the analysis to catastrophic and non-catastrophic spacecraft collisions, especially if the cislunar environment becomes increasingly populated by operational spacecraft, inactive objects and debris. However, this last scenario is precisely the condition that proper end-of-life planning for cislunar missions aims to prevent.

The lower bound of the characteristic length interval was set to $L_0 = 10\,\text{cm}$, following the indications of Johnson et al. [13] and accounting for current tracking limitations in the cislunar environment. The upper bound was set to $L_1 = 1\,\text{m}$, in accordance with the implementation recommendation discussed by Krisko [14]. A representative spacecraft mass of 800 kg was considered to enforce mass conservation, as described in Sec. 2.1.5. This value lies within the mass range indicated by Johnson et al. [13] for the applicability of the NASA SBM and it is also consistent with the values adopted by Boone et al. [39] and Guardabasso et al. [46]. Accordingly, the explosion scaling factor was set to $S = 1$, which is the reference value for this class of spacecraft mass. The additional two to eight fragments larger than 1 m required for mass conservation were assigned to the interval between $L_{0,add} = 1\,\text{m}$ and $L_{1,add} = 5\,\text{m}$. This range provides a reasonable representation of the larger and more massive components located farther from the explosion centre.

Since the properties of the fragments are sampled from statistical distributions, a fixed random seed was used to ensure reproducibility. This also guarantees that the subsequent analyses of debris dispersion are influenced only by the dynamical structure of the problem, rather than by the specific randomly sampled debris population. Figure 3.1 shows the debris ejection velocity components generated by the reference isotropic explosion, with a colormap representing the corresponding ejection velocity magnitude.

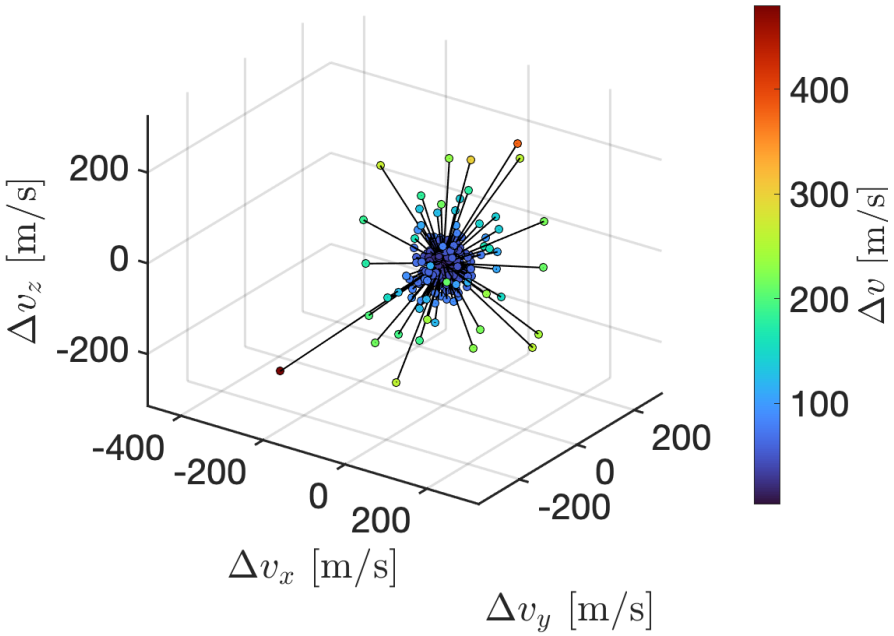
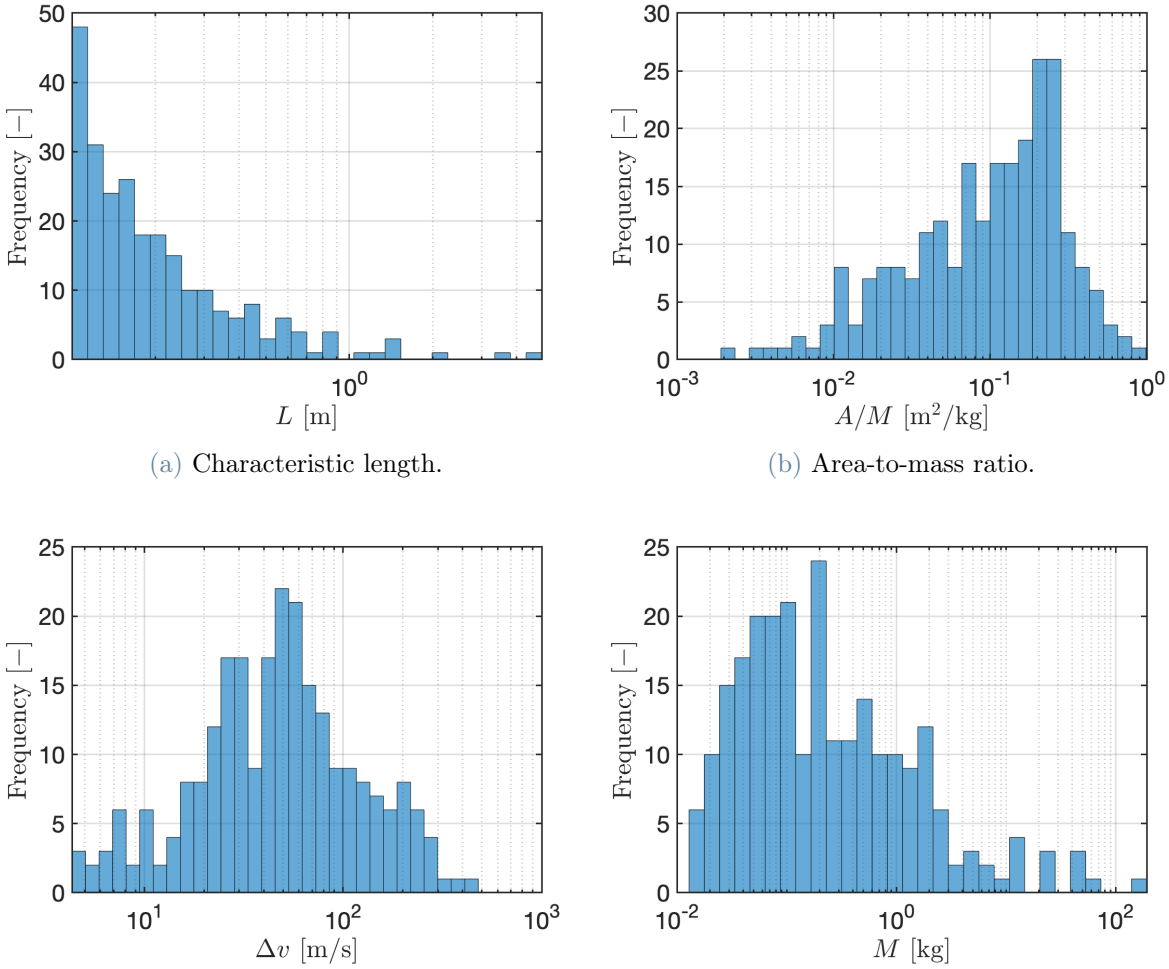


Figure 3.1: Reference explosion event.

Figure 3.2 shows the frequency distributions of the main properties of the generated debris fragments, namely the characteristic length L, area-to-mass ratio A/M, ejection velocity Δv, and mass M. The resulting trends are analogous to those reported by Boone et al. [39] and Guardabasso et al. [46] for the same breakup modelling framework, thus supporting the validity of the implemented sampling procedure. The characteristic length distribution is dominated by smaller fragments, consistently with the inverse power-law behaviour prescribed by the NASA SBM, while progressively fewer objects are generated at larger sizes. The area-to-mass ratio and ejection velocity distributions show a broader variability, reflecting the statistical nature of the breakup process and the dependence of the ejection speed on the sampled physical properties of each fragment. Similarly, the mass distribution is characterised by a large number of relatively small fragments, with a limited subset of larger debris contributing more significantly to the total mass budget.



(a) Characteristic length.

(b) Area-to-mass ratio.

(c) Ejection velocity.

(d) Debris mass.

Figure 3.2: Distributions of the debris properties for the reference explosion event.

3.2. Breakup framework for Halo orbits

The family of southern Earth–Moon L_2 Halo orbits was generated by applying the differential correction scheme and the numerical continuation method described in Secs. 2.4.2 and 2.4.3, respectively. The nonlinear ODEs associated with the state vector and STM propagation were solved using the Matlab `ode78` integrator, with absolute and relative tolerances set to 10^{-12}. This solver was selected for its effectiveness in celestial mechanics applications, where high accuracy is required at each integration step. The stringent tolerance values were imposed to account for the sensitivity of the nonlinear dynamics, ensuring the robustness and reliability of the computed solutions. Figure 3.3 shows the resulting family of southern Halo orbits coloured by perilune radius r_p, while Fig. 3.4 shows the evolution of the main parameters along the family as a function of x_0 or JC.

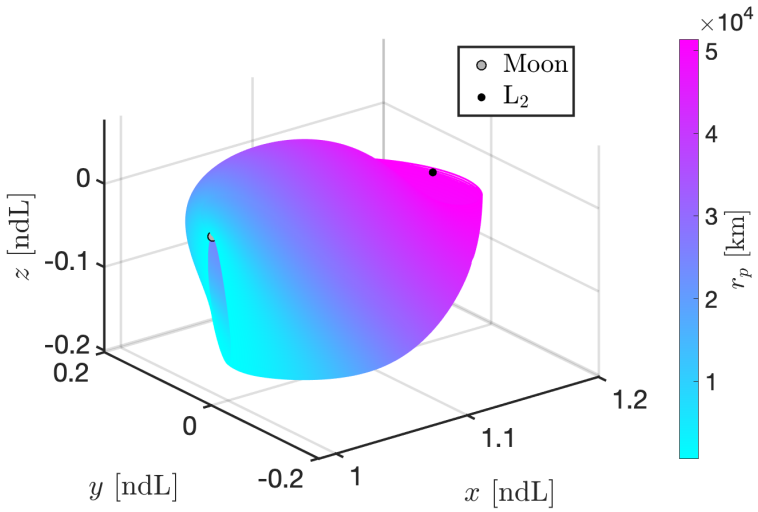
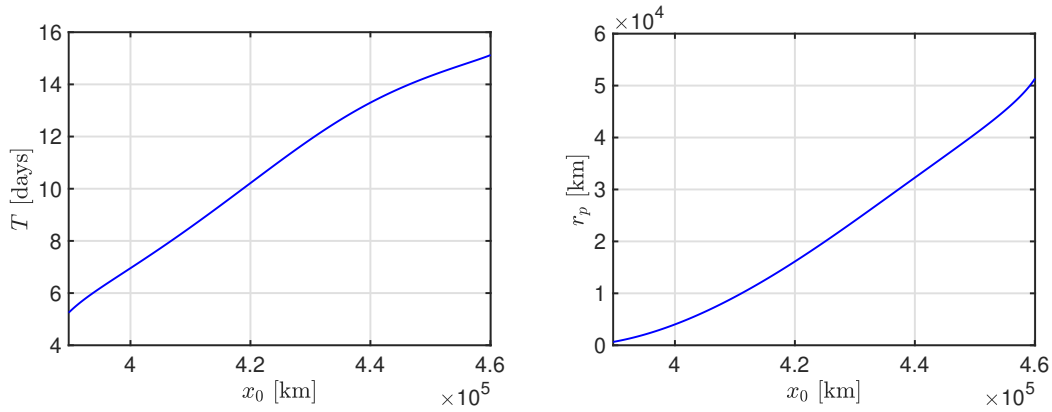


Figure 3.3: Family of southern Earth–Moon L_2 Halo orbits with a colormap on r_p.



(a) Orbital period.

(b) Perilune radius.

(c) Jacobi constant.

(d) Stability index.

Figure 3.4: Evolution of the main parameters along southern Earth–Moon L_2 Halo orbits.

A subset of N_{orbits} representative orbits was selected for the present analysis by considering equally spaced values of SI. This parameter was chosen because it provides direct insight into the dynamical properties along the family, allowing possible correlations to be identified between debris transport mechanisms and the stable or unstable behaviour of the parent trajectory. Since the value of N_{orbits} may vary among the simulation cases, its specific value is reported in the corresponding analysis.

For each selected Halo orbit, N_{phase} breakup locations were defined from equally spaced values of the phase angle θ. Since θ is obtained by linearly scaling the propagation time over $[0, 2\pi]$, this corresponds to equally spaced times along the orbit, rather than to equally spaced distances. The resulting locations are therefore denser near the apolune, where the spacecraft has a longer residence time, consistently with the assumption of a time-uniform breakup probability. Although alternative criteria based on arc length could be adopted, they were not considered here since they would assign a larger weight to the perilune region. The specific value of N_{phase} is reported in the corresponding analysis, since it may vary among the simulation cases.

At each breakup location, a population of N_{debris} fragments was generated according to the breakup modelling procedure described in Sec. 3.1 and propagated forward in time up to the final epoch t_f. Therefore, the complete analysis involves a total number of propagated debris trajectories equal to:

$$N_{\text{orbits}} \times N_{\text{phase}} \times N_{\text{debris}} \tag{3.1}$$

The reference breakup event was initially simulated on a single southern Earth–Moon L_2 NRHO similar to the 9:2 synodic resonant orbit considered in the original Lunar Gateway mission architecture. The initial conditions for the trajectory propagations were retrieved from the NASA JPL Three-Body Periodic Orbits database [88], and the orbit periodicity was further refined by applying the differential correction algorithm described in Sec. 2.4.2. The main parameters of the target NRHO are reported in Table 3.1, including the Jacobi constant JC, the stability index SI, the perilune radius r_p, and the orbital period T. Figure 3.5 shows the reference NRHO together with 20 equally spaced values of θ, marked in red for illustrative purposes.

Table 3.1: Main parameters of the reference NRHO.

JC [−]	SI [−]	r_p [km]	T [days]
3.0489	1.2554	2930.5921	6.5602

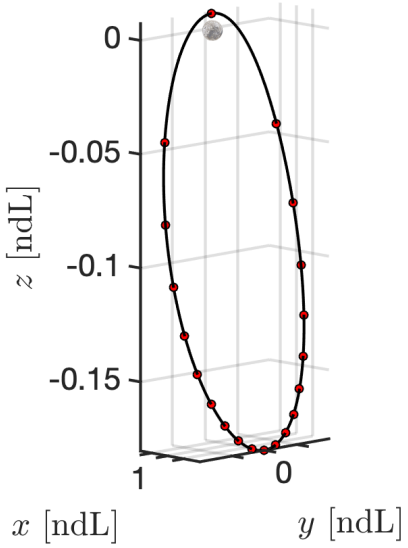


Figure 3.5: Reference NRHO with 20 equally spaced values of θ.

3.3. Breakup framework for disposal trajectories

The analysis of cislunar breakup events was then extended to relevant disposal trajectories associated with the unstable invariant manifold of the reference NRHO introduced in Tab. 3.1. As discussed in Sec. 2.5, these natural transport structures provide preferential departure pathways from the vicinity of the periodic orbit, representing a relevant dynamical mechanism for end-of-life disposal in the Earth–Moon system.

The manifold trajectories were generated following the procedure described in Sec. 2.5. In particular, a perturbation of magnitude $\varepsilon = 10^{-4}$ was applied along the unstable eigendirection, with a negative sign selected to obtain the unstable manifold branch leading to the largest number of direct escapes from the Earth–Moon system [89]. This branch was then propagated forward in time, producing trajectories that depart from the Halo orbit and progressively evolve towards the exterior cislunar region.

In the present work, only the subset of unstable manifold trajectories associated with phase angle values between $\theta = 100°$ and $\theta = 120°$ was considered. According to the disposal methodology proposed by Bolis et al. [90], this interval identifies the most favourable departure region for end-of-life disposal from the reference NRHO. Figure 3.6 shows the resulting branch of the unstable manifold associated with the reference orbit, with a colormap based on the departure phase angle θ from the parent orbit. The trajectories corresponding to the selected disposal range are highlighted in red.

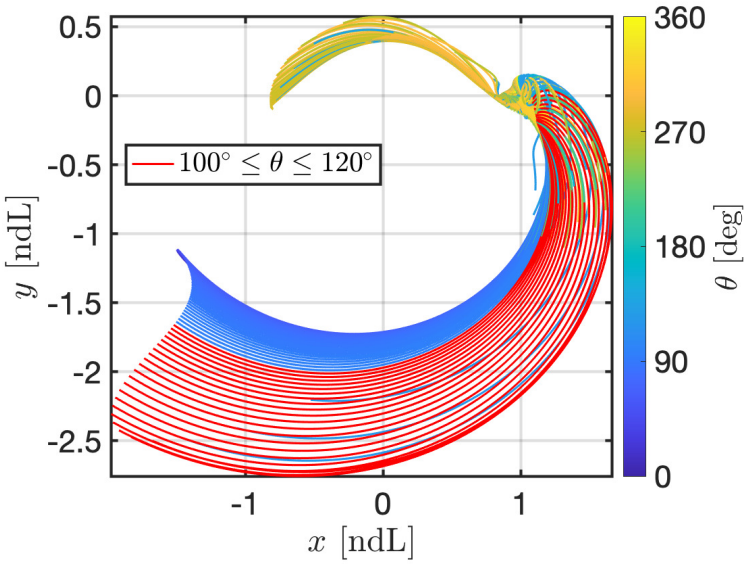


Figure 3.6: Unstable manifold associated with the reference NRHO.

The selected manifold trajectories were then used as parent trajectories for the breakup analysis. The simulation framework assumes that the spacecraft is injected onto one of these unstable manifold trajectories and is propagated forward in time until a breakup event occurs at time t_{break}. The resulting debris population is subsequently propagated forward in time up to the final epoch t_f. It is useful to introduce the debris time of flight, defined as the time elapsed from the breakup epoch t_{break} to the final simulation time t_f:

$$\Delta t_{\text{debris}} = t_f - t_{\text{break}} \tag{3.2}$$

Let N_{phase} denote the number of unstable manifold trajectories departing from the reference NRHO within the selected phase angle interval. Let N_{break} be the number of breakup locations considered along each manifold trajectory, corresponding to the selected values of the breakup time t_{break}. Finally, let N_{debris} be the number of fragments generated by the reference breakup event described in Sec. 2.1. Overall, the complete analysis involves a total number of propagated debris trajectories equal to:

$$N_{\text{phase}} \times N_{\text{break}} \times N_{\text{debris}} \tag{3.3}$$

4 | Analysis of results

This chapter presents the results of the cislunar breakup simulations. The analysis first focuses on breakup events along the reference southern Earth–Moon L_2 NRHO, introducing the numerical and dynamical tools used to characterise the debris cloud evolution. The numerical study is then extended to the corresponding family of Halo orbits to assess how the parent orbit and breakup location influence fragment dispersion. Finally, breakup events along disposal trajectories associated with the unstable manifold of the reference NRHO are analysed, highlighting the role of natural transport mechanisms in shaping the subsequent evolution of the debris population.

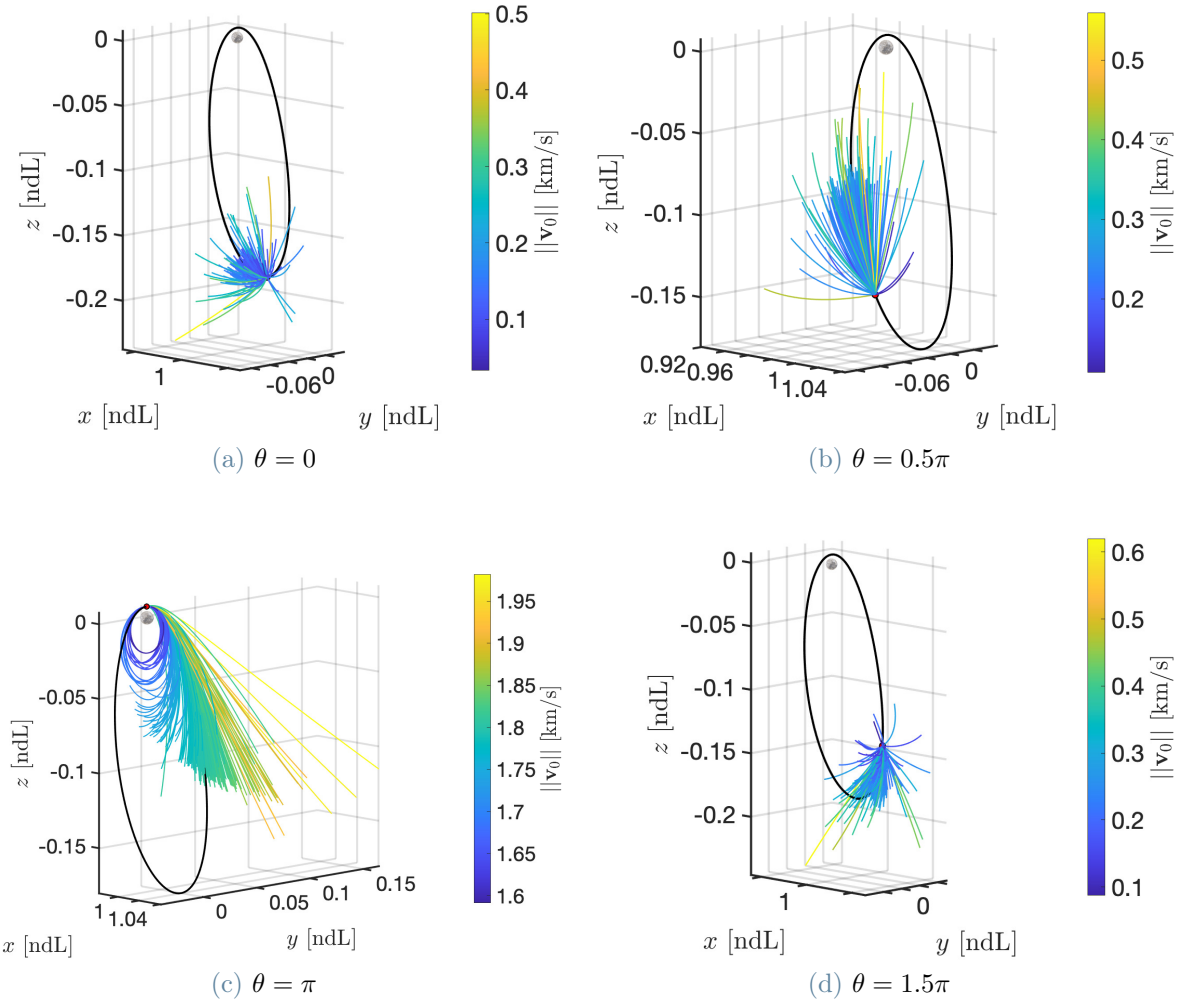
4.1. Breakup events on Halo orbits

4.1.1. Debris trajectory evolution

Figure 4.1 shows the debris trajectories generated by breakup events occurring at four representative phase angles along the reference NRHO, namely $\theta = 0$, 0.5π, π and 1.5π. The trajectories are initially propagated for 24 hours and coloured according to the norm of the post-breakup velocity $\|\boldsymbol{v}_0\|$, with $\boldsymbol{v}_0(\theta) = \boldsymbol{v}_{\text{Halo}}(\theta) + \Delta\boldsymbol{v}$. The breakup location is marked in red along the reference orbit. This representation provides a first qualitative insight into the debris evolution patterns, highlighting their dependence on the breakup location and on the initial velocity magnitude of the fragments.

The breakup at $\theta = 0$, corresponding to the apolune of the Halo orbit, results in a slower and more confined short-term evolution, with the fragments remaining close to the parent trajectory. The debris cloud is broadly dispersed in the rotating frame, with only a slight bias along the direction of the parent spacecraft velocity. This behaviour reflects the comparable magnitudes of the spacecraft velocity at apolune, $v_{\text{apolune}} = 99.78$ m/s, and the mean ejection velocity generated by the breakup event, $\Delta\bar{v}_{\text{debris}} = 69.78$ m/s.

The breakup at $\theta = \pi$, corresponding to the perilune of the Halo orbit, leads to a faster separation from the breakup point, with the trajectories forming an elongated cloud within the first day. In this case, the debris population exhibits a preferential dispersion direction



(a) $\theta = 0$ (b) $\theta = 0.5\pi$

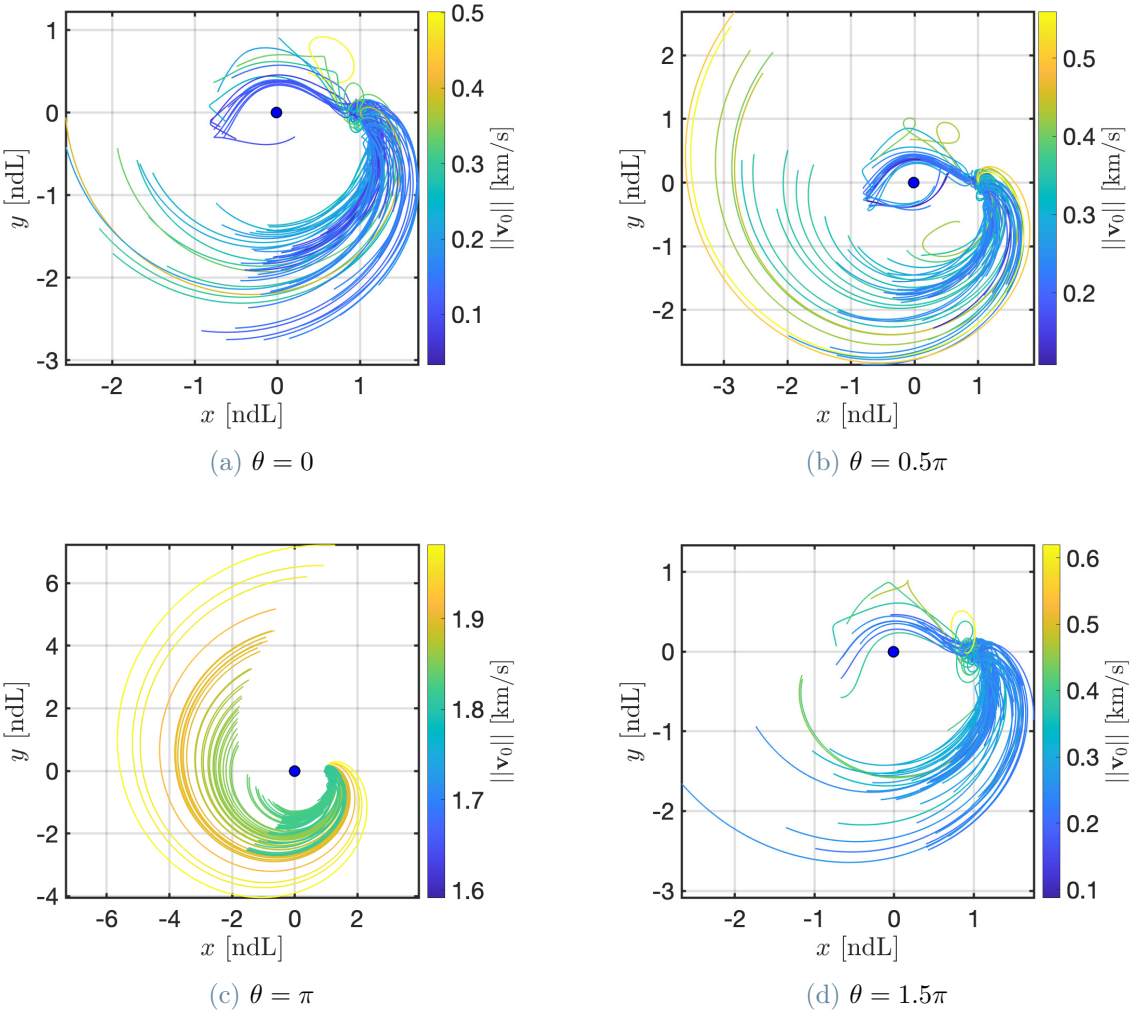
(c) $\theta = \pi$ (d) $\theta = 1.5\pi$

Figure 4.1: Debris trajectories after 24 hours in the EMB rotating frame.

aligned with the motion of the parent spacecraft. This can be attributed to the large spacecraft velocity at perilune, $v_{\text{perilune}} = 1801.37$ m/s, which is significantly higher than the mean ejection velocity of the fragments generated by the breakup event. The resulting evolution is strongly influenced by the magnitude of the post-breakup velocity. Fragments with larger values of $\|\boldsymbol{v}_0\|$ depart more rapidly from the reference orbit, those with smaller values evolve on tighter lunar orbits, while fragments with intermediate values remain closer to the reference NRHO for a longer time interval.

The breakups at $\theta = 0.5\pi$ and $\theta = 1.5\pi$ show an intermediate behaviour, with most fragments initially following the motion of the parent Halo orbit. However, the two cases are not fully symmetric. At $\theta = 0.5\pi$, the debris cloud exhibits a slightly faster and more elongated evolution as the fragments move towards the perilune. At $\theta = 1.5\pi$, the dispersion is slower and more diffuse, as the fragments move away from the Moon.

The debris trajectories generated by the same breakup events are then propagated within the Earth–Moon CR3BP for 30 days, as shown in Fig. 4.2. The longer propagation confirms the trends already observed over 24 hours, while revealing the global transport pattern of the debris cloud. For the breakups at $\theta = 0$, $\theta = 0.5\pi$ and $\theta = 1.5\pi$, part of the fragments appears to depart from the L_2 region in a clockwise direction, while another portion is transported towards the inner region following a counter-clockwise motion. Conversely, the breakup at $\theta = \pi$ does not produce the same two-lobed cloud structure, since the slower fragments that would form the inner lobe are more efficiently captured by the Moon. In this case, the debris cloud mainly evolves clockwise towards the L_2 region, with some trajectories rapidly departing from the cislunar region and others remaining on tighter and slower orbits.



(a) $\theta = 0$ (b) $\theta = 0.5\pi$

(c) $\theta = \pi$ (d) $\theta = 1.5\pi$

Figure 4.2: Debris trajectories after 30 days in the EMB rotating frame.

4.1.2. Debris event counters

The evolution of the debris population was further analysed by tracking the number of fragments associated with different regions of cislunar space. In particular, four counters were introduced: N_{SOI}, identifying the fragments evolving within the Earth–Moon Sphere of Influence (SOI); N_{Moon}, associated with impacts on the Moon; N_{Earth}, associated with impacts on the Earth; and N_{exit}, corresponding to fragments located outside the Earth–Moon SOI. All the debris trajectories were propagated for 1 year with a time step of 1 hour, unless a stopping condition was encountered. For lunar impacts, the propagation was terminated when a fragment reached the lunar surface, modelled as a sphere with mean lunar radius. For Earth impacts, the propagation was terminated when the fragment altitude above the Earth reached 120 km, approximately corresponding to the beginning of the Earth's atmosphere. Conversely, the propagation was not stopped when a fragment crossed the Earth–Moon SOI radius, taken equal to 913,000 km from the Earth–Moon centre of mass. This choice allows the counters to account for the instantaneous location of the debris fragments, since they may leave and later re-enter the SOI multiple times during the propagation interval.

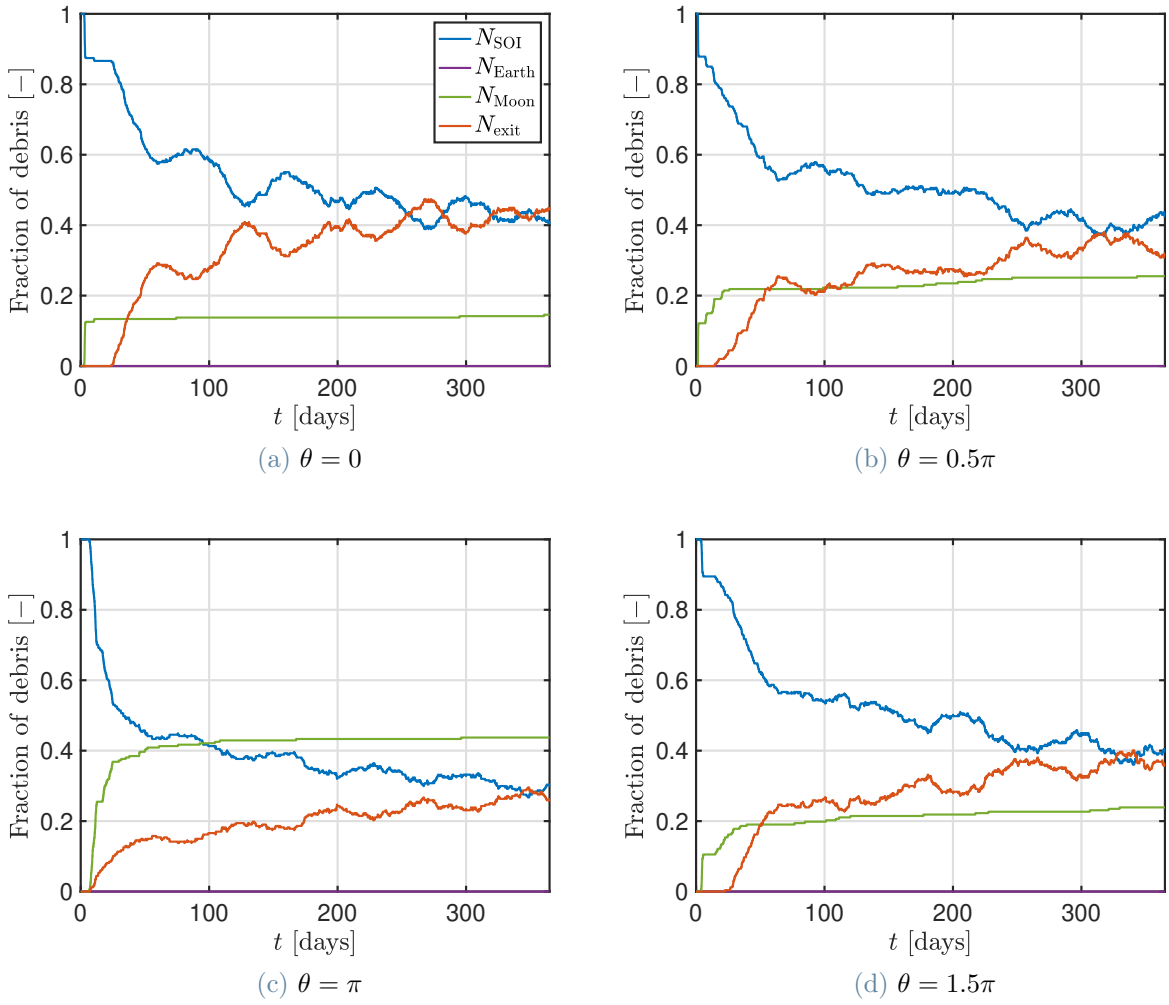
Representative breakup locations

Figure 4.3 shows the temporal evolution of the debris event counters for the four representative breakup locations along the reference NRHO, namely $\theta = 0$, 0.5π, π and 1.5π. Each panel refers to a fixed breakup location and reports the corresponding evolution of N_{SOI}, N_{Moon}, N_{Earth} and N_{exit} over the 1 year propagation interval from the breakup event. The corresponding final values are summarised in Tab. 4.1, where the counters are reported as percentages of the initial debris population.

Table 4.1: Debris event counters along the reference NRHO after 1 year.

Phase angle	N_{SOI} [%]	N_{Moon} [%]	N_{Earth} [%]	N_{exit} [%]
$\theta = 0.0\pi$	40.5	14.6	0.0	44.9
$\theta = 0.5\pi$	42.5	25.5	0.0	32.0
$\theta = 1.0\pi$	30.0	43.7	0.0	26.3
$\theta = 1.5\pi$	39.7	23.9	0.0	36.4

The breakup at $\theta = 0$, corresponding to the apolune of the NRHO, leads to the lowest final number of lunar impacts among the considered breakup locations. In this case, N_{Moon} exhibits an initially steep increase, followed by an almost horizontal plateau reached within



(a) $\theta = 0$ (b) $\theta = 0.5\pi$

(c) $\theta = \pi$ (d) $\theta = 1.5\pi$

Figure 4.3: Debris event counters along the reference NRHO, grouped by breakup location.

the first 4 days after the breakup event. This behaviour indicates that lunar impacts occur over a short timescale, while only a marginal probability of impacts is still present at later times. The increase of N_{exit} begins approximately 24 days after the breakup event. Its evolution then shows a progressively increasing trend, with a clear oscillatory behaviour superimposed on the long-term growth. This trend is associated with fragments moving on progressively departing trajectories characterised by radial excursions with respect to the Earth–Moon centre of mass [91]. As their distance periodically crosses the adopted SOI radius, the same debris objects may alternately leave and re-enter the Earth–Moon SOI, producing the observed oscillations. No Earth impacts are observed over the considered simulation time for this breakup location. Finally, N_{SOI} shows a complementary evolution. It first decreases as a consequence of the early lunar impacts, and subsequently follows an oscillatory decreasing trend that mirrors the progressive increase of N_{exit}.

The breakup at $\theta = 0.5\pi$ again shows an initially steep increase of N_{Moon}, analogous to the behaviour observed for $\theta = 0$. This first growth phase is followed by several stepwise increases, which nearly double the number of fragments impacting the Moon, before an approximately flat trend is reached after about 30 days. A slight gradual increase in N_{Moon} is also observed after the first 150 days, indicating that a residual probability of lunar impacts persists over longer timescales for breakup events occurring at this phase angle. The increase of N_{exit} begins approximately 14 days after the breakup event, leading to a lower final number of debris fragments outside the SOI than in the case of $\theta = 0$. This is associated with the larger number of lunar impacts, which reduces the debris population available to leave the SOI. The oscillatory behaviour superimposed on the long-term growth is also less pronounced than for $\theta = 0$, suggesting that the radial excursions of the fragments moving away from the Earth–Moon system are more limited. As a result, most debris objects do not re-enter the SOI after crossing its boundary. No Earth impacts are observed over the considered simulation time for this breakup location. Finally, N_{SOI} again shows a complementary trend with respect to the evolution of N_{Moon} and N_{exit}.

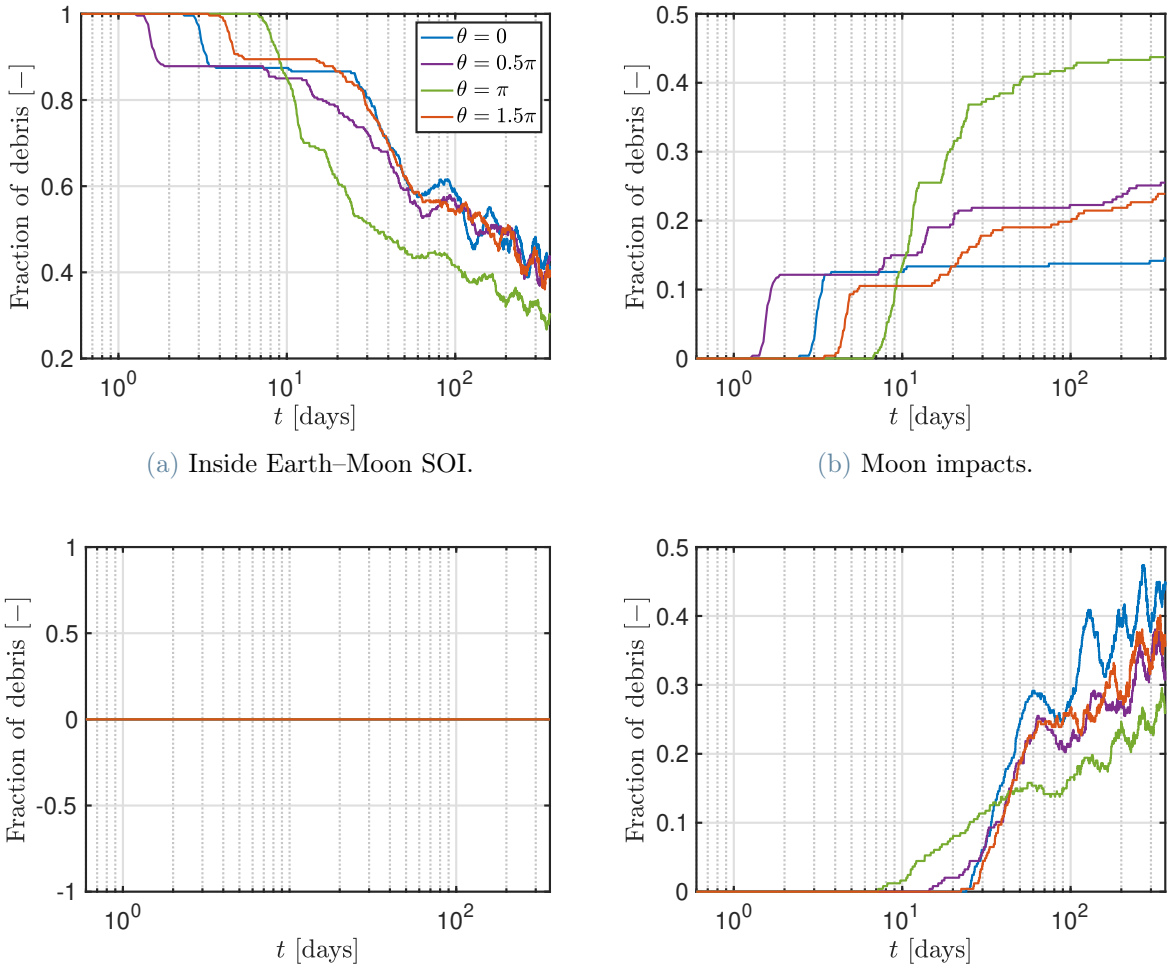
The breakup at $\theta = \pi$, corresponding to the perilune of the NRHO, leads to the highest final number of lunar impacts. At the same time, it shows a more gradual accumulation of impacts than the other breakup locations, reaching an almost horizontal plateau only about 100 days after the breakup event. This slower growth can be related to the temporary capture of part of the debris population onto smaller orbits around the Moon, whose subsequent evolution contributes to delayed lunar impacts. The increase in N_{exit} begins approximately 7 days after the breakup event, leading to a final number of debris objects outside the Earth–Moon SOI comparable to the case of $\theta = 0.5\pi$. Since the larger number of lunar impacts significantly reduces the debris population available for escape, this result suggests that a higher fraction of the remaining fragments evolves onto departing trajectories. This is also reflected in the final value of N_{SOI}, which is the lowest among all the considered breakup locations. The oscillatory behaviour superimposed on the growth of N_{exit} is very weak, indicating that most debris objects moving on departing trajectories do not re-enter the SOI after crossing its boundary. No Earth impacts are observed over the considered simulation time for this breakup location. Finally, N_{SOI} again shows a complementary trend with respect to the evolution of N_{Moon} and N_{exit}. Differently from the previous breakup locations, the increases in N_{Moon} and N_{exit} are comparable and occur over similar timescales. Therefore, the decrease in N_{SOI} is not driven by two clearly separated phases, but by the combined effect of lunar impacts and SOI exits.

The breakup at $\theta = 1.5\pi$ shows an intermediate behaviour, similar to the case of $\theta = 0.5\pi$. An initially steep increase of N_{Moon} is observed, followed by a more gradual growth

phase that nearly doubles the cumulative number of fragments impacting the Moon. An approximately flat trend is then reached after about 40 days. Also in this case, a further slight increase in N_{Moon} is observed after about 80 days, indicating that a residual probability of lunar impacts persists over longer timescales at this phase angle. The evolution of N_{exit} is analogous to that observed for $\theta = 0.5\pi$, both in terms of final value and oscillatory behaviour. The less pronounced oscillations suggest that most fragments leaving the Earth–Moon SOI do not repeatedly cross the adopted boundary. Similarly to the previous cases, no Earth impacts are observed, while N_{SOI} decreases as fragments either impact the Moon or leave the SOI.

Similar results were reported by Guardabasso et al. [46] and Boone et al. [39], although with relevant differences in the post-processing strategy. Guardabasso et al. considered snapshot statistics for analogous counters, while continuously monitoring only impacts with the Moon and Earth. Boone et al. reported cumulative results over all breakup simulations, but terminated the propagation when fragments crossed the Earth–Moon SOI, treating them as escaped from the system. Conversely, in the present work, SOI crossings are not used as stopping conditions, allowing possible later re-entries into the Earth–Moon SOI to be retained in the analysis. Despite these differences, the trends reported for similar NRHO configurations are consistent with the present results. This agreement is particularly relevant because both studies used ephemeris dynamical models, while the present analysis is performed within the CR3BP. Therefore, the comparison supports the proposed framework and suggests that the CR3BP captures the dominant features of the statistical evolution of the debris counters with good accuracy.

An alternative representation of the debris event counters is shown in Fig. 4.4. In this case, each panel refers to one debris counter, while the different curves correspond to the four breakup locations along the orbit. The time axis is represented on a semilogarithmic scale, allowing the evolution of each counter to be visualised more clearly within the first days after the breakup event. As also observed by Guardabasso et al. [46], the first steep increase in N_{Moon} can be associated with the first subsequent passage of the debris cloud through the perilune region of the NRHO. This explains the sequence in which the initial lunar impact growth appears for the different breakup locations, namely $\theta = 0.5\pi$, $\theta = 0$, $\theta = 1.5\pi$ and finally $\theta = \pi$. Further increases in N_{Moon} may then occur at later passages of the debris cloud through the same region. This is particularly evident for $\theta = 0.5\pi$, where the stepwise growth previously described can be related to the orbital period separating consecutive passages through the perilune region. The consistency with the results reported in [46] suggests that the CR3BP reproduces not only the final values, but also the dynamical trends of the debris counters with good fidelity.



(a) Inside Earth–Moon SOI.

(b) Moon impacts.

(c) Earth impacts.

(d) Exited Earth–Moon SOI.

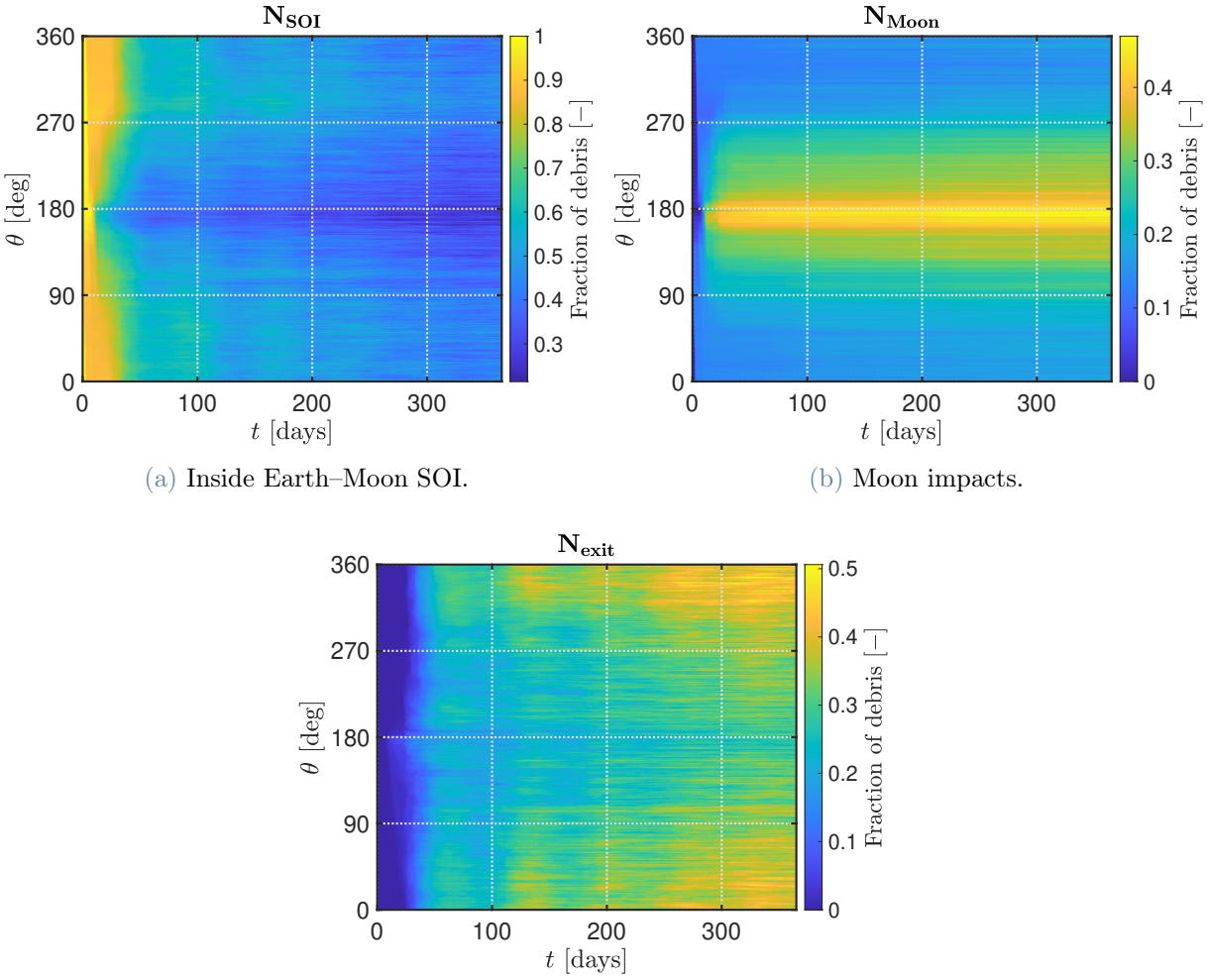
Figure 4.4: Debris event counters along the reference NRHO, grouped by counter type.

Global dependence on the phase angle at breakup

The previous analysis presented in Figs. 4.3 and 4.4 focused on four representative breakup locations along the reference NRHO. This allowed the main features of the evolution of debris event counters to be identified, including the characteristic timescales of lunar impacts, exits and possible re-entries into the Earth–Moon SOI. However, these four cases provide only a discrete description of the dependence of the debris evolution on the breakup location. To obtain a more continuous representation, the analysis was extended to breakup events occurring along the entire reference NRHO.

In particular, breakup events were simulated over the interval $\theta \in [0°, 360°]$ with a resolution of 1°. For each breakup location, the debris population was propagated for 1 year using the same simulation setup adopted in the previous analysis. The resulting

counters were normalised with respect to the initial debris population and collected into two-dimensional maps shown in Fig. 4.5. In this representation, the horizontal axis denotes the elapsed time after the breakup, the vertical axis identifies the breakup phase angle and the colormap indicates the fraction of fragments associated with each counter. The maps are reported for N_{SOI}, N_{Moon} and N_{exit}, providing a global view of the sensitivity of the debris evolution to the breakup location along the NRHO. Since no Earth impacts were observed over the considered propagation interval, N_{Earth} is not shown.



(a) Inside Earth–Moon SOI.

(b) Moon impacts.

(c) Exited Earth–Moon SOI.

Figure 4.5: Debris event counter maps along the reference NRHO.

The map of N_{Moon} is mainly organised into horizontal bands, showing that the fraction of lunar impacts is strongly dependent on the breakup phase angle. The largest impact fractions are concentrated around $\theta \simeq 180°$, corresponding to the perilune region of the NRHO. This confirms the trend already observed in the four representative cases, where

the breakup at $\theta = \pi$ produced the highest value of N_{Moon}. In the same phase angle region, N_{SOI} reaches its lowest values, indicating that a significant portion of the debris population is removed from the cislunar region through lunar impacts. Conversely, breakup locations farther from perilune are associated with progressively smaller fractions of lunar impacts, with a minimum near the apolune region. This is reflected in a larger fraction of fragments remaining inside the SOI at early times and exiting it over longer timescales.

The map of N_{exit} shows a more gradual temporal evolution and a less localised dependence on the breakup phase angle. Unlike N_{Moon}, which reaches an almost steady distribution within a few weeks, N_{exit} continues to increase over longer timescales for most breakup locations. This indicates that SOI exits are not driven by a single short-term dynamical mechanism, but rather by the progressive transport of fragments onto departing trajectories. The irregular structures visible in the maps are consistent with the fact that SOI crossings are not treated as terminal events in the present analysis. As a result, fragments may leave the Earth–Moon SOI and later re-enter it during the propagation interval. This also explains the complementary oscillations observed in N_{exit} and N_{SOI}, which are associated with repeated excursions across the adopted SOI boundary.

These maps confirm that breakup events occurring near perilune are the most critical in terms of lunar impacts. Conversely, breakups farther from this region produce fewer lunar impacts, a larger fraction of fragments inside the SOI at early epochs and a higher contribution of SOI exits over long propagation times. Additional debris event counter maps associated with Halo orbits with different SI values are reported in Appendix A.

Cumulative counters along the reference NRHO

Figure 4.6 provides a compact representation of the cumulative debris event counters along the reference NRHO, similar to the one proposed by Boone et al. [39]. The breakup locations were obtained by sampling the full phase angle interval $\theta \in [0°, 360°]$ with a resolution of 1°, consistently with the discretisation adopted in the previous analysis. The figure reports the counters obtained by summing the contributions from all sampled breakup locations and normalising them with respect to the total number of fragments generated over all these events. This representation is useful because it associates the reference orbit with an average temporal evolution of the debris counters, thus enabling a direct comparison with other Halo orbits. In this case, the resulting trend is analogous to that observed for breakups near apolune, consistently with the fact that a spacecraft on an NRHO spends most of its residence time within this orbital region. Additional examples of cumulative debris event counters associated with Halo orbits with different SI values are reported in Appendix B.

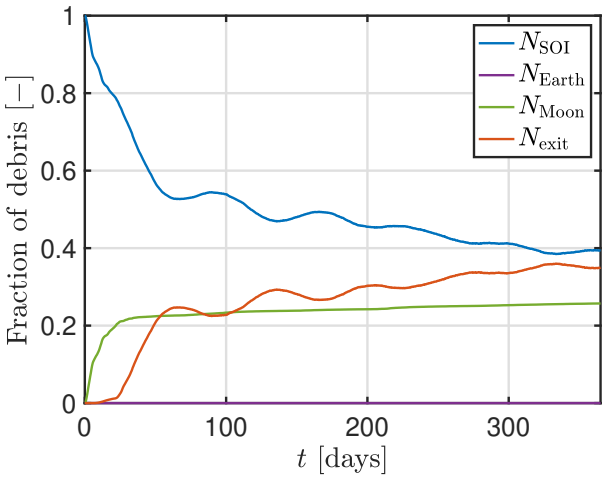
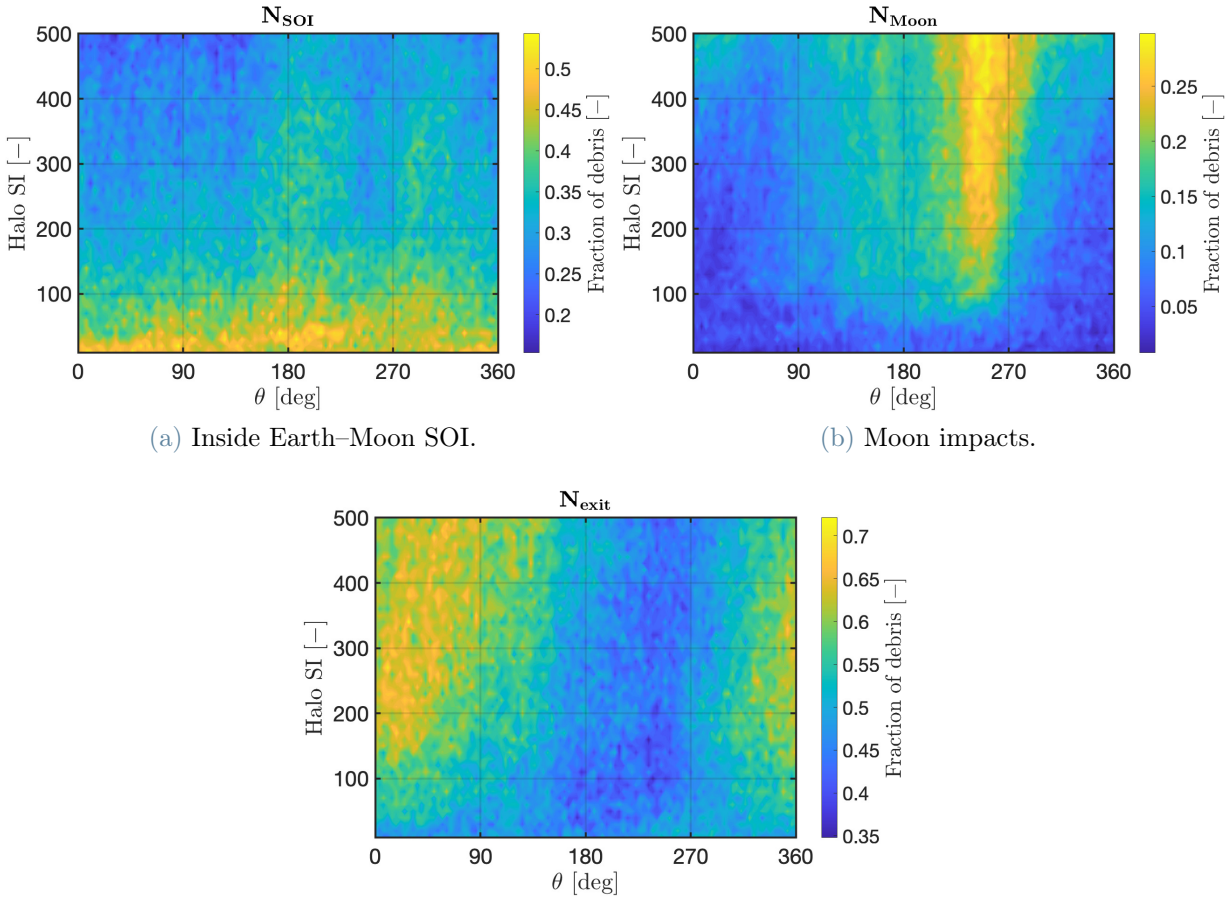


Figure 4.6: Cumulative debris event counters along the reference NRHO.

Debris event counters along the Halo family

The debris event counter analysis was extended to the family of southern Earth–Moon L_2 Halo orbits obtained in Sec. 3.2. A representative subset of 50 orbits was uniformly sampled in $SI \in [10, 500]$ [–]. As previously shown in Fig. 3.4, larger values of SI correspond to Halo orbits located progressively farther from the Moon. This subset does not include the NRHO regime, which was analysed separately in the previous sections. For each orbit, the breakup locations were defined by sampling the phase angle with 100 equally spaced values over $\theta \in [0°, 360°]$. The debris populations were then propagated for 1 year using the same simulation setup adopted in the previous sections. The results of these simulations are collected in the two-dimensional maps shown in Fig. 4.7. In these maps, the horizontal axis denotes the breakup phase angle along each orbit, the vertical axis denotes the SI values of the selected Halo orbits and the colormap indicates the fraction of fragments associated with each debris event counter after 1 year.

The map of N_{Moon} shows that the fraction of lunar impacts starts to increase approximately from $\theta = 90°$, reaching its maximum for $\theta \in [230°, 270°]$. This trend is observed for all the selected Halo orbits, although it becomes less pronounced for $SI \in [10, 100]$ [–]. This behaviour differs from that observed for the reference NRHO, where the maximum was concentrated around $\theta = 180°$. The difference can be attributed to the distinct geometry and dynamical properties of the orbits considered in the two analyses. The reference NRHO is strongly elongated, with an apolune region far from the Moon at $\theta = 0°$ and a perilune passage very close to the lunar surface at $\theta = 180°$. In that case, the lunar impact dynamics is mainly governed by the perilune region, which is characterised by a higher degree of local chaoticity compared with the rest of the orbit.



(a) Inside Earth–Moon SOI.

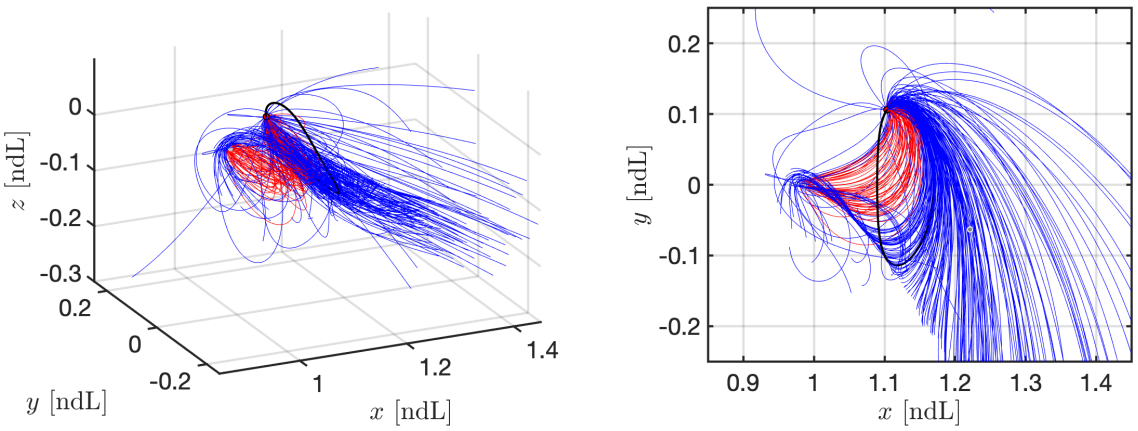
(b) Moon impacts.

(c) Exited Earth–Moon SOI.

Figure 4.7: Debris event counter maps along the Halo family after 1 year.

Conversely, the Halo orbits analysed here are larger periodic solutions located between the Moon and L_2, and their distance from the Moon varies less sharply along the orbit than for the reference NRHO. As a result, the impact process is no longer dominated by a single close perilune passage. Instead, the maximum of N_{Moon} appears in the region where the Halo orbits cross the x-y plane from positive to negative values of z, corresponding indeed to the phase angle interval $\theta \in [230°, 270°]$.

To further investigate this behaviour, a representative breakup was simulated on the Halo orbit with $SI = 300$ [–] at $\theta = 240°$, which lies within the region where the maximum value of N_{Moon} is observed. The corresponding debris trajectories are shown in Fig. 4.8, with lunar-impact trajectories highlighted in red and all the remaining ones shown in blue. The figure suggests that a fraction of fragments is injected onto direct-impact trajectories, reaching the lunar surface without first completing revolutions around the Moon. A similar behaviour is observed for the other values of SI when the breakup location is selected within the region of maximum N_{Moon}.



(a) Three-dimensional view.

(b) Projection on the x-y plane.

Figure 4.8: Debris trajectories for a Halo orbit with $SI = 300$ [−] at $\theta = 240°$.

Going back to the results of the parametric analysis, the map of N_{exit} shows that the largest fraction of SOI exits is obtained in the first portion of the orbit, close to $\theta = 0°$. This region forms an approximately triangular pattern in the (θ, SI) plane. For the most unstable orbits, corresponding to $SI \simeq 500$ [−], large values of N_{exit} extend over a broad phase angle interval, approximately up to $\theta \simeq 150°$. As SI decreases, this area progressively shrinks and becomes increasingly confined around $\theta \simeq 0°$. In the second half of the orbit, large values of N_{exit} are instead mainly confined to the region close to $\theta \simeq 360°$. The smallest values of N_{exit} are obtained approximately in the region $\theta \in [180°, 270°]$. However, this region is not completely uniform, as local discontinuities are present where the fraction of exiting debris increases.

Finally, the map of N_{SOI} shows a complementary behaviour with respect to the combined effect of N_{Moon} and N_{exit}. In particular, the largest fractions of debris remaining inside the SOI are observed approximately for $SI \in [10, 100]$ [−] over the full range of θ, and around $\theta = 180°$ for larger values of SI. In these regions, both N_{exit} and N_{Moon} remain relatively small. Conversely, the lowest values of N_{SOI} are found in the regions associated with the largest fractions of escaping debris.

An important feature emerging from the three maps is the absence of symmetry between the two halves of the orbit, namely $\theta \in [0°, 180°]$ and $\theta \in [180°, 360°]$. This indicates that the debris transport along the Halo orbits is not determined only by the geometric location of the breakup point, but also by the direction of motion of the parent object before fragmentation. Therefore, symmetric portions of the orbit may lead to different debris outcomes, depending on the way in which the breakup region is approached.

4.1.3. Post-breakup Jacobi constant distribution

This section analyses how the breakup event modifies the JC of the fragments with respect to the nominal value of the reference NRHO. Table 4.2 reports the fraction of debris whose post-breakup JC falls within the intervals bounded by the JC values of the Lagrange points. The table is constructed for the representative breakup locations selected in the previous sections, namely $\theta = 0$, 0.5π, π and 1.5π. As discussed in Sec. 2.2.6, these intervals are dynamically relevant because they determine the opening or closure of the ZVCs in the CR3BP framework. Therefore, the post-breakup JC can be used to infer which regions of the cislunar domain are energetically accessible to the debris fragments.

Table 4.2: Fraction of debris fragments in each JC interval.

Phase angle [rad]	Jacobi constant intervals [%]				
	$> JC_{L_1}$	JC_{L_2}–JC_{L_1}	JC_{L_3}–JC_{L_2}	JC_{L_4}–JC_{L_3}	$< JC_{L_4}$
$\theta = 0.0\pi$	0.0000	0.0000	90.6883	4.4534	4.8583
$\theta = 0.5\pi$	0.0000	0.0000	89.8785	3.2389	6.8826
$\theta = 1.0\pi$	16.5992	0.8097	51.8219	4.4534	26.3158
$\theta = 1.5\pi$	0.0000	0.0000	89.8785	4.8583	5.2632

The results reported in Table 4.2 show that, for the breakup locations at $\theta = 0$, 0.5π and 1.5π, most fragments remain within the JC_{L_3}–JC_{L_2} interval, with fractions close to 90%. This range corresponds to a configuration in which the necks at L_1 and L_2 are open, allowing interior and exterior transfers, while the passage through L_3 is still forbidden. Only a small fraction of the debris population is shifted towards lower JC values, associated with more energetic configurations and progressively larger admissible regions. At the same time, no fragments are found in the intervals above JC_{L_2}, which correspond to more confined ZVC configurations.

A different behaviour is observed for the breakup at $\theta = \pi$, where the fraction of fragments in the JC_{L_3}–JC_{L_2} interval decreases to approximately 52%. In this case, a significant portion of the cloud is shifted both above JC_{L_1} and below JC_{L_4}, indicating that the breakup near the perilune of the reference NRHO produces a wider redistribution of the debris JC values. The fragments shifted above JC_{L_1} are associated with dynamically confined lunar motion and therefore with a higher expected impact risk. On the other hand, the fragments shifted below JC_{L_4} belong to the most energetic range, where the planar forbidden regions vanish and the debris motion is no longer constrained by the ZVCs in the rotating plane.

Finally, Fig. 4.9 reports the mean and standard deviation of the JC of the debris cloud after the breakup as a function of the phase angle θ along the reference NRHO. Both quantities exhibit a peak near $\theta = \pi$, corresponding to the perilune region. This confirms the larger variability of the debris JC observed for the perilune breakup, while the energetic distribution remains more similar over the rest of the orbit.

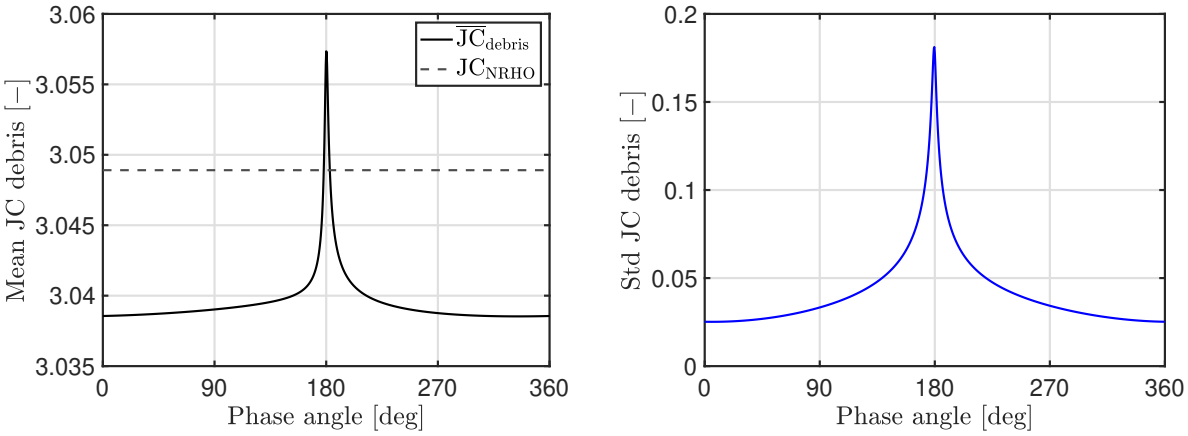


Figure 4.9: Mean and standard deviation of the JC of debris cloud as a function of θ.

4.1.4. Phase angle dependence of debris range

In this section, the distance of each fragment from the corresponding breakup location, denoted as $\rho(t)$, is analysed as a function of time. The breakup locations are distributed along the reference NRHO by sampling the phase angle interval $\theta \in [0°, 360°]$ with a resolution of 1°. The fragments are propagated for 1 month, so that the analysis focuses on the early phase of the debris evolution. In this sense, $\rho(t)$ provides a direct measure of the fragment separation from the reference NRHO and represents a compact indicator of the short-term debris dispersion.

Figure 4.10 shows the temporal evolution of $\rho(t)$, expressed in logarithm to base 10. Each curve is coloured according to the phase angle θ of the corresponding breakup event location along the NRHO. Two main regions can be identified. The first one, shown in light green, is associated with breakup events occurring around $\theta = 180°$, namely in the perilune region of the reference NRHO. This region forms a broad band spanning very different values of $\rho(t)$, consistently with the large energy dispersion previously observed in Sec. 4.1.3. The upper part of the band corresponds to fragments that rapidly depart from the vicinity of the parent orbit, whereas the lower part is populated by debris entering tighter lunar trajectories, which eventually lead to lunar impacts.

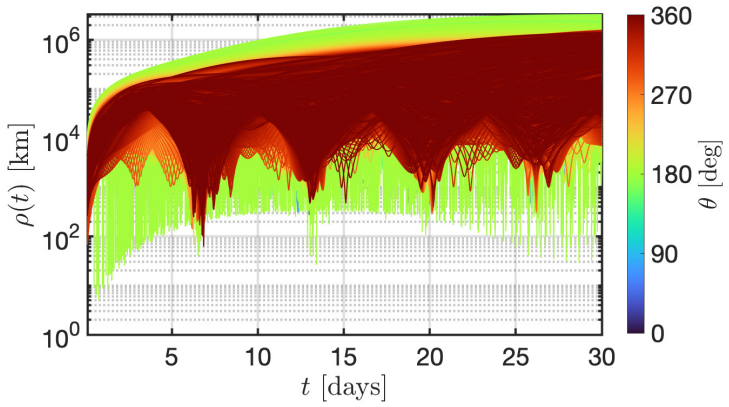


Figure 4.10: Temporal evolution of $\rho(t)$ with a colormap based on θ.

The second region, shown in red, is associated with debris generated from breakup locations in the second half of the orbit. This region is largely superimposed on an analogous one, shown in blue, corresponding to breakup locations in the first half of the orbit. Compared with the band associated with the perilune, these regions occupy a narrower subset of the $\rho(t)$ values and appear more compact. Some trajectories depart from the vicinity of the parent orbit through a nearly monotonic increase of $\rho(t)$, while others exhibit an oscillatory behaviour with a period close to that of the reference NRHO. These trajectories correspond to fragments that follow temporarily the dynamical behaviour of the parent orbit, before either departing from its neighbourhood or terminating in a lunar impact.

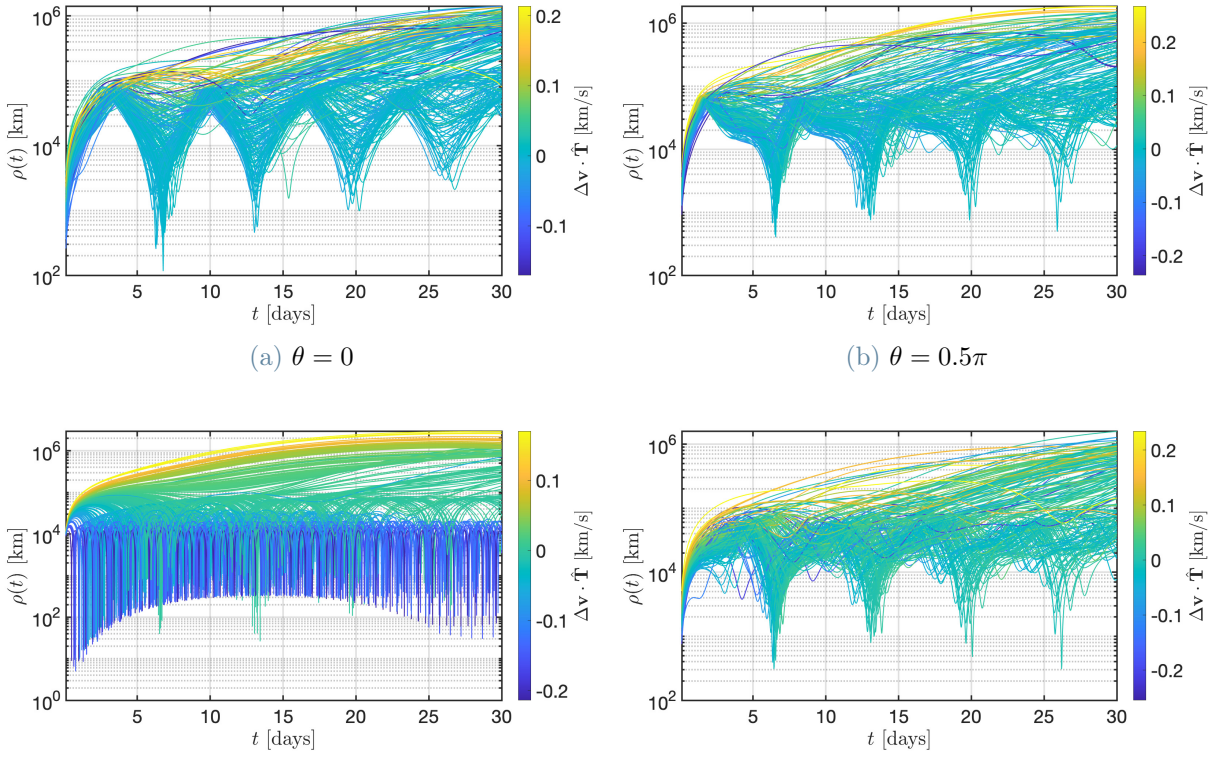
4.1.5. TNB velocity projections and debris range

The evolution of the debris cloud is further analysed by studying how the debris range $\rho(t)$ is related to the projection of the ejection velocity $\Delta\boldsymbol{v}$ onto the local Tangent-Normal-Binormal (TNB) frame of the reference NRHO at the breakup point. The same propagation interval of 1 month was considered in order to characterise the initial dispersion of the debris cloud and the departure of the fragments from the vicinity of the parent orbit. In this case, the analysis focuses again on relevant breakup locations along the reference NRHO, namely $\theta = 0$, 0.5π, π and 1.5π.

The TNB frame (or Frenet-Serret frame) associated with a trajectory generated by the CR3BP vector field can be locally defined from the spatial curve $\boldsymbol{r}(t)$ and its time derivatives, namely the velocity $\boldsymbol{v}(t) = \dot{\boldsymbol{r}}(t)$ and the acceleration $\boldsymbol{a}(t) = \dot{\boldsymbol{v}}(t)$. The tangent direction $\hat{\mathbf{T}}$ is aligned with the instantaneous velocity, the normal direction $\hat{\mathbf{N}}$ identifies the local curvature direction and the binormal direction $\hat{\mathbf{B}}$ is normal to the osculating plane [92]. The corresponding unit vectors are defined as follows:

$$\hat{\mathbf{T}} = \frac{\boldsymbol{v}}{\|\boldsymbol{v}\|}$$
$$\hat{\mathbf{N}} = \frac{\boldsymbol{a} - (\boldsymbol{a} \cdot \hat{\mathbf{T}})\hat{\mathbf{T}}}{\|\boldsymbol{a} - (\boldsymbol{a} \cdot \hat{\mathbf{T}})\hat{\mathbf{T}}\|} \tag{4.1}$$
$$\hat{\mathbf{B}} = \hat{\mathbf{T}} \times \hat{\mathbf{N}}$$

Figure 4.11 shows the evolution of the debris distance from the breakup location $\rho(t)$, expressed in logarithm to base 10, with each curve coloured according to the projection of the debris ejection velocity $\Delta\boldsymbol{v}$ onto the tangent direction $\hat{\mathbf{T}}$, namely $\Delta v_T = \Delta\boldsymbol{v} \cdot \hat{\mathbf{T}}$.



(a) $\theta = 0$ (b) $\theta = 0.5\pi$

(c) $\theta = \pi$ (d) $\theta = 1.5\pi$

Figure 4.11: Temporal evolution of $\rho(t)$ with a colormap based on $\Delta\boldsymbol{v} \cdot \hat{\mathbf{T}}$.

The breakup events occurring at $\theta = 0$, 0.5π and 1.5π exhibit a similar dynamical behaviour. Fragments with large positive values of Δv_T, shown in yellow, define a first group of curves characterised by a monotonic increase of $\rho(t)$ and by the largest separation distances from the breakup point. For $\theta = 0$ and $\theta = 0.5\pi$, this group is particularly compact, whereas it appears more widely dispersed for $\theta = 1.5\pi$. A second group, falling within the light-green to light-blue colour range, is associated with fragments having Δv_T

close to zero. Some of these fragments also display a monotonic increase of $\rho(t)$, similarly to the previous group. Others remain more closely tied to the motion of the parent trajectory, showing an approximately periodic behaviour in which the fragments return close to the breakup point after each orbital period T. No distinct dynamical region can be identified for fragments with large negative values of Δv_T at these breakup locations.

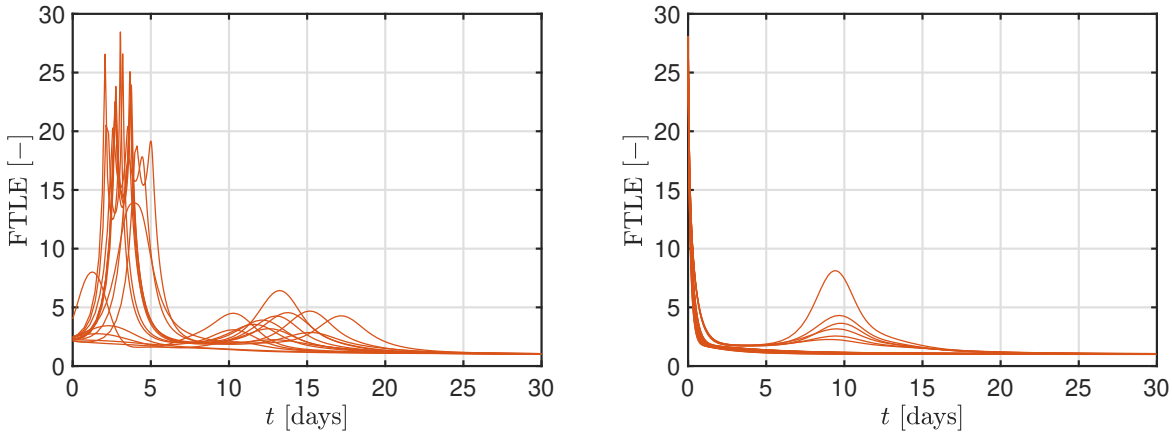
The breakup event occurring at $\theta = \pi$, corresponding to the perilune of the reference NRHO, exhibits a different dynamical behaviour. The two regions identified for the other breakup locations are still present, but they appear more clearly separated. In addition, a third region can be identified for fragments with large negative values of Δv_T. These trajectories, shown in blue, remain approximately confined below 10^4 km and display oscillations on timescales significantly shorter than the orbital period of the reference NRHO. This behaviour may be associated with fragments injected onto tighter lunar orbits. These trajectories may either evolve progressively towards lunar impact or remain in the lunar vicinity for longer times, potentially becoming critical for future missions.

No clear trends or well-defined regions were observed when $\rho(t)$ was coloured according to the projections of the ejection velocity onto the normal and binormal directions, namely $\Delta v_N = \Delta \boldsymbol{v} \cdot \hat{\mathbf{N}}$ and $\Delta v_B = \Delta \boldsymbol{v} \cdot \hat{\mathbf{B}}$. Therefore, the corresponding figures based on the normal and binormal projections are not reported in this work.

4.1.6. FTLE evolution of debris trajectories

This section analyses the temporal evolution of the FTLE along the debris trajectories, with the aim of identifying possible correlations between this dynamical indicator and the final outcome of each debris event. In all the results presented in this section, the FTLE is computed according to the definition given in Sec. 2.6.3, using a finite integration time $t^* = 1$ day. A future sensitivity analysis on t^* could be performed to assess the influence of this parameter on the resulting FTLE trends. The previous analyses showed that the fragments generated at $\theta = 0$, 0.5π and 1.5π follow comparable dynamical trends, whereas the breakup event at $\theta = \pi$ exhibits a distinct behaviour. For this reason, the present analysis is restricted to the short-term evolution associated with $\theta = 0$ and $\theta = \pi$, which correspond to the apolune and perilune regions of the reference NRHO, respectively.

Figure 4.12 shows the temporal evolution of the FTLE for the fragments located outside the Earth–Moon SOI within 1 month. For both the apolune and perilune breakup events, the FTLE progressively converges towards an asymptotic value. This convergence occurs over a relatively short timescale, especially for the breakup at the perilune. In the apolune case, instead, transient oscillations are observed before the FTLE reaches its asymptotic

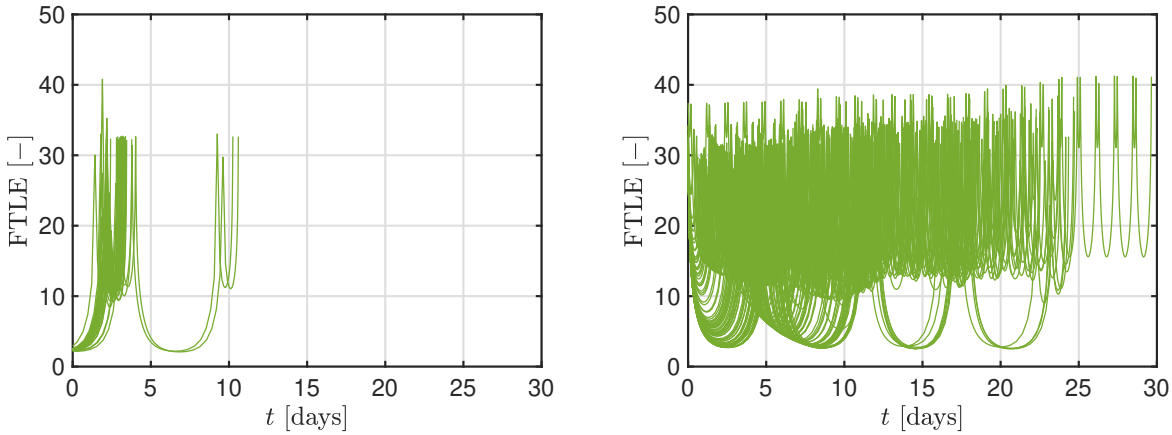


(a) Breakup at apolune ($\theta = 0$). (b) Breakup at perilune ($\theta = \pi$).

Figure 4.12: FTLE evolution for debris exiting the Earth–Moon SOI within 1 month.

behaviour after approximately 20 days. These results are particularly relevant because they show that debris fragments exiting the SOI are associated with a well-defined FTLE trend. Moreover, the convergence towards the asymptotic value occurs before the fragments actually leave the SOI, suggesting that the FTLE may provide an early indication of the subsequent escape behaviour.

Figure 4.13 shows the temporal evolution of the FTLE for the fragments that impact the Moon within 1 month. In contrast to the debris escaping the Earth–Moon SOI, these trajectories do not exhibit convergence towards an asymptotic FTLE value, but they maintain an oscillatory behaviour until impact. For the breakup at apolune, the FTLE

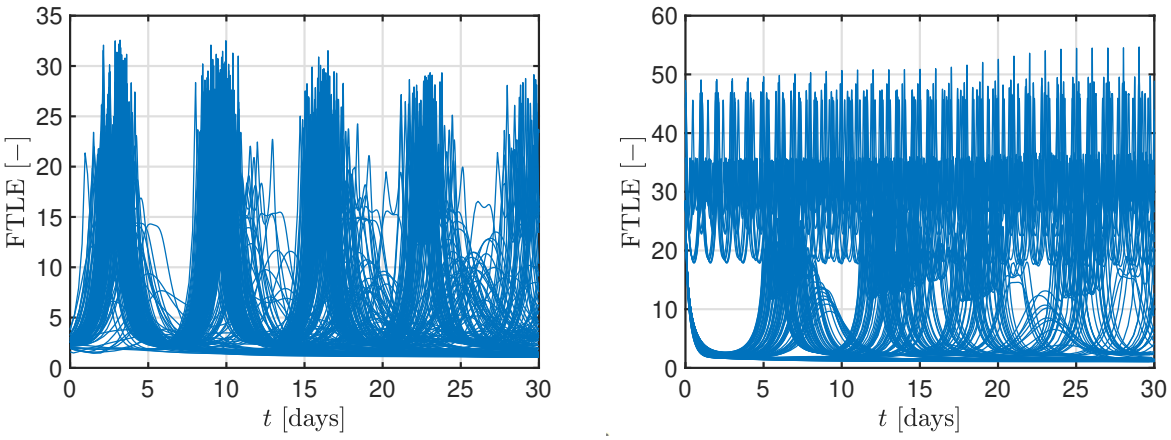


(a) Breakup at apolune ($\theta = 0$). (b) Breakup at perilune ($\theta = \pi$).

Figure 4.13: FTLE evolution for debris impacting the Moon within 1 month.

oscillates periodically between approximately 2.5 [−] and 30 [−]. The corresponding curves terminate after about 12 days, since all lunar impacts occur within this timescale and the propagation of each fragment is stopped at impact. For the breakup at perilune, two distinct groups of trajectories impacting the Moon can be identified, indicating that this final outcome may be reached through different dynamical behaviours. The first group shows a trend comparable to that observed for the apolune breakup, with the FTLE oscillating between approximately 2.5 [−] and 30 [−]. The second group is instead characterised by faster oscillations, with FTLE values mainly bounded between 10 [−] and 40 [−], suggesting a higher level of chaoticity before impact.

Figure 4.14 shows the temporal evolution of the FTLE for the fragments that remain inside the Earth–Moon SOI within 1 month. Although the overall behaviour is more



(a) Breakup at apolune ($\theta = 0$). (b) Breakup at perilune ($\theta = \pi$).

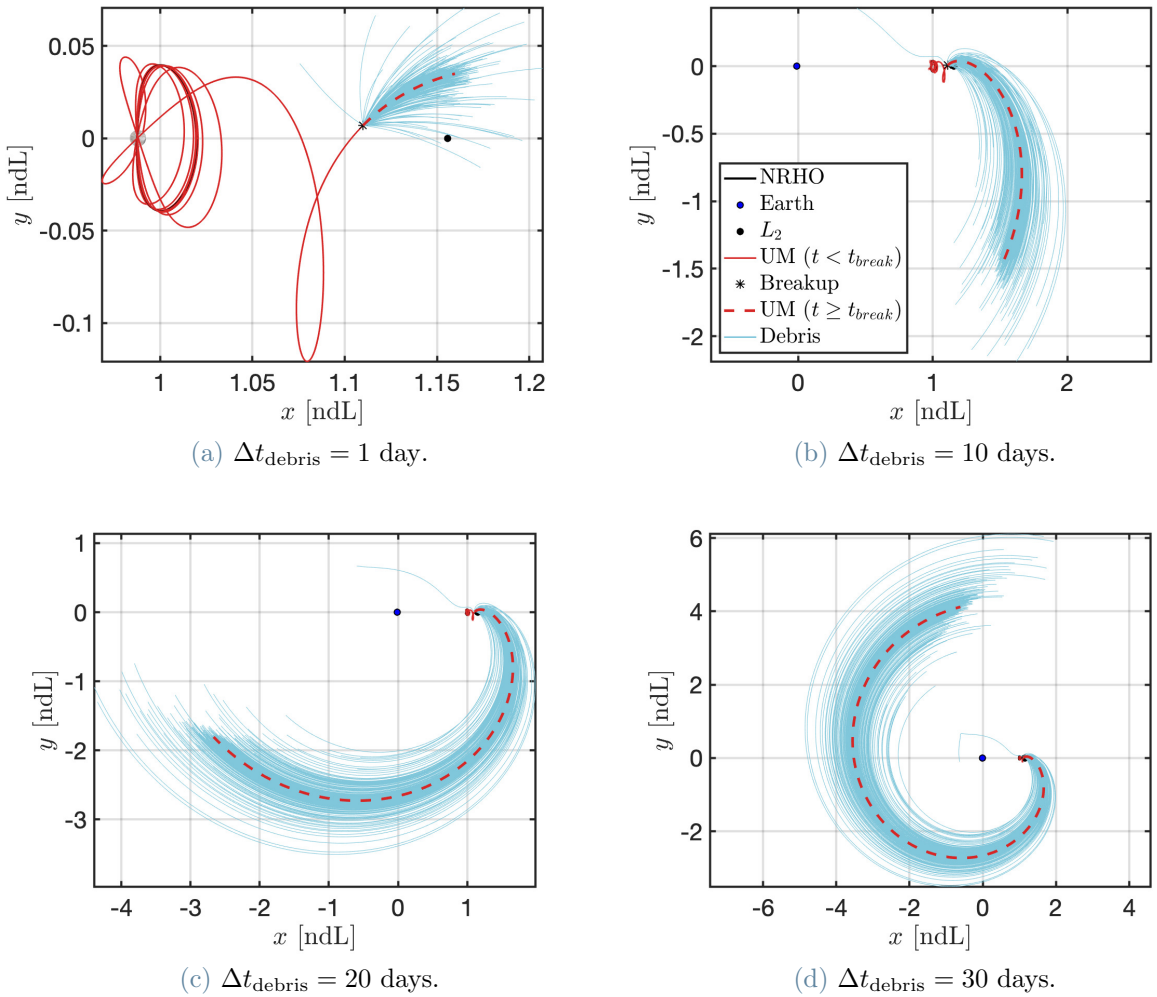
Figure 4.14: FTLE evolution for debris inside the Earth–Moon SOI within 1 month.

irregular than in the previous cases, some patterns can still be identified. For both the apolune and perilune breakup events, a subset of fragments exhibits an FTLE evolution that tends towards an asymptotic value. Based on the behaviour observed for the debris exiting the SOI, these fragments are likely to leave the SOI if propagated over longer timescales. Oscillatory trends are also present, with the main FTLE peaks associated with close approaches to the Moon. These peaks indicate passages through dynamically chaotic regions, where the trajectory is not clearly governed by either the Earth or the Moon. Although this behaviour is consistent with lunar-impact trajectories, it should not be interpreted as a definitive indicator of the final outcome. In fact, some fragments that initially remain inside the SOI may still evolve towards an asymptotic FTLE regime and leave the SOI over longer timescales.

4.2. Breakup events on cislunar disposal trajectories

4.2.1. Debris trajectory evolution

Fragmentation events along relevant cislunar disposal trajectories associated with the unstable manifold of the reference NRHO were simulated following the framework described in Sec. 3.3. Figure 4.15 shows snapshots of the post-breakup evolution for different values of Δt_{debris} in the Earth–Moon rotating frame. The unstable manifold trajectory is shown in red, with a solid line before the breakup event and a dashed line after it. The debris trajectories generated after the breakup are reported in light blue. The breakup location is marked with a black asterisk, while the Earth and L_2 point are represented by blue and black dots, respectively. The Moon is shown using a rendered surface map.



(a) $\Delta t_{\text{debris}} = 1$ day.

(b) $\Delta t_{\text{debris}} = 10$ days.

(c) $\Delta t_{\text{debris}} = 20$ days.

(d) $\Delta t_{\text{debris}} = 30$ days.

Figure 4.15: Debris trajectories after a breakup event along a cislunar disposal trajectory associated with the reference NRHO @ EMB rotating frame ($\theta = 120°$, $t_{\text{break}} = 72$ days).

Since this figure is intended to provide a qualitative visualisation of the debris cloud evolution, a single representative manifold trajectory with $\theta = 120°$ was selected. Similar qualitative features were also observed for the other phase angle values within the selected interval $\theta \in [100°, 120°]$. The breakup epoch was set to $t_{\text{break}} = 72$ days, corresponding to a representative configuration in which the manifold trajectory has already departed from the vicinity of the reference NRHO. In the following sections, more detailed quantitative analyses are performed to assess how the debris cloud transport varies as a function of both the departure phase angle θ and the breakup epoch t_{break}.

The debris cloud appears to follow the dynamical evolution of the unstable manifold, progressively developing around its reference trajectory over the 1 month propagation. This behaviour represents a more favourable condition compared with breakup events occurring along the reference NRHO, where the debris motion was characterised by a markedly more chaotic and nonlinear evolution. In that case, the stronger dispersion of the fragments led to a larger number of lunar impacts and longer residence times within the Earth–Moon SOI. Conversely, the present configuration suggests that a breakup occurring along the unstable manifold may still generate a debris population that remains associated with a natural transport structure departing from the vicinity of the reference NRHO.

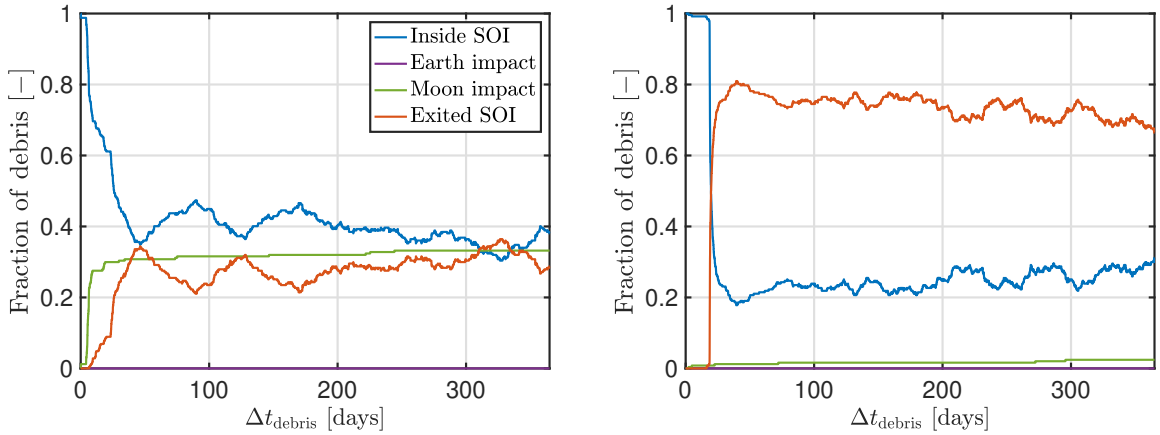
4.2.2. Debris event counters

The evolution of the debris population was analysed using the same debris event counters introduced in Sec. 4.1.2 for the breakup events along the reference NRHO. Since the objective of this analysis is to investigate the dynamical trends of the counters, rather than their specific numerical values, a single manifold trajectory corresponding to $\theta = 120°$ was selected. This choice is justified by the fact that preliminary simulations performed for other trajectories within the target disposal interval $\theta \in [100°, 120°]$ showed similar trends in the considered debris event counters.

Four representative breakup epochs were selected along the manifold trajectory, namely $t_{\text{break}} = 60$, 65, 70 and 75 days. The lower limit $t_{\text{break}} = 60$ days was chosen because at earlier epochs the unstable manifold still closely shadows the reference NRHO. This behaviour follows from the favourable stability properties of NRHOs, which lead to a slow divergence of the associated unstable manifold. As a consequence, choosing a lower value of t_{break} would produce results comparable to those obtained for breakup events occurring directly along the reference NRHO, which are discussed in Sec. 4.1.2. The upper limit, $t_{\text{break}} = 75$ days, was selected as a reference epoch beyond which no significant differences in the trends of the debris event counters were observed. At later epochs, the debris

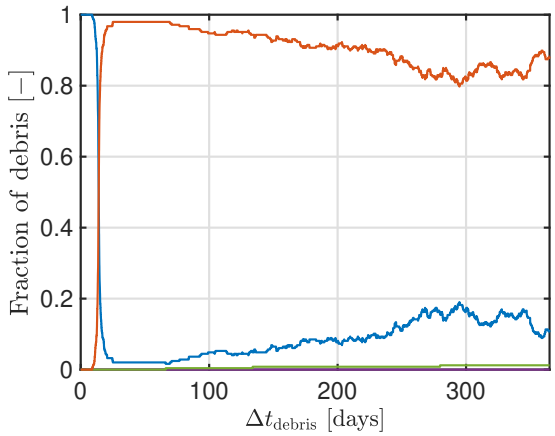
cloud closely follows the unstable manifold itself, leading to a coherent transport of the fragments outside the Earth–Moon SOI. Starting from each breakup epoch, the debris population was propagated for $\Delta t_{\text{debris}} = 1$ year. The same settings and termination conditions adopted for the breakup analysis along the reference NRHO were used, as described in Sec. 4.1.2.

Figure 4.16 shows the temporal evolution of the four debris event counters for the reference case scenario described above. Each panel refers to a fixed breakup epoch and reports the corresponding evolution of N_{SOI}, N_{Moon}, N_{Earth} and N_{exit} over the 1 year propagation interval. The corresponding final values are summarised in Tab. 4.3, where the counters are reported as percentages of the initial debris population.

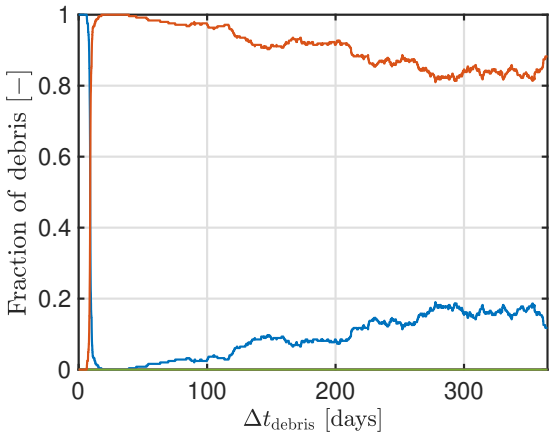


(a) $t_{\text{break}} = 60$ days.

(b) $t_{\text{break}} = 65$ days.



(c) $t_{\text{break}} = 70$ days.



(d) $t_{\text{break}} = 75$ days.

Figure 4.16: Debris event counters along the reference disposal trajectory.

Table 4.3: Debris event counters along the reference disposal trajectory after 1 year.

t_{break}	N_{SOI} [%]	N_{Moon} [%]	N_{Earth} [%]	N_{exit} [%]
60 days	38.1	33.2	0.0	28.7
65 days	31.2	2.4	0.0	66.4
70 days	10.5	1.2	0.0	88.3
75 days	11.7	0.0	0.0	88.3

For the fragmentation at $t_{\text{break}} = 60$ days, the debris event counters exhibit a trend similar to that obtained for the breakup event occurring along the reference NRHO at $\theta = \pi$. This behaviour is consistent with the previous discussion, since at this epoch the unstable manifold has not yet fully departed from the reference NRHO and still evolves in its vicinity before gradually diverging from it. Therefore, the same considerations made in Sec. 4.1.2 for the breakup event near the perilune region can also be extended to this case.

The other three breakup scenarios, namely $t_{\text{break}} = 65$, 70 and 75 days, show similar trends. In all cases, a sharp increase in N_{exit} is observed, indicating that a significant fraction of the debris population leaves the Earth–Moon SOI over a relatively short time interval. This increase occurs earlier for larger values of t_{break}, since the manifold trajectory progressively moves away from the barycentre of the Earth–Moon rotating frame and the breakup occurs closer to the SOI boundary. In addition, the maximum value reached by N_{exit} increases with t_{break}, suggesting that later breakup events generate a larger fraction of fragments that are naturally transported outside the Earth–Moon SOI.

The steep nature of the increase in N_{exit} also confirms the coherent, almost simultaneous evolution of the debris fragments along the unstable manifold. This behaviour differs from that observed for breakup events occurring along the reference NRHO, where the increase in the number of fragments leaving the SOI was more gradual. In that case, the smoother growth of N_{exit} reflected a more heterogeneous dynamical evolution of the debris population, with fragments following more dispersed trajectories.

After the sharp exit phase, N_{SOI} appears to approach an asymptotic value lower than the maximum initially reached. This suggests that, although the debris cloud initially follows the unstable manifold, part of the debris population is still able to re-enter the Earth–Moon SOI at later times. Therefore, an initial departure along the unstable manifold, even when it leads the debris outside the Earth–Moon SOI, is not sufficient to exclude a later natural re-entry. For this reason, heliocentric disposal strategies usually include a second manoeuvre to close the ZVCs and prevent a return to the Earth–Moon region.

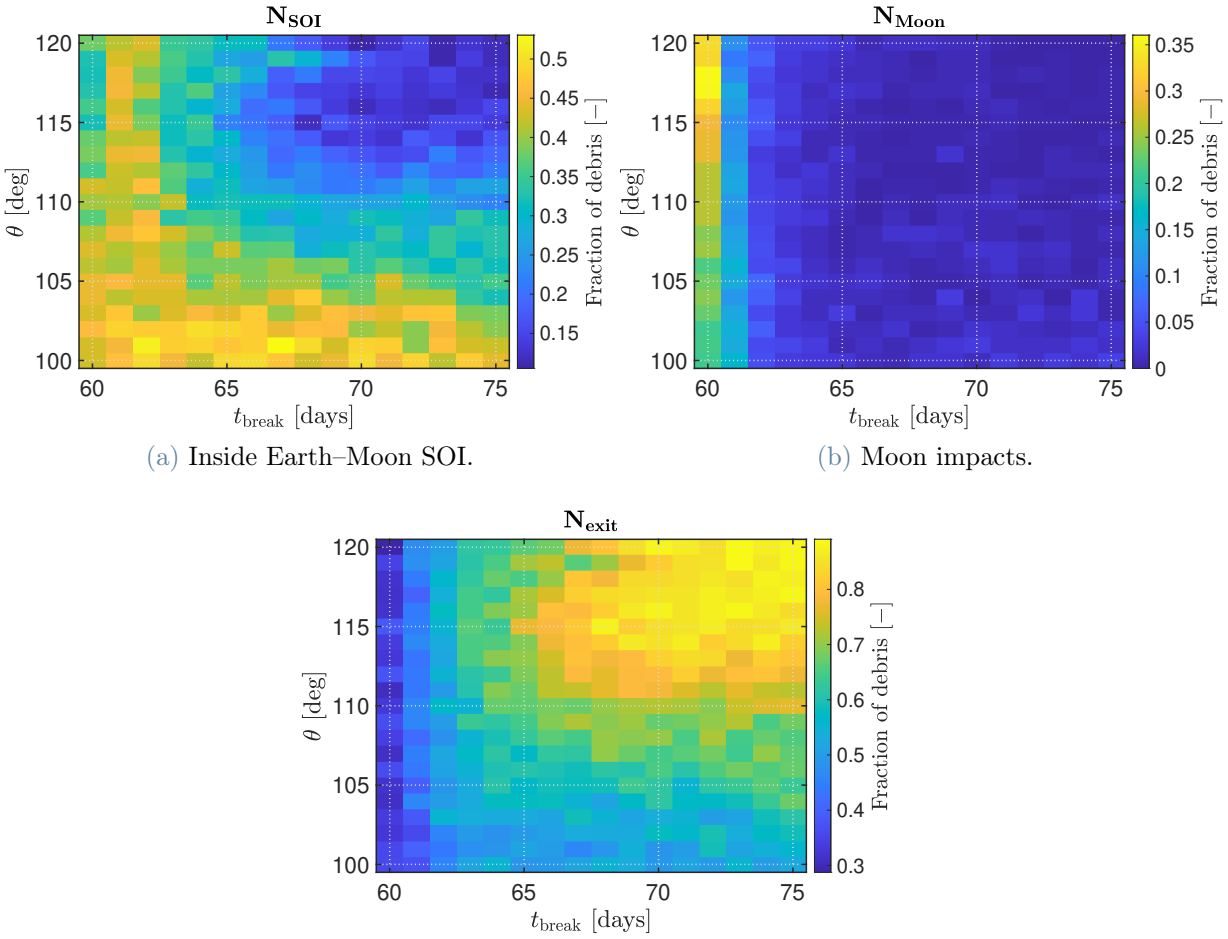
Finally, the results show that lunar impacts are drastically reduced once the disposal trajectory has departed from the vicinity of the NRHO, reaching $N_{\text{Moon}} = 0\%$ for $t_{\text{break}} = 75$ days. Moreover, no impacts with the Earth are recorded for any of the considered breakup epochs. This trend highlights the advantage of performing the disposal manoeuvre along the unstable manifold, as a breakup occurring on these trajectories results in a much lower fraction of lunar impacts than a breakup occurring along the reference NRHO.

4.2.3. Global dependence of debris event counters

The debris event counter analysis was extended to all unstable manifold trajectories departing from the reference NRHO for which successful disposal is feasible, as described in Sec. 3.3. A representative subset of unstable manifold departure points was selected by sampling the target interval $\theta \in [100°, 120°]$ with a resolution of 0.5°. Along each unstable manifold trajectory, the breakup locations were defined by sampling the interval $t_{\text{break}} \in [60, 75]$ days with a resolution of 1 day. The debris population generated at each breakup location was then propagated for $\Delta t_{\text{debris}} = 1$ year using the same simulation setup adopted in the previous section. The results are collected in the two-dimensional maps shown in Fig. 4.17. In these maps, the horizontal axis denotes the breakup epoch t_{break} along each disposal trajectory, the vertical axis denotes the phase angle θ at which the corresponding unstable manifold departs from the reference NRHO, and the colormap indicates the fraction of fragments associated with each debris event counter after 1 year.

The map of N_{Moon} shows that the fraction of lunar impacts decreases significantly over the whole range of θ for $t_{\text{break}} \geq 63$ days. A non-negligible fraction is observed only at the earliest considered breakup time, namely $t_{\text{break}} = 60$ days, with higher values occurring for larger θ. This behaviour is due to the fact that, at this stage of the disposal trajectory, the spacecraft is still close to the reference NRHO. As a result, the debris evolution remains similar to that obtained in Sec. 4.1.2. The increase in lunar impacts near $\theta = 120°$ can be related to the fact that the disposal trajectory is closer to the perilune, which is the region where the NRHO analysis showed the largest values of N_{Moon}.

The map of N_{exit} shows that, for $\theta \in [110°, 120°]$, the fraction of fragments leaving the Earth–Moon SOI increases significantly with t_{break}. A complementary trend is observed in the map of N_{SOI}, where the fraction of debris remaining inside the SOI decreases in the same region. This behaviour is favourable because, as the spacecraft progresses along the disposal trajectories, a potential breakup would generate fewer debris fragments that remain inside the SOI after 1 year. As a result, the potential risk posed to other spacecraft within this region is reduced. The same trend is still present, although less pronounced,



(a) Inside Earth–Moon SOI.

(b) Moon impacts.

(c) Exited Earth–Moon SOI.

Figure 4.17: Global dependence of debris event counters on θ and t_{break}.

for $\theta \in [105°, 110°]$. Conversely, it is not clearly observed for $\theta \in [100°, 105°]$. This last region is therefore less favourable, since delaying the breakup within the considered interval of t_{break} does not lead to a significant reduction in the fraction of debris remaining inside the SOI after 1 year.

Although the selection of the disposal manoeuvre location depends on several factors, such as manoeuvre cost, execution time, and mission constraints, these maps provide an additional tool to support the trade-off. For instance, if the whole interval $\theta \in [100°, 120°]$ were available with similar disposal cost and execution time, the window $\theta \in [110°, 120°]$ would be preferable. In this region, a breakup event would lead to a larger fraction of debris being transported outside the Earth–Moon SOI, reducing the number of fragments that remain in the cislunar environment after 1 year.

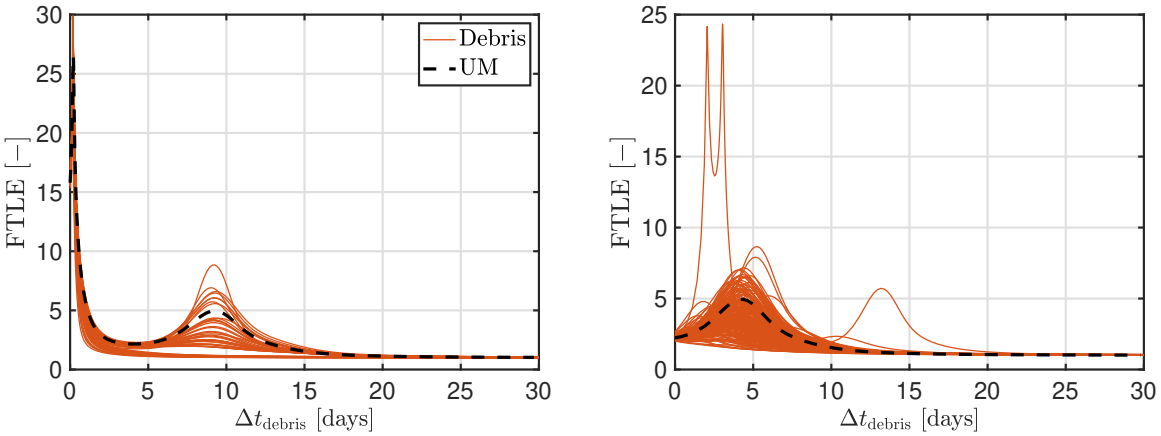
4.2.4. FTLE evolution of debris trajectories

This section extends the FTLE analysis introduced in Sec. 4.1.6 to breakup events occurring along unstable manifold disposal trajectories. The objective is to investigate whether the temporal evolution of the FTLE can be related to the final outcome of the fragments. For consistency with the previous analysis, the FTLE is computed according to the definition given in Sec. 2.6.3, using a finite integration time $t^* = 1$ day. The influence of t^* is not investigated here and is left as a possible future development. The FTLE evolution is analysed over the first month after the breakup, consistently with the reference NRHO case. This interval is sufficient to capture the initial divergence of nearby trajectories and the early transport behaviour induced by the unstable manifold.

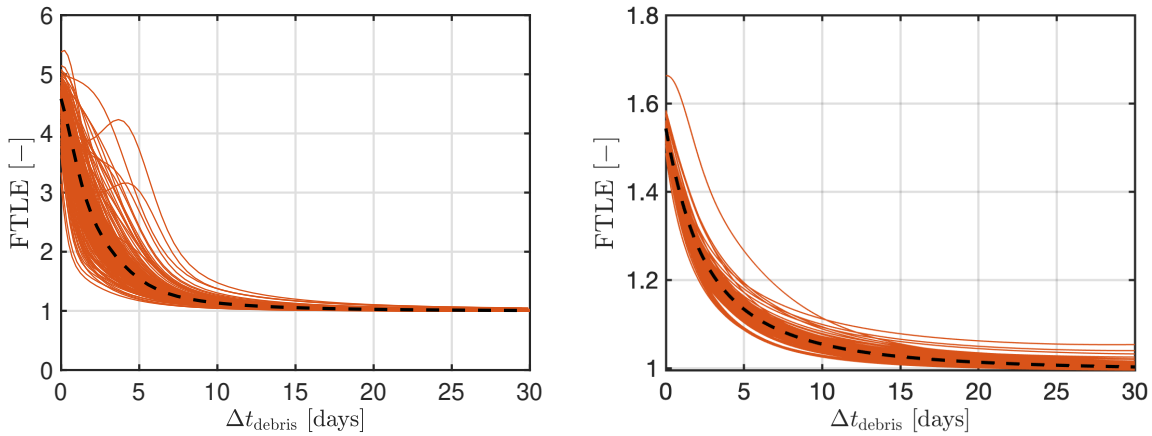
The same representative set adopted in Sec. 4.2.2 for the debris event counter analysis along unstable manifolds is considered. In particular, the analysis is performed on the branch departing from the reference NRHO at $\theta = 120°$, with breakup epochs $t_{\text{break}} = 60$, 65, 70, and 75 days. This choice allows the FTLE evolution to be directly compared with the debris outcomes already obtained for the same cases. Moreover, the purpose of this section is not to reconstruct the full dependence over the disposal window, but to identify the main dynamical trends associated with the different debris outcomes.

Figure 4.18 shows the temporal evolution of the FTLE for fragments located outside the Earth–Moon SOI within 1 month. The orange solid line represents the FTLE evolution of the exiting debris, while the black dashed line shows the FTLE evolution along the unstable manifold disposal trajectory followed by the spacecraft before the breakup. Also in this case, the FTLE exhibits a clear trend. For all the considered values of t_{break}, the debris FTLE progressively converges towards an asymptotic value. This convergence occurs over a relatively short timescale and becomes faster as t_{break} increases. Moreover, larger values of t_{break} are associated with lower initial FTLE values. This suggests that, as the spacecraft evolves along the disposal trajectory, the breakup occurs in progressively less chaotic dynamical regions. It can also be observed that the FTLE evolution of the debris develops around the FTLE curve of the corresponding unstable manifold. This indicates that, after the breakup, the fragments remain dynamically guided by the unstable manifold and continue to follow its transport mechanism.

Figure 4.19 shows the temporal evolution of the FTLE for fragments that impact the Moon within 1 month. The cases corresponding to $t_{\text{break}} = 70$ days and $t_{\text{break}} = 75$ days are not reported, since no lunar impacts are observed for these breakup epochs. In contrast to the debris exiting the SOI, these trajectories do not converge towards an asymptotic FTLE value, but maintain an oscillatory behaviour until impact. For the breakup at

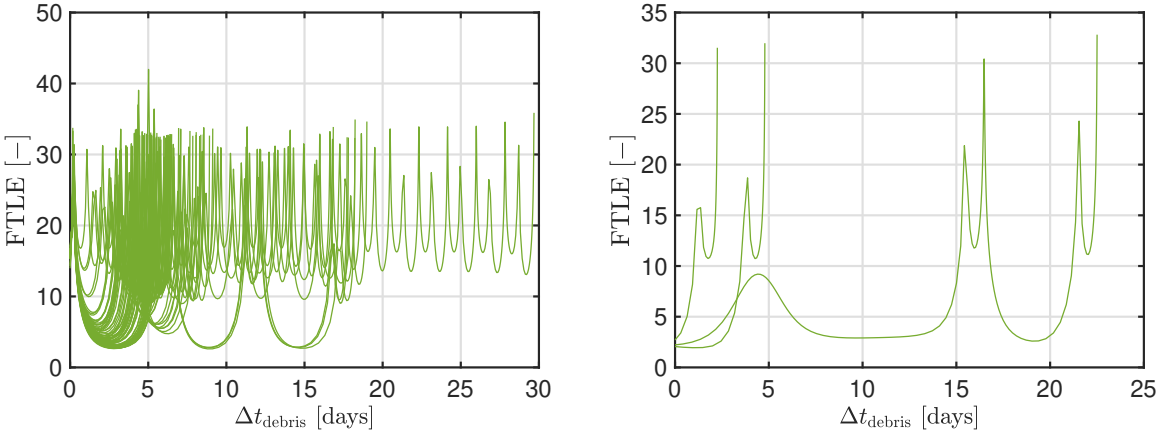


(a) $t_{\text{break}} = 60$ days. (b) $t_{\text{break}} = 65$ days.



(c) $t_{\text{break}} = 70$ days. (d) $t_{\text{break}} = 75$ days.

Figure 4.18: FTLE evolution for debris exiting the Earth–Moon SOI within 1 month.

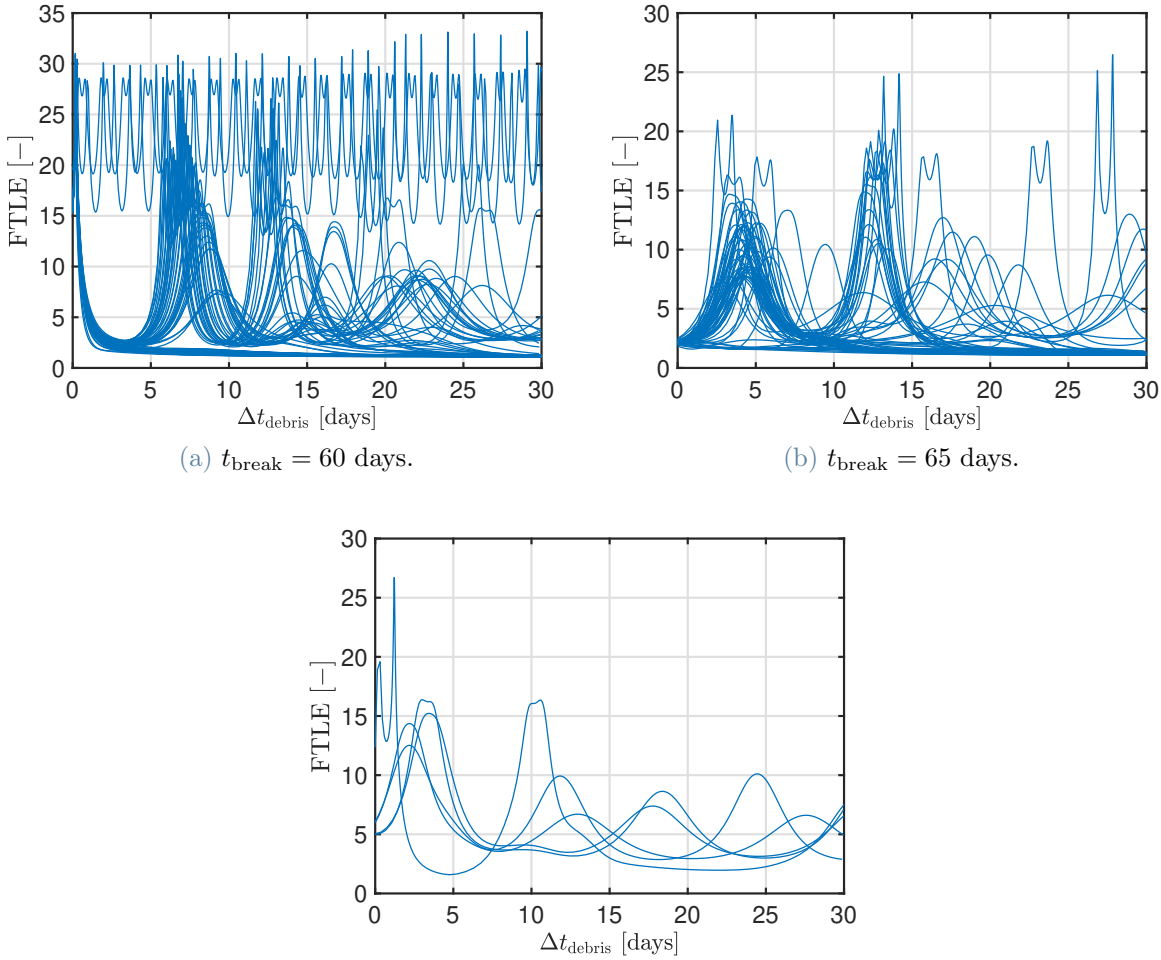


(a) $t_{\text{break}} = 60$ days. (b) $t_{\text{break}} = 65$ days.

Figure 4.19: FTLE evolution for debris impacting the Moon within 1 month.

$t_{\text{break}} = 60$ days, two distinct groups of trajectories can be identified. The first group is characterised by FTLE values oscillating approximately between 2.5 [−] and 30 [−], while the second group exhibits faster oscillations, mainly bounded between 10 [−] and 40 [−]. This behaviour is analogous to that observed for the breakup event at $\theta = \pi$ along the reference NRHO. This is consistent with the fact that, at $t_{\text{break}} = 60$ days, the unstable manifold trajectory is still close to the perilune region. For the breakup at $t_{\text{break}} = 65$ days no clear trend can be identified, as only a small number of trajectories impact the Moon.

Finally, Fig. 4.20 shows the temporal evolution of the FTLE for fragments that remain inside the SOI within 1 month. The case corresponding to $t_{\text{break}} = 75$ days is not reported, since no fragments remaining inside the SOI are observed within the considered 1 month propagation window. For $t_{\text{break}} = 60$ days, a subset of trajectories shows a pro-



(a) $t_{\text{break}} = 60$ days.

(b) $t_{\text{break}} = 65$ days.

(c) $t_{\text{break}} = 70$ days.

Figure 4.20: FTLE evolution for debris inside the Earth–Moon SOI within 1 month.

gressive convergence of the FTLE towards an asymptotic value. As previously observed, this behaviour suggests that these fragments would likely leave the Earth–Moon SOI if propagated over a longer time window. A second group is characterised by fast FTLE oscillations, with a dynamical behaviour similar to that obtained for debris impacting the Moon. A third group exhibits a more irregular and chaotic evolution, likely associated with fragments travelling through different regions of the SOI where the trajectory is not clearly governed by either the Earth or the Moon. Based on the present propagation window, it is not possible to determine whether this latter group would eventually lead to a SOI exit or a lunar impact. A similar behaviour is observed for $t_{\text{break}} = 65$ days, except for the fast oscillatory band associated with lunar impact trajectories. Finally, for $t_{\text{break}} = 70$ days, the debris fragments also exhibit a chaotic FTLE evolution. However, no clear trend can be identified in this case, due to the small number of trajectories that remain inside the Earth–Moon SOI.

5 | Conclusions

5.1. Summary and contributions

This thesis analysed the dynamical evolution of debris clouds generated by fragmentation events in the Earth–Moon environment. The study focused on breakup events occurring along a reference southern Earth–Moon L_2 NRHO, along the corresponding family of Halo orbits and along relevant cislunar disposal trajectories. The main objective was to understand how the breakup location, the parent trajectory and the underlying dynamical structures influence the evolution of the resulting fragments.

The breakup event was modelled using the NASA SBM, assuming a spacecraft explosion as the reference scenario. The fragments were propagated in the CR3BP, which captures the main nonlinear dynamical features of the Earth–Moon system with a computational cost suitable for large parametric analyses. The methods employed to characterise debris evolution include trajectory analyses, debris outcome maps, post-breakup Jacobi constant distributions, dynamical metrics and the temporal evolution of the FTLE.

The analysis along the reference NRHO showed that the debris evolution is strongly governed by the breakup phase angle. Lunar impacts were mainly concentrated around the perilune region, while other breakup locations produced a higher fraction of debris remaining inside or escaping the Earth–Moon SOI. Since SOI exits were not treated as terminal events, possible re-entries were also captured in the analysis, showing that fragments may return to the cislunar region after crossing the SOI boundary.

The extension to the southern Earth–Moon L_2 Halo family showed that the final debris distribution depends on both the breakup phase angle and the stability properties of the parent orbit. The largest fractions of lunar impacts were found mainly for $\theta \in [230°, 270°]$, rather than near $\theta = 180°$ as in the reference NRHO. The highest values of N_{exit} were instead obtained close to $\theta = 0°$, with this region becoming wider for larger values of SI and progressively shrinking as SI decreases. The maps also showed a clear lack of symmetry between the two halves of the Halo orbits, indicating that debris transport also depends on the direction of motion of the parent spacecraft before fragmentation.

Breakup events along the cislunar disposal trajectories exhibited a more coherent debris evolution. Once the trajectory had departed from the vicinity of the reference NRHO, the debris cloud tended to follow the unstable manifold dynamics and was naturally transported away from the cislunar region. The debris event counter analysis showed that later breakup epochs along the disposal trajectory led to a larger fraction of fragments exiting the Earth–Moon SOI and to a strong reduction in lunar impacts. The global maps over the selected disposal window indicated that the interval $\theta \in [110°, 120°]$ is more favourable from a debris mitigation perspective, since a breakup in this region would leave fewer fragments inside the SOI after 1 year.

Finally, the FTLE analysis provided a dynamical interpretation of the observed debris outcomes. Fragments exiting the Earth–Moon SOI generally showed a progressive convergence of the FTLE towards an asymptotic value, often before the actual SOI exit occurred. Conversely, fragments impacting the Moon were characterised by oscillatory FTLE trends. Debris remaining inside the SOI exhibited mixed behaviours, suggesting that some of these fragments may eventually evolve towards escape or lunar impact over longer propagation times.

5.2. Future developments

This thesis contributed to a deeper understanding of the dynamical mechanisms governing debris transport in the cislunar environment. The work presented here can be extended in several directions, both from a methodological perspective and in terms of the breakup scenarios considered. The main possible future developments are summarised below.

- **Extension to collision scenarios.** This thesis considered a spacecraft explosion as the reference breakup scenario. This choice was motivated by the current state of the cislunar environment, which is still sparsely populated compared to near-Earth space. Therefore, in the early stages of cislunar traffic growth, explosions may represent a plausible source of the first artificial debris populations. However, as the number of spacecraft increases, collision events will become progressively more relevant. Future work could extend the breakup modelling to catastrophic and non-catastrophic collisions, assessing the effect of different fragment distributions.
- **Use of higher-fidelity dynamical models.** The CR3BP provided a suitable first framework to investigate the main nonlinear transport mechanisms of the Earth–Moon system. Future analyses could adopt higher-fidelity dynamical models to quantify the robustness of the observed trends. Possible extensions include the coupled Sun–Earth and Earth–Moon CR3BP, the BCR4BP and ephemeris models.

- **Longer propagation windows and denser sampling.** From a numerical perspective, the propagation time could be extended beyond the intervals adopted in this work. This would allow a better characterisation of the long-term evolution of the debris population in the cislunar environment. In addition, the sampling of the Halo family and of the cislunar disposal trajectories could be made denser, both in terms of breakup phase angle and selected parent orbits. These improvements would increase the resolution of the debris event counter maps, but would also lead to a significant increase in computational cost. For this reason, GPU parallelisation or high-performance computing resources would be required.
- **Extension to other cislunar orbit families.** The same methodology could be applied to other relevant cislunar orbital regimes, such as Lyapunov orbits, vertical orbits and DROs. This would provide a more complete overview of the fragmentation hazard across the cislunar environment and would allow different candidate operational or disposal regions to be compared from a debris mitigation perspective. A separate extension could also address LLOs. In this case, the dynamical model should be refined to include the higher-order harmonics of the lunar gravity field, whose effects become relevant at low altitudes around the Moon.
- **Application to cislunar SSA and mission design.** Finally, the dynamical analysis of debris transport developed in this thesis could support the design of future SSA systems for the cislunar environment. Debris outcome maps, FTLE trends and transport pathways could be used to identify regions where fragments are more likely to accumulate, escape, or impact the Earth and the Moon. This information may help define observation priorities, sensor placement strategies and safer operational or disposal trajectories for future cislunar missions.

Bibliography

[1] M. J. Holzinger, C. C. Chow, and P. Garretson. A Primer on Cislunar Space. Air Force Research Laboratory, OH, USA, 2021.

[2] S. Kaplan. Eyes on the Prize: The Strategic Implications of Cislunar Space and the Moon. Center for Strategic and International Studies (CSIS), 2020.

[3] K. Johnson. Fly Me to the Moon: Worldwide Cislunar and Lunar Missions. Center for Strategic and International Studies (CSIS), 2022.

[4] NASA. Artemis. `https://www.nasa.gov/humans-in-space/artemis/`, 2026. Accessed: 15 May 2026.

[5] NASA. Lunar Science Priorities. `https://science.nasa.gov/lunar-science/priorities/`, 2026. Accessed: 15 May 2026.

[6] S. K. Borowski, S. W. Ryan, D. R. McCurdy, and B. G. Sauls. Commercial and Human Settlement of the Moon and Cislunar Space – A Look Ahead at the Possibilities over the Next 50 Years. In *AIAA Propulsion and Energy Forum*, IN, USA, 2019. doi: 10.2514/6.2019-3971.

[7] NASA. Overview: In-Situ Resource Utilization. `https://www.nasa.gov/overview-in-situ-resource-utilization/`, 2023. Accessed: 15 May 2026.

[8] P. M. Cunio, M. Bever, C. Ingram, B. R. Flewelling, and G. McNeill. Utilization Potential for Distinct Orbit Families in the Cislunar Domain. In *2021 Advanced Maui Optical and Space Surveillance Technologies Conference (AMOS)*, HI, USA, 2021.

[9] ESA Space Debris Office. ESA's Annual Space Environment Report. European Space Agency. `https://www.sdo.esoc.esa.int/environment_report/Space_Environment_Report_latest.pdf`, 2026. Accessed: 17 May 2026.

[10] ESA Space Debris Mitigation Working Group. ESA Space Debris Mitigation Requirements. European Space Agency. `https://technology.esa.int/upload/media/ESA-Space-Debris-Mitigation-Requirements-ESSB-ST-U-007-Issue1.pdf`, 2023. Accessed: 17 May 2026.

[11] ESB Secretariat. ESA Space Debris Mitigation Compliance Verification Guidelines. European Space Agency. https://sdup.esoc.esa.int/documents/download/ESA_Space_Debris_Mitigation_Compliance_Verification_Guidelines.pdf, 2025. Accessed: 17 May 2026.

[12] Inter-Agency Space Debris Coordination Committee. IADC Space Debris Mitigation Guidelines. https://www.unoosa.org/res/oosadoc/data/documents/2025/aac_105c_12025crp/aac_105c_12025crp_9_0_html/AC105_C1_2025_CRP09E.pdf, 2025. Accessed: 17 May 2026.

[13] N. L. Johnson, P. H. Krisko, J.-C. Liou, and P. D. Anz-Meador. NASA's New Breakup Model of EVOLVE 4.0. *Advances in Space Research*, 28(9):1377–1384, 2001. doi: 10.1016/S0273-1177(01)00423-9.

[14] P. H. Krisko. Proper Implementation of the 1998 NASA Breakup Model. *Orbital Debris Quarterly News*, 15(4):4–5, 2011.

[15] F. Letizia, C. Colombo, H. G. Lewis, and C. R. McInnes. Space Debris Cloud Evolution in Low Earth Orbit. In *64th International Astronautical Congress (IAC)*, Beijing, China, 2013.

[16] F. Letizia. *Space Debris Cloud Evolution in Low Earth Orbit*. PhD thesis, University of Southampton, Southampton, United Kingdom, 2016.

[17] L. Giudici. *Space Debris Environment Analysis with Continuum Mechanics*. PhD thesis, Politecnico di Milano, Milan, Italy, 2024.

[18] S. Frey, C. Colombo, S. Lemmens, and H. Krag. Evolution of Fragmentation Cloud in Highly Eccentric Orbit using Representative Objects. In *68th International Astronautical Congress (IAC)*, Adelaide, Australia, 2017.

[19] S. Frey, C. Colombo, and S. Lemmens. Evolution of Fragmentation Cloud in Highly Eccentric Earth Orbits through Continuum Modelling. In *69th International Astronautical Congress (IAC)*, Bremen, Germany, 2018.

[20] S. Piani. Analytical Model for Propagation of Debris Clouds in Geostationary Orbit. Master's thesis, Politecnico di Milano, Milan, Italy, 2022. Master in Space Engineering, Supervisor: C. Colombo, Co-supervisor: A. Muciaccia.

[21] S. J. Frey. *Evolution and Hazard Analysis of Orbital Fragmentation Continua*. PhD thesis, Politecnico di Milano, Milan, Italy, 2020.

[22] M. Romano, A. Muciaccia, M. Trisolini, P. Di Lizia, C. Colombo, A. Di Cecco, and

L. Salotti. PUZZLE Software for the Characterisation of In-Orbit Fragmentations. In *8th European Conference on Space Debris*, Darmstadt, Germany, 2021.

[23] A. Muciaccia, M. Romano, and C. Colombo. Detection and Characterisation of In-Orbit Fragmentations over Short and Long Periods of Time. In *72nd International Astronautical Congress (IAC)*, Dubai, UAE, 2021.

[24] M. F. Montaruli, P. Di Lizia, E. Cordelli, H. Ma, and J. Siminski. A Stochastic Approach to Detect Fragmentation Epoch from a Single Fragment Orbit Determination. *Advances in Space Research*, 72(9):3713–3733, 2023. doi: 10.1016/j.asr.2023.08.031.

[25] A. Muciaccia, M. Romano, M. Trisolini, and C. Colombo. Reconstruction of In-Orbit Breakup Events over the Long Term. *Acta Astronautica*, 228:875–885, 2025. doi: 10.1016/j.actaastro.2024.12.053.

[26] F. Ottoboni, A. Muciaccia, L. Giudici, and C. Colombo. Short-Term Reconstruction of Fragmentation Events in Low Earth Orbit Using Uncertainty Propagation. In *75th International Astronautical Congress (IAC)*, Milan, Italy, 2024.

[27] F. Ottoboni, A. Muciaccia, and C. Colombo. Reconstruction of In-Orbit Breakup Events over the Short Term. *Acta Astronautica*, 243:326–337, 2026. doi: 10.1016/j.actaastro.2026.01.061.

[28] F. Ottoboni, C. Colombo, P. Grattagliano, A. Mignocchi, J. L. Gonzalo, A. Muciaccia, M. F. Montaruli, M. Maestrini, P. Di Lizia, L. Dimare, S. Cicalò, F. Guerra, F. Delfino, A. Rossi, X. Yan, M. Miklewski, F. J. Simarro Mecinas, L. Gisolfi, A. Horstmann, and T. Flohrer. Characterisation of Fragmentation Clouds and Fragmentation Event Reconstruction for Space Break-Up Forensics. In *9th European Conference on Space Debris*, Bonn, Germany, 2025.

[29] P. Grattagliano, F. Ottoboni, A. Muciaccia, M. F. Montaruli, P. Di Lizia, and C. Colombo. Robust Short-Term Reconstruction of In-Orbit Fragmentation Events. In *11th European Conference for Aeronautics and Aerospace Sciences (EUCASS)*, 2025.

[30] N. R. Boone and R. A. Bettinger. Artificial Debris Collision Risk Following a Catastrophic Spacecraft Mishap in Lunar Orbit. In *2021 Advanced Maui Optical Surveillance Conference (AMOS)*, HI, USA, 2021.

[31] N. R. Boone and R. A. Bettinger. Long-Term Evolution of Debris Clouds in Low Lunar Orbit. In *2022 Advanced Maui Optical Surveillance Conference (AMOS)*, HI, USA, 2022.

[32] N. R. Boone and R. A. Bettinger. Simulation of Debris Events in Selected Low Lunar Orbits. *The Journal of the Astronautical Sciences*, 70(16):1–24, 2023. doi: 10.1007/s40295-023-00382-y.

[33] N. R. Boone and R. A. Bettinger. Monte Carlo Simulation of Spacecraft Breakup Events in Low Lunar Orbit. *Advances in Space Research*, 73(12):6125–6139, 2024. doi: 10.1016/j.asr.2024.03.005.

[34] N. R. Boone and R. A. Bettinger. Debris Propagation Following a Spacecraft Mishap at the Collinear Earth–Moon Lagrange Points. In *2021 IEEE Aerospace Conference*, Big Sky, MT, USA, 2021. doi: 10.1109/AERO50100.2021.9438276.

[35] N. R. Boone and R. A. Bettinger. Spacecraft Survivability in the Natural Debris Environment Near the Stable Earth–Moon Lagrange Points. *Advances in Space Research*, 67(8):2319–2332, 2021. doi: 10.1016/j.asr.2021.01.047.

[36] N. R. Boone and R. A. Bettinger. Cislunar Debris Propagation Following a Catastrophic Spacecraft Mishap. In *AIAA SciTech 2021 Forum*, Virtual Event, 2021. doi: 10.2514/6.2021-0102.

[37] N. R. Boone and R. A. Bettinger. Debris Collision Risk Analysis Following Simulated Cislunar Spacecraft Explosions. *Journal of Spacecraft and Rockets*, 60(2):668–684, 2023. doi: 10.2514/1.A35353.

[38] N. R. Boone, R. A. Bettinger, and B. D. Little. Risks From Spacecraft Breakup Events in Near Rectilinear Halo Orbits. In *2023 Advanced Maui Optical Surveillance Conference (AMOS)*, HI, USA, 2023.

[39] N. R. Boone, R. A. Bettinger, and B. D. Little. Simulation of Debris Events in Cislunar Orbits Near the Moon. *Journal of Spacecraft and Rockets*, 62(6):2030–2046, 2025. doi: 10.2514/1.A36072.

[40] A. P. Wilmer, N. R. Boone, and R. A. Bettinger. Artificial Debris Propagation in Cislunar Periodic Orbits. In *2021 AAS/AIAA Astrodynamics Specialist Conference*, 2021.

[41] A. P. Wilmer, N. R. Boone, and R. A. Bettinger. Debris Propagation and Spacecraft Survivability Assessment for Catastrophic Mishaps Occurring in Cislunar Periodic Orbits. *Journal of Space Safety Engineering*, 9(2):207–222, 2022. doi: 10.1016/j.jsse.2022.02.007.

[42] C. J. Wetterer, C. Craft, J. Baldwin, M. Dilley, P. Billings, J. Gaebler, and J. Bruer.

Cislunar Debris from Halo Object Breakups. In *2023 Advanced Maui Optical Surveillance Conference (AMOS)*, HI, USA, 2023.

[43] P. Guardabasso, S. Lizy-Destrez, and M. Ansart. Lunar Orbital Debris Mitigation: Characterisation of the Environment and Identification of Disposal Strategies. In *8th European Conference on Space Debris*, Darmstadt, Germany, 2021.

[44] P. Guardabasso, D. K. Skoulidou, L. Bucci, F. Letizia, S. Lemmens, and S. Lizy-Destrez. Cislunar Debris Mitigation: Development of a Methodology to Assess the Sustainability of Lunar Missions. In *72nd International Astronautical Congress (IAC)*, Dubai, UAE, 2021.

[45] P. Guardabasso, L. Bucci, D. K. Skoulidou, F. Letizia, and S. Lizy-Destrez. Massive GPU Parallelisation for Cislunar Debris Mitigation Analyses. In *73rd International Astronautical Congress (IAC)*, Paris, France, 2022.

[46] P. Guardabasso, D. K. Skoulidou, L. Bucci, F. Letizia, S. Lemmens, M. Ansart, X. Roser, S. Lizy-Destrez, and G. Casalis. Analysis of Accidental Spacecraft Breakup Events in Cislunar Space. *Advances in Space Research*, 72(5):1550–1569, 2023. doi: 10.1016/j.asr.2023.05.004.

[47] A. Black and C. Frueh. Characterizing Cislunar Fragmentations. In *2023 Advanced Maui Optical and Space Surveillance Technologies Conference (AMOS)*, HI, USA, 2023.

[48] A. Black and C. Frueh. Fragmentation Characterization in the Circular Restricted Three Body Problem for Cislunar Space Domain Awareness. *Advances in Space Research*, 75(1):1177–1204, 2025. doi: 10.1016/j.asr.2024.08.076.

[49] A. Black. *Decluttering the Cosmos: Characterizing Fragmentation Behaviour in Cislunar and Near Earth Environments for Space Domain Awareness*. PhD thesis, Purdue University, West Lafayette, Indiana, USA, 2024.

[50] M. Bolis, E. M. Alessi, and C. Colombo. Long-Term Evolution of Orbits in Cislunar Space: Characterisation and Stability Analysis. In *75th International Astronautical Congress (IAC)*, Milan, Italy, 2024.

[51] M. Bolis, E. M. Alessi, and C. Colombo. End-of-Life Disposal Parametric Analysis in Cislunar Space: Earth–Moon L2 Escape No-Return Trajectories. In *9th European Conference on Space Debris*, Bonn, Germany, 2025.

[52] M. Bolis, E. M. Alessi, and C. Colombo. End-of-Life Disposal Design for Near-

Rectilinear Halo Orbits. In *76th International Astronautical Congress (IAC)*, Sydney, Australia, 2025.

[53] R. L. Kling. Postmortem of a Hypervelocity Impact: Summary. Technical Report CS86-LKD-001, Teledyne Brown Engineering, 1986.

[54] N. L. Johnson. The Collision of Satellites 16937 and 16938: A Preliminary Report. Technical Report CS87-LKD-002, Teledyne Brown Engineering, 1986.

[55] R. L. Kling. The Collision of Satellites 16937 and 16938: Debris Characterization. Technical Report CS87-LKD-005, Teledyne Brown Engineering, 1987.

[56] D. S. McKnight, N. L. Johnson, M. L. Fudge, and T. D. Maclay. Satellite Orbital Debris Characterization Impact Test (SOCIT) Series Data Collection Report. Technical report, Kaman Sciences Corporation, April 1995.

[57] W. Fucke and H. Sdunnus. Population Model of Small Size Space Debris, Final Report. Technical Report BF-R 67.698-5, Battelle-Institut e.V., June 1993.

[58] R. C. Reynolds, A. Bade, P. Eichler, A. A. Jackson, P. H. Krisko, M. Matney, D. J. Kessler, and P. D. Anz-Meador. NASA Standard Breakup Model 1998 Revision. Technical Report LMSMSS-32532, Lockheed Martin Space Mission Systems and Services, September 1998.

[59] S. Frey and C. Colombo. Transformation of Satellite Breakup Distribution for Probabilistic Orbital Collision Hazard Analysis. *Journal of Guidance, Control, and Dynamics*, 44(1):88–105, 2021. doi: 10.2514/1.G004939.

[60] V. Szebehely. *Theory of Orbits: The Restricted Problem of Three Bodies*. Academic Press, 1 edition, 1967.

[61] W. S. Koon, M. W. Lo, J. E. Marsden, and S. D. Ross. *Dynamical Systems, the Three-Body Problem and Space Mission Design*. Marsden Books, 2011.

[62] NASA Jet Propulsion Laboratory. Planetary Satellite Mean Elements. `https://ssd.jpl.nasa.gov/sats/elem/`, 2026. Accessed: 8 May 2026.

[63] G. Gómez, J. Llibre, R. Martínez, and C. Simó. *Dynamics and Mission Design Near Libration Points, Vol. I: Fundamentals, The Case of Collinear Libration Points*. World Scientific, Singapore, 2001. doi: 10.1142/4402.

[64] G. Gómez, J. Llibre, R. Martínez, and C. Simó. *Dynamics and Mission Design Near Libration Points, Vol. II: Fundamentals, The Case of Triangular Libration Points*. World Scientific, Singapore, 2001. doi: 10.1142/4392.

[65] K. K. Boudad. Disposal Dynamics from the Vicinity of Near Rectilinear Halo Orbits in the Earth–Moon–Sun System. Master's thesis, Purdue University, West Lafayette, Indiana, USA, 2018.

[66] B. D. Tapley, B. E. Schutz, and G. H. Born. *Statistical Orbit Determination*. Elsevier, 1 edition, 2004.

[67] P. Di Lizia and F. Topputo. Spacecraft Guidance and Navigation. Lecture notes, Politecnico di Milano, Milan, Italy, 2024.

[68] E. J. Doedel, V. A. Romanov, R. C. Paffenroth, H. B. Keller, D. J. Dichmann, J. Galán-Vioque, and A. Vanderbauwhede. Elemental Periodic Orbits Associated with the Libration Points in the Circular Restricted 3-Body Problem. *International Journal of Bifurcation and Chaos*, 17(8):2625–2677, 2007. doi: 10.1142/S0218127407018671.

[69] M. Hénon. *Generating Families in the Restricted Three-Body Problem, II. Quantitative Study of Bifurcations*. Springer Berlin, Heidelberg, 2003. doi: 10.1007/3-540-44712-1.

[70] J. S. Parker and R. L. Anderson. *Low-Energy Lunar Trajectory Design*. Jet Propulsion Laboratory, Pasadena, CA, USA, 2013.

[71] R. W. Farquhar. *The Control and Use of Libration-Point Satellites*. PhD thesis, Stanford University, Stanford, CA, USA, 1968.

[72] J. V. Breakwell and J. V. Brown. The 'Halo' Family of 3-Dimensional Periodic Orbits in the Earth–Moon Restricted 3-Body Problem. *Celestial Mechanics*, 20:389–404, 1979. doi: 10.1007/BF01230405.

[73] K. C. Howell. Three-dimensional, Periodic 'Halo' Orbits. *Celestial Mechanics*, 32: 53–71, 1984. doi: 10.1007/BF01358403.

[74] K. C. Howell and J. V. Breakwell. Almost Rectilinear Halo Orbits. *Celestial Mechanics*, 32:29–52, 1984. doi: 10.1007/BF01358402.

[75] D. Guzzetti, E. M. Zimovan, K. C. Howell, and D. C. Davis. Stationkeeping Analysis for Spacecraft in Lunar Near Rectilinear Halo Orbits. In *27th AAS/AIAA Spaceflight Mechanics Meeting*, San Antonio, TX, USA, 2017.

[76] D. C. Davis, S. A. Bhatt, K. C. Howell, J.-W. Jang, R. L. Whitley, F. D. Clark, D. Guzzetti, E. M. Zimovan, and G. H. Barton. Orbit Maintenance and Navigation

of Human Spacecraft at Cislunar Near Rectilinear Halo Orbits. In *27th AAS/AIAA Spaceflight Mechanics Meeting*, San Antonio, TX, USA, 2017.

[77] E. M. Zimovan, K. C. Howell, and D. C. Davis. Near Rectilinear Halo Orbits and Their Application in Cis-Lunar Space. In *3rd International Academy of Astronautics Conference on Dynamics and Control of Space Systems*, Moscow, Russia, 2017.

[78] E. M. Zimovan-Spreen, K. C. Howell, and D. C. Davis. Eclipse Avoidance in Dynamical Structures Nearby NRHOs in a Higher-Fidelity Model. In *AAS/AIAA Astrodynamics Specialist Conference*, Lake Tahoe, CA, USA, 2020.

[79] D. E. Lee. White Paper: Gateway Destination Orbit Model: A Continuous 15 Year NRHO Reference Trajectory. Technical Report JSC-E-DAA-TN72594, NASA Johnson Space Center Houston, TX, USA, 2019.

[80] D. J. Grebow. Generating Periodic Orbits in the Circular Restricted Three-Body Problem with Applications to Lunar South Pole Coverage. Master's thesis, Purdue University, West Lafayette, Indiana, USA, 2006.

[81] T. S. Parker and L. Chua. *Practical Numerical Algorithms for Chaotic Systems*. Springer Science & Business Media, 1989. doi: 10.1007/978-1-4612-3486-9.

[82] G. Gómez, W. S. Koon, M. W. Lo, J. E. Marsden, J. Masdemont, and S. D. Ross. Connecting Orbits and Invariant Manifolds in the Spatial Restricted Three-Body Problem. *Nonlinearity*, 17(5):1571–1606, 2004. doi: 10.1088/0951-7715/17/5/002.

[83] Z. P. Olikara, G. Gómez, and J. J. Masdemont. Dynamic Mechanisms for Spacecraft Disposal from Sun–Earth Libration Points. *Journal of Guidance, Control, and Dynamics*, 38(10):1976–1989, 2015. doi: 10.2514/1.G000581.

[84] A. M. Lyapunov. The General Problem of the Stability of Motion. *International Journal of Control*, 55(3):531–534, 1992. doi: 10.1080/00207179208934253.

[85] D. C. Heggie. Bifurcation at Complex Instability. *Celestial Mechanics*, 35(4):357–382, 1985. doi: 10.1007/BF01227832.

[86] C. R. Short. *Flow-Informed Strategies for Trajectory Design and Analysis*. PhD thesis, Purdue University, West Lafayette, Indiana, USA, 2016.

[87] A. Celletti. *Stability and Chaos in Celestial Mechanics*. Springer Science & Business Media, 2010.

[88] NASA Jet Propulsion Laboratory. Three-Body Periodic Orbits. `https://ssd.jpl.nasa.gov/tools/periodic_orbits.html`, 2021. Accessed: 8 June 2026.

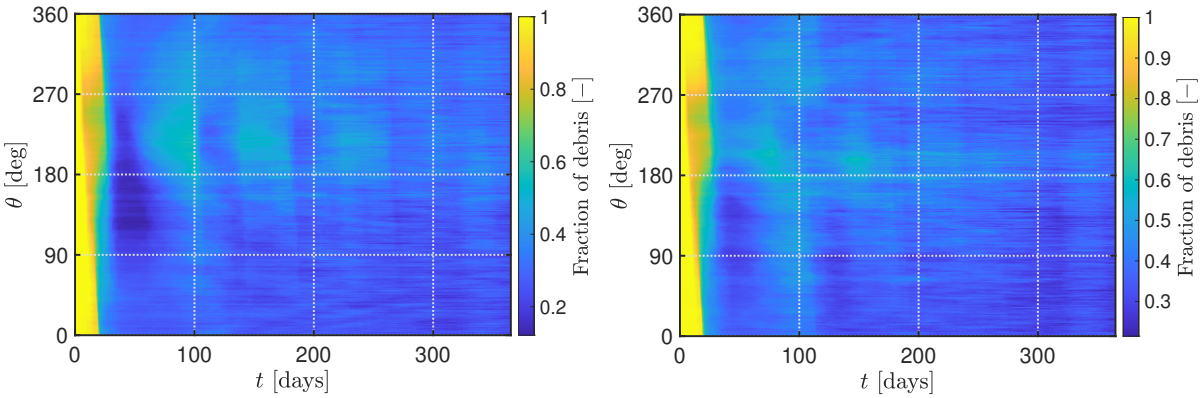
[89] F. G. Cicchi. Study of Heliocentric Escape Dynamics from Earth–Moon L_2 Near Rectilinear Halo Orbits. Master's thesis, Politecnico di Milano, Milan, Italy, 2026. Master in Space Engineering, Supervisor: C. Colombo, Co-supervisor: M. Bolis.

[90] M. Bolis, E. M. Alessi, J. P. Sánchez Cuartielles, C. Colombo, and S. Lizy-Destrez. Cislunar End-of-Life Strategies Based on an Aware Usage of Key Dynamical Objects. In *30th International Symposium on Space Flight Dynamics*, Toulouse, France, 2026.

[91] M. Bolis, E. M. Alessi, and C. Colombo. No-return Disposal Trajectories in the Earth–Moon System: A Parametric Analysis. *Aerospace Science and Technology*, 178:112452, 2026. doi: 10.1016/j.ast.2026.112452.

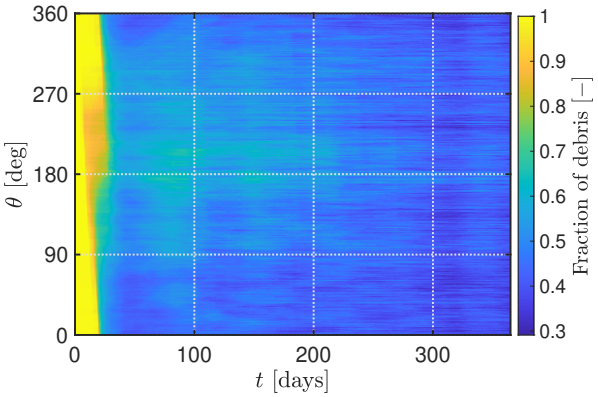
[92] A. Pressley. *Elementary Differential Geometry*. Springer, 2 edition, 2010. doi: 10.1007/978-1-84882-891-9.

A | Appendix A

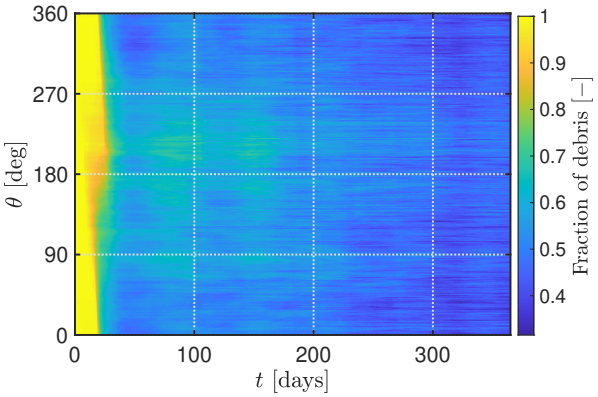


(a) $SI = 500$ [–].

(b) $SI = 250$ [–].

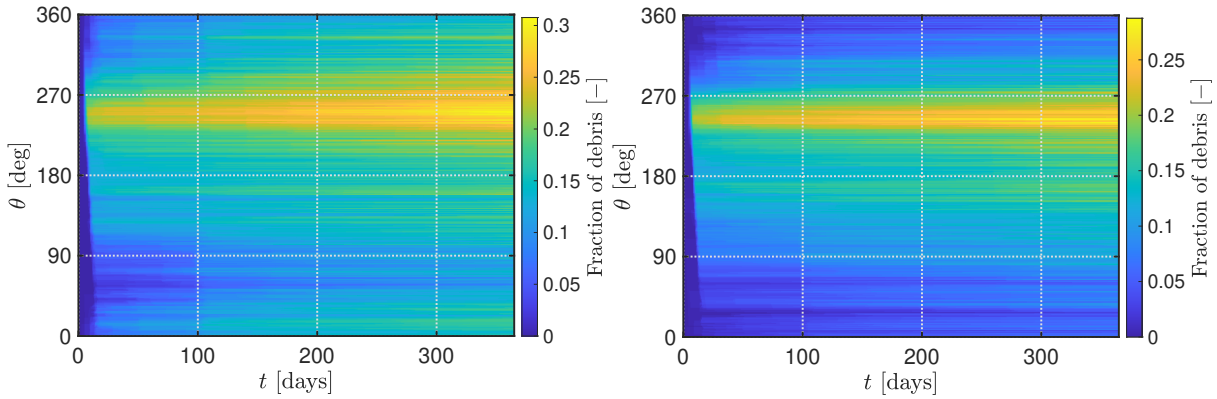


(c) $SI = 100$ [–].



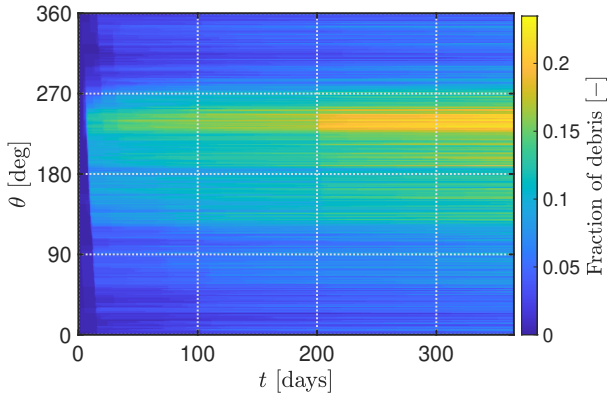
(d) $SI = 50$ [–].

Figure A.1: Debris event counter maps for N_{SOI} along selected Halo orbits.

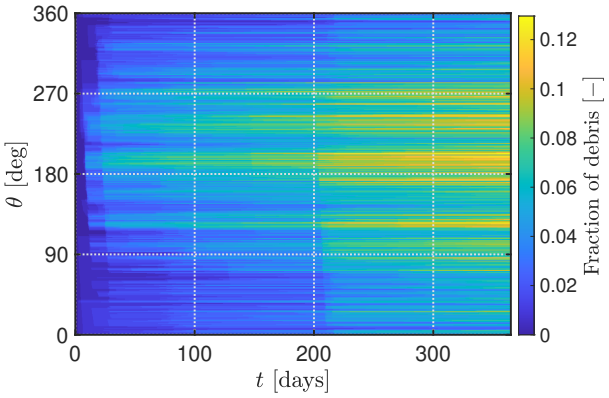


(a) $SI = 500$ [–].

(b) $SI = 250$ [–].

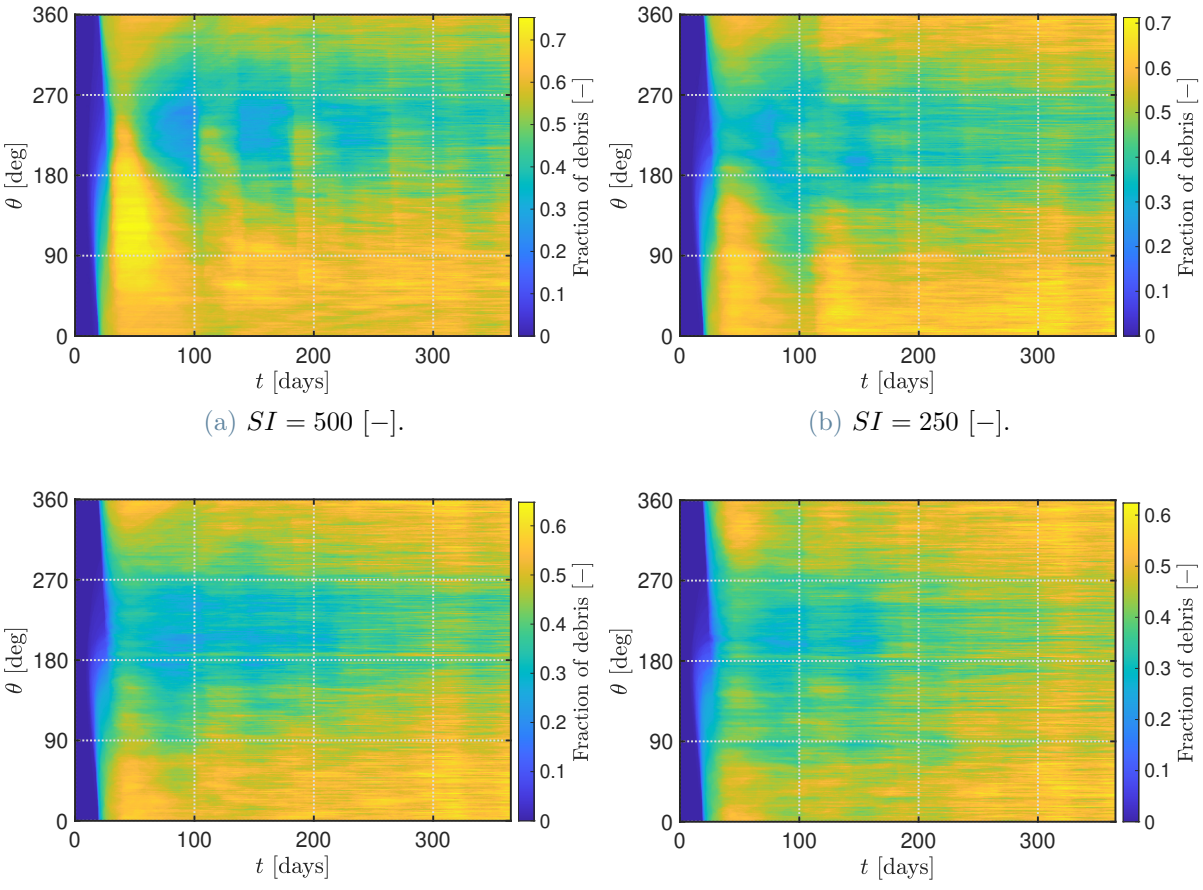


(c) $SI = 100$ [–].



(d) $SI = 50$ [–].

Figure A.2: Debris event counter maps for N_{Moon} along selected Halo orbits.



(a) $SI = 500$ [−].

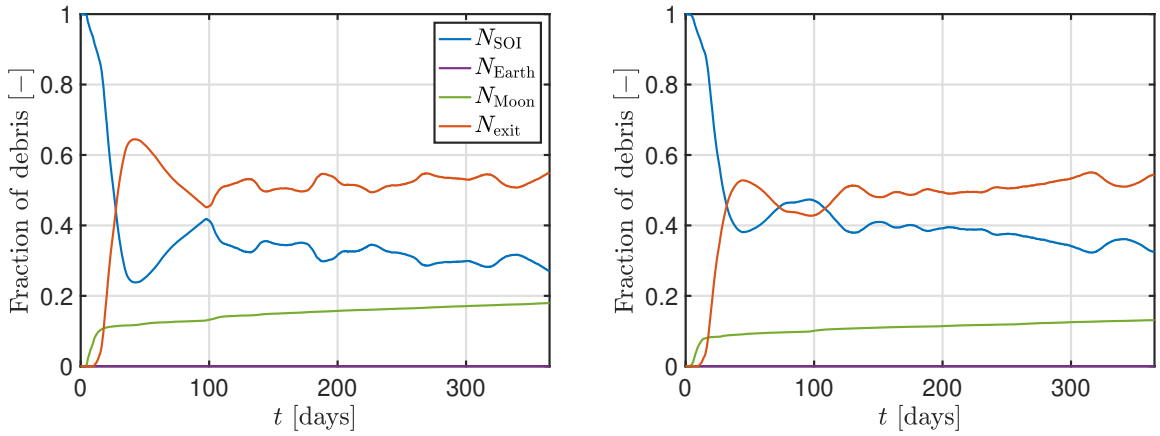
(b) $SI = 250$ [−].

(c) $SI = 100$ [−].

(d) $SI = 50$ [−].

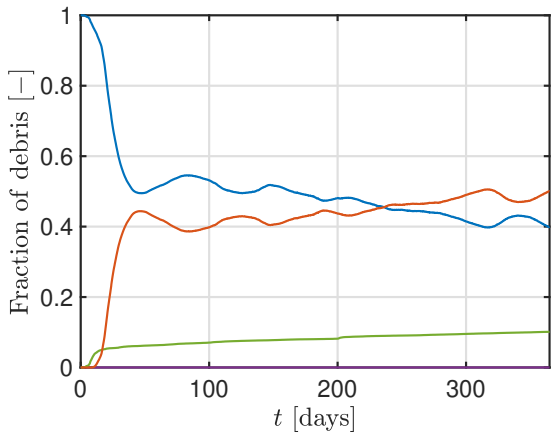
Figure A.3: Debris event counter maps for N_{exit} along selected Halo orbits.

B | Appendix B

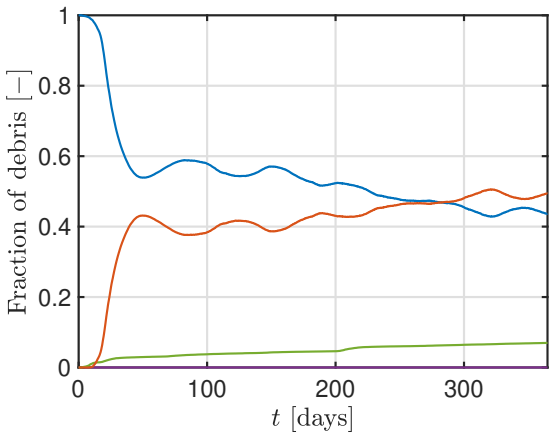


(a) $SI = 500$ [–].

(b) $SI = 250$ [–].



(c) $SI = 100$ [–].



(d) $SI = 50$ [–].

Figure B.1: Cumulative debris event counters along selected Halo orbits.

List of Figures

1.1 Evolution of catalogued objects in Earth orbit by object type [9]. 2

2.1 Inertial reference frame. 20
2.2 Rotating reference frame. 21
2.3 Collinear and triangular Lagrange points. 28
2.4 Zero Velocity Surfaces. 30
2.5 Zero Velocity Curves. 31
2.6 Family of southern Earth–Moon L_2 Halo orbits. 40
2.7 Unstable manifold directions. 44
2.8 Unstable manifold trajectories ($t_f = 22$ days). 45
2.9 Unstable manifold trajectories ($t_f = 60$ days). 45

3.1 Reference explosion event. 50
3.2 Distributions of the debris properties for the reference explosion event. . . 51
3.3 Family of southern Earth–Moon L_2 Halo orbits with a colormap on r_p. . . 52
3.4 Evolution of the main parameters along southern Earth–Moon L_2 Halo orbits. 52
3.5 Reference NRHO with 20 equally spaced values of θ. 54
3.6 Unstable manifold associated with the reference NRHO. 55

4.1 Debris trajectories after 24 hours in the EMB rotating frame. 58
4.2 Debris trajectories after 30 days in the EMB rotating frame. 59
4.3 Debris event counters along the reference NRHO, grouped by breakup location. 61
4.4 Debris event counters along the reference NRHO, grouped by counter type. 64
4.5 Debris event counter maps along the reference NRHO. 65
4.6 Cumulative debris event counters along the reference NRHO. 67
4.7 Debris event counter maps along the Halo family after 1 year. 68
4.8 Debris trajectories for a Halo orbit with $SI = 300$ [−] at $\theta = 240°$. 69
4.9 Mean and standard deviation of the JC of debris cloud as a function of θ. . 71
4.10 Temporal evolution of $\rho(t)$ with a colormap based on θ. 72
4.11 Temporal evolution of $\rho(t)$ with a colormap based on $\Delta\boldsymbol{v} \cdot \hat{\mathbf{T}}$. 73

4.12 FTLE evolution for debris exiting the Earth–Moon SOI within 1 month. . 75
4.13 FTLE evolution for debris impacting the Moon within 1 month. 75
4.14 FTLE evolution for debris inside the Earth–Moon SOI within 1 month. . . 76
4.15 Debris trajectories after a breakup event along a cislunar disposal trajectory. 77
4.16 Debris event counters along the reference disposal trajectory. 79
4.17 Global dependence of debris event counters on θ and t_{break}. 82
4.18 FTLE evolution for debris exiting the Earth–Moon SOI within 1 month. . 84
4.19 FTLE evolution for debris impacting the Moon within 1 month. 84
4.20 FTLE evolution for debris inside the Earth–Moon SOI within 1 month. . . 85

A.1 Debris event counter maps for N_{SOI} along selected Halo orbits. 101
A.2 Debris event counter maps for N_{Moon} along selected Halo orbits. 102
A.3 Debris event counter maps for N_{exit} along selected Halo orbits. 103

B.1 Cumulative debris event counters along selected Halo orbits. 105

List of Tables

2.1 Values of the parameters k and β for different breakup types. 13

3.1 Main parameters of the reference NRHO. 53

4.1 Debris event counters along the reference NRHO after 1 year. 60
4.2 Fraction of debris fragments in each JC interval. 70
4.3 Debris event counters along the reference disposal trajectory after 1 year. . 80

Acronyms

ASI	Italian Space Agency
BCR4BP	Bicircular Restricted Four-Body Problem
CGST	Cauchy-Green Strain Tensor
CR3BP	Circular Restricted Three-Body Problem
DRO	Distant Retrograde Orbit
EMB	Earth–Moon Barycentric
ESA	European Space Agency
FTLE	Finite-Time Lyapunov Exponent
GEO	Geostationary Earth Orbit
GMAT	General Mission Analysis Tool
GPU	Graphics Processing Unit
GTO	Geostationary Transfer Orbit
HEO	Highly Eccentric Orbit
IADC	Inter-Agency Space Debris Coordination Committee
IBEX	Interstellar Boundary Explorer
INAF	National Institute for Astrophysics
JC	Jacobi Constant
JPL	Jet Propulsion Laboratory
LEO	Low Earth Orbit
LLO	Low Lunar Orbit
LPO	Lagrangian Point Orbit
NASA	National Aeronautics and Space Administration
NOAA	National Oceanic and Atmospheric Administration
NPCM	Natural Parameter Continuation Method

NRHO	Near Rectilinear Halo Orbit
ODE	Ordinary Differential Equation
SBM	Standard Breakup Model
SI	Stability Index
SOI	Sphere of Influence
SOCIT	Satellite Orbital Debris Characterization Impact Test
SSA	Space Situational Awareness
STM	State Transition Matrix; Space Traffic Management
TLE	Two-Line Element
TNB	Tangent-Normal-Binormal
ZVC	Zero Velocity Curve
ZVS	Zero Velocity Surface

Acknowledgements

Vorrei ringraziare la Professoressa Camilla Colombo per avermi dato l'opportunità di svolgere questo lavoro di tesi e per avermi guidato durante tutto il percorso.
Un ringraziamento particolare va inoltre a Mathilda e Yeerang, mie correlatrici, per la loro costante disponibilità, il supporto e i preziosi suggerimenti, che hanno contribuito in modo fondamentale allo sviluppo di questo lavoro.